

ABSTRACT

Modeling the Influence of Ion Wakes on the Self-organization of Dust in a Complex Plasma

Katrina Vermillion, Ph.D.

Mentor: Lorin Swint Matthews, Ph.D.

The interaction between charged dust grains and streaming plasma leads to the formation of ion wakes, which are thought to be responsible for the self-organization of dust into complex structures. These structures have been observed to exhibit long-range stability both in ground-based and microgravity experiments. The response of dust in complex plasma to changes in experimental conditions is similar to the atomic-level ordering in traditional materials, but occurs at more easily observable spatial and temporal scales due to the larger dust grain size. The purpose of this work is to expand the current understanding of stable configurations of dust grains in a streaming plasma environment by implementing a molecular dynamics simulation that models dust and ions on their individual timescales. The model is used to determine plasma parameters that are currently unable to be directly measured experimentally and quantify their impact on dust structures, to compare and evaluate existing theoretical models of electric potential and resulting interactions between charged dust grains, and to quantify plasma conditions that lead to transitions between stable configurations of dust.

Modeling the Influence of Ion Wakes on the Self-organization of Dust in a Complex
Plasma

by

Katrina Vermillion, B.S., M.A.

A Dissertation

Approved by the Department of Physics

Lorin Swint Matthews, Ph.D., Chairperson

Submitted to the Graduate Faculty of
Baylor University in Partial Fulfillment of the
Requirements for the Degree
of
Doctor of Philosophy

Approved by the Dissertation Committee

Lorin Swint Matthews, Ph.D., Chairperson

Truell Hyde, Ph.D.

Gerald B. Cleaver, Ph.D.

Peter B. James, Ph.D.

Accepted by the Graduate School
December 2022

J. Larry Lyon, Ph.D., Dean

Copyright © 2022 by Katrina Vermillion

All rights reserved

TABLE OF CONTENTS

TABLE OF CONTENTS.....	iv
LIST OF FIGURES	vi
LIST OF TABLES	x
ACKNOWLEDGMENTS	xi
Chapter One	1
Introduction.....	1
1.1 Complex (Dusty) Plasma	1
1.2 Applications of Complex (Dusty) Plasma	3
1.3 Previous Work	6
1.4. Present Work.....	11
Chapter Two.....	15
Physical Processes in Complex (Dusty) Plasma.....	15
2.1 Characteristics of a Plasma	15
2.2 Dust Grain Charging.....	23
2.3 Timescales in a Complex (Dusty) Plasma	29
2.4 Ion Wakes	31
Chapter Three.....	36
Complex (Dusty) Plasma Experiments and Simulations.....	36
3.1 Plasmakristall-4 (PK-4) Microgravity Experiment.....	36
3.2 Ground-Based Experiments	40
3.3 Dynamic Response of Ions And Dust (DRIAD) Simulation.....	46
Chapter Four	54
Influence of Temporal Variations in Plasma Conditions on the Electric Potential Near Self-Organized Dust Chains	54
4.1 Introduction.....	54
4.2 Methods.....	62
4.3 Results.....	66
4.4 Discussion	76
4.5 Conclusion	89
Chapter Five.....	92
Interacting Dust Grains in Complex Plasmas: Ion wake formation and electric potential.....	92
5.1 Introduction.....	92
5.2 Background.....	94
5.3 Methods.....	95
5.4 Results.....	101
5.5 Discussion.....	117
5.6 Conclusion	128
Chapter Six.....	130
Conclusion and Outlook	130

6.1 Dust Chain Stability in the Presence of Ionization Waves	130
6.2 Dependence of Ion Wake Characteristics on Dust Grain Orientation	132
BIBLIOGRAPHY	135

LIST OF FIGURES

Figure 1.1 Types of plasmas that can be found at densities ranging from 10^1 cm^{-3} to 10^{15} cm^{-3} and temperatures from 100 to 100,000,000 K. Image credit: CASPER, Baylor University.....	2
Figure 1.2 Images showing examples of naturally occurring complex plasma.....	3
Figure 1.3 Experimental images of complex plasma exhibiting order indicative of (left panel) a crystal state, (center panel) a liquid-like state, and (right panel) a gaseous state.....	5
Figure 1.4 Top-down view of a plasma crystal with dust appearing as white dots on a black background	7
Figure 1.5 Side-view of two layers in a plasma crystal illustrating the vertical alignment of dust in adjacent horizontal layers	7
Figure 1.6 Photo illustrating water wakes formed behind ducks in water.....	8
Figure 1.7 Images from Hyde (2013) showing dust formed into various configurations with number of chains increasing from left (one chain) to right (eight chains).....	9
Figure 1.8 Illustration of dust structure formed (a) perpendicular to the ion flow direction, and (b) aligned parallel to the ion flow direction.	10
Figure 2.1 Illustration of the number of ionized and neutral gas atoms as a function of temperature using the expression in Equation 2.1.....	16
Figure 2.2 Illustration of a time-lapse depicting how a plasma bulk maintains quasi-neutrality	17
Figure 2.3 Illustration of the plasma response when a negatively charged dust grain is inserted into a neutral plasma.....	21
Figure 2.4 Illustration showing the trajectory of a charged particle moving toward (a) a neutral dust grain and (b) an oppositely charged dust grain.....	24
Figure 2.5 Plot of the left and right sides of Equation 2.26 for the case of singly-charged hydrogen with $X = e\Phi d/kBT$	28
Figure 2.6 Illustration depicting the deflection of ions in the vicinity of a charged dust grain.....	32

Figure 2.7 Illustration of the symmetric ion wake formed in the case of uniform polarity switching of the electric field direction	33
Figure 3.1 Illustration of the PK-4 ISS experiment [this figure was originally published in (Vermillion 2021)]	37
Figure 3.2 Photo of the PK-4BU. Photo credit: CASPER, Hyde lab, Parker Adamson, Baylor University.	42
Figure 3.3 Ionization waves observed in the PIC-MCC simulations of the BUD-DC experiment and the PK-4BU experimental results. [Image originally published in Hartmann 2020].....	44
Figure 3.4 Ion (top) and electron (bottom) temperatures obtained from PIC-MCC simulation of the BUD-DC discharge at 40 Pa neutral gas pressure.	45
Figure 3.5 Ion (top) and electron (bottom) temperatures obtained from PIC-MCC simulations of the BUD-DC discharge at 60 Pa neutral gas pressure.....	45
Figure 3.6 Illustration depicting the calculation of the potential from ions outside the simulation region (Φ_{out}) as the potential from ions inside the simulation region (Φ_{in}) subtracted from the total potential (Φ_d).	48
Figure 4.1 Illustration showing the qualitative behavior of the shielding ion cloud surrounding dust grains.....	56
Figure 4.2 Results from the PIC-MCC model illustrating time-varying electron and ion temperatures, axial electric field, electron and ion number densities, the ratio of n_i to n_e , and the Mach number	60
Figure 4.3 Results of the PIC-MCC model showing the time-varying electron temperature, axial electric field, and electron number density with the data selected for the various averaging schemes highlighted.....	64
Figure 4.4 Plot of ion density results from the DRIAD simulation of the four averaging cases	69
Figure 4.5 Plots showing the total electric potential from the DRIAD simulation along the z-axis and the fit to the axial potential taken at a radial distance of $9 \lambda_{Di}$ from the z-axis	71
Figure 4.6 Plots showing electric potential from the DRIAD simulation results for each of the four averaging cases	72
Figure 4.7 Plot of $g(r)$ pair correlation functions for the four averaging cases.....	74
Figure 4.8 Results from analysis of video data obtained during Campaign 7 of the PK-4 ISS experiment	76

Figure 4.9 Results from simulations of a single dust grain in plasma conditions corresponding to the four averaging cases.....	81
Figure 4.10 Comparison of the simulation results for a single, isolated dust grain with the analytic potentials	83
Figure 4.11 Comparison of the superimposed single dust grain simulation results with the 20 dust grain simulation results and analytic potentials	85
Figure 4.12 Figure 4.12. Comparison of electric potential from the DRIAD simulation of 20 dust grain chains in the four averaging cases with the analytic potentials.....	86
Figure 4.13 Dynamic charging of a dust grain in evolving plasma conditions associated with the ionization waves	89
Figure 5.1 An illustration indicating the positions of stationary dust grains in the simulations with two and three dust grains.....	98
Figure 5.2 Illustration of the 2D grid spacing used to determine 3D characteristics of the ion wake for two representative cases	100
Figure 5.3 Results from two and three dust grain simulations illustrating lower dust grain charge as a fraction of upper right dust grain charge.....	102
Figure 5.4 Results from the simulation of a single dust grain showing the ion density as a contour plot and the distance to the maximum ion density location along each angle as a scatter plot.....	104
Figure 5.5 Contour plots of normalized ion density for representative cases from the two dust grain simulations	105
Figure 5.6 Ion wake characteristics from two dust grain simulations	107
Figure 5.7 Contour plots of normalized ion density for representative cases from the three dust grain simulations	109
Figure 5.8 Ion wake characteristics from simulations of three dust grains	110
Figure 5.9 Results from a single dust grain simulation showing the Coulomb potential of the charged dust grain, the electron shielded potential of ions inside and outside the simulation region, and the total electric potential.....	113
Figure 5.10 Simulation results for the total electric potential surrounding a single dust grain.....	114
Figure 5.11 Results for the total electric potential from two dust grain simulations.....	115

Figure 5.12 Results for the total electric potential from three dust grain simulations	116
Figure 5.13 Comparison between the total electric potential obtained from DRIAD simulation results with the Coulomb potential and Yukawa potential.....	118
Figure 5.14 Comparison between the total electric potential in two dust grain DRIAD simulation with the potential determined by Equation 5.2 and the potential determined by Equation 5.3	120
Figure 5.15 Comparison between the DRIAD simulation results for four representative cases with two and three stationary dust grains and the total electric potential which results from a superposition of the single dust grain simulation results at each dust grain location	123
Figure 5.16 Contour plots illustrating the potential energy (U) from simulations of two dust grains.....	125
Figure 5.17 Contour plots illustrating the total electric potential for three dust grain simulations with the lower dust grain at the position with the minimum energy centered between the upper two dust grains and at the minimum energy position calculated from two dust grain simulations	127

LIST OF TABLES

Table 4-1 Plasma parameters used for each of the four averaging cases.....	63
Table 4-2 Size of the cylindrical simulation region, final average interparticle spacing, and final average dust grain charge for each averaging case.....	67
Table 5-1 Plasma parameters used for input in the DRIAD simulation.	97

ACKNOWLEDGMENTS

First and foremost, I am extremely grateful to Dr. Lorin Matthews, my research advisor and dissertation committee chairperson, for her guidance, support, and for sharing her expertise throughout this journey. I am deeply appreciative to Dr. Truell Hyde for his mentorship, encouragement, and helping me stay grounded in the broader context of my research. I would also like to thank Dr. Gerald Cleaver and Dr. Peter James for serving as members of my dissertation committee and for providing useful input and helping me to see the work from a different perspective.

Many thanks to the members in the High Performance and Research Computing Services at Baylor University, including Mike Hutcheson, Carl Bell, and Brian Sitton, who have provided invaluable support for me relating to the GPUs on Kodiak that were needed to run the many simulations used to complete this work. I am also grateful for the support from members of our research group and my fellow graduate students, who have provided an environment where I felt welcome and able to ask for help.

I would also like to acknowledge the love and support from my family, whose constant encouragement has propelled me to heights I never imagined were possible and whose patience truly knows no bounds.

CHAPTER ONE

Introduction

1.1 Complex (Dusty) Plasma

Plasma is composed of unbound electrons, ions, and neutral gas atoms and may be generated by supplying sufficient energy to a neutral gas. Since this process is similar to the way adding energy to a solid can result in a phase transition to a liquid or a liquid to a gas, plasma has been termed the fourth state of matter (Chen 2018). Although plasma shares some properties with a neutral gas, such as having no definite shape or volume, plasma is distinct in interesting ways. The significant number of unbound charged particles in plasma makes it conductive, allowing plasma to conduct electric currents and respond to electric and magnetic fields. While interactions in a neutral gas are typically binary (or, rarely, three-body), charged particles in a plasma will respond collectively to long-range electric and magnetic forces, overwhelming the contribution from random binary interactions. In this manner, plasma exhibits collective behavior among large numbers of particles in response to electric and magnetic forces.

Plasma is thought to comprise more than 99% of the visible material in the universe (Gurnett 2005) and is present in many naturally occurring forms, including lightning, aurorae, solar wind, and stars, and artificially created forms, including fluorescent lights, plasma TVs, fusion reactors, and ion thrusters. These conditions correspond to a wide range of plasma temperatures and densities, as shown in Figure 1.1, which are parameters that play a large role in determining the nature of plasma dynamics.

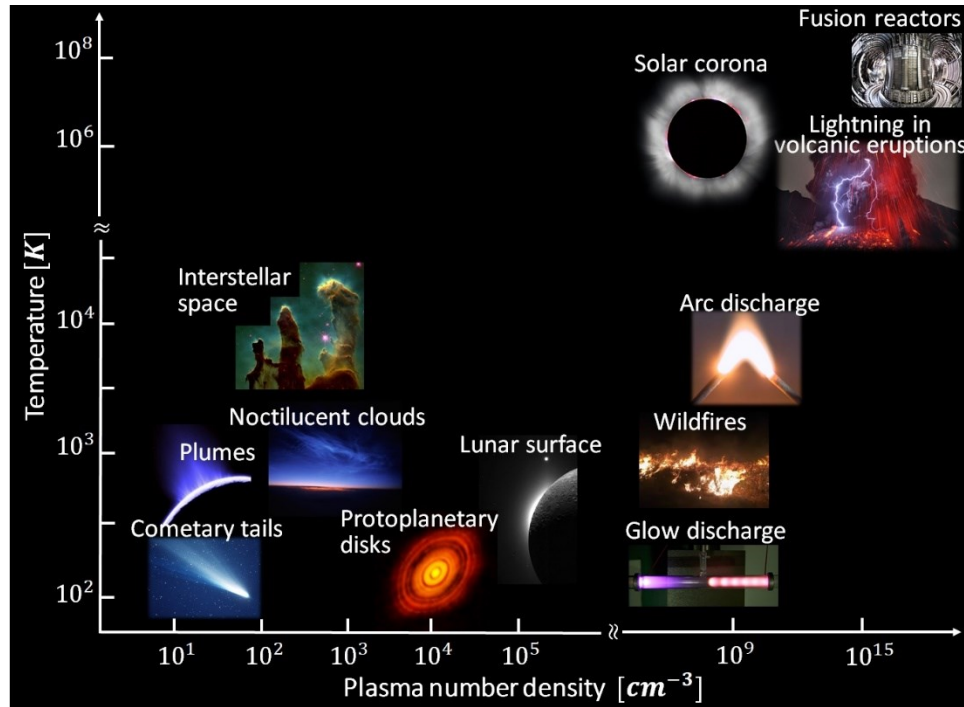


Figure 1.1 Types of plasmas that can be found at densities ranging from 10^1 cm^{-3} to 10^{15} cm^{-3} and temperatures from 100 to 100,000,000 K. Image credit: CASPER, Baylor University.

Complex (dusty) plasma is a plasma into which macroscopic particles, referred to as dust, are immersed. Individual dust particles typically range in size from a few nanometers to millimeters in diameter and can become highly charged through interactions with ions and electrons in the plasma. As with plasma more broadly, complex plasma may be found naturally occurring in a wide variety of astrophysical and terrestrial environments (as well as some artificially created plasma). Examples of complex plasma include comet tails, the rings of Saturn, the lunar surface, fusion reactors, and plasma etchers for semiconductor manufacturing. Images of naturally occurring complex plasma in (a) Saturn’s rings, (b) a nebula in the Triangulum constellation, and (c) noctilucent clouds are provided in Figure 1.2.

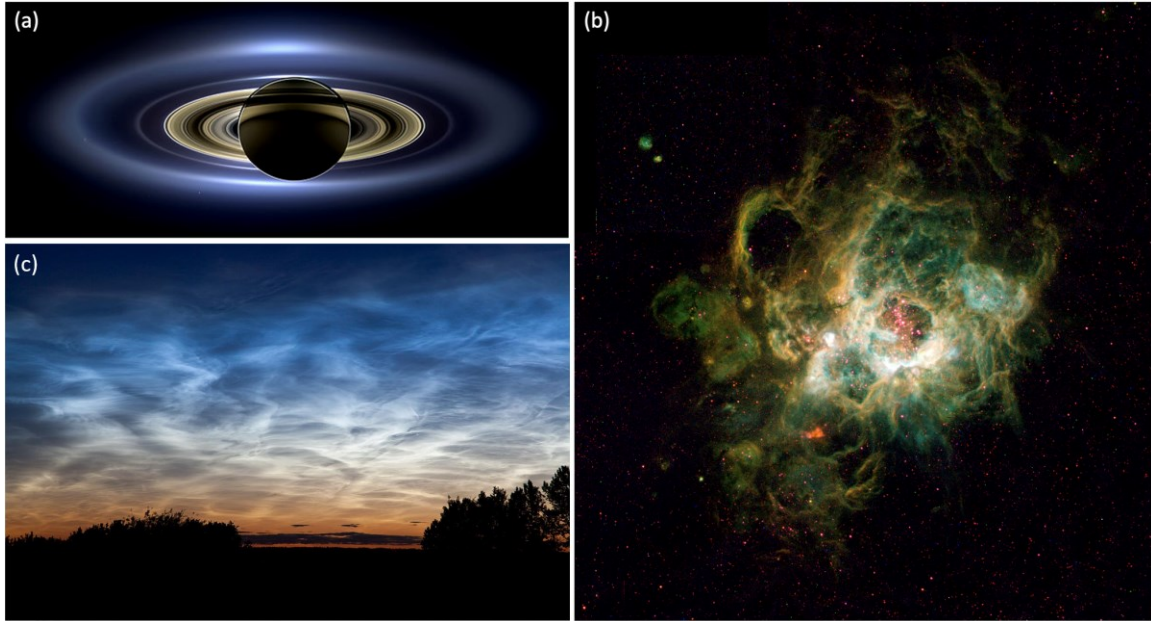


Figure 1.2 Images showing examples of naturally occurring complex plasma in (a) Saturn’s rings imaged by NASA’s Cassini spacecraft on July 19, 2013 (image credit: NASA/JPL-Caltech/SSI), (b) a Hubble Space Telescope image of a vast nebula called NGC 604, which lies in the neighboring spiral galaxy Messier 33, located 2.7 million light-years away in the constellation Triangulum (image credit: Hui Yang, University of Illinois, and NASA/ESA), and (c) noctilucent clouds above Edmonton, Alberta, in Canada on July 2, 2011 (image credit: NASA/Dave Hughes).

1.2 Applications of Complex (Dusty) Plasma

Complex plasma research has applications in numerous fields due to the ubiquitous presence of plasma and dust throughout the universe. Highly charged micrometer-sized particles immersed in plasma contribute to the formation of planets, enable investigation into microscopic phenomena and fundamental physics, and currently present challenges for technological advances in device manufacturing and aerospace endeavors.

1.2.1 Planet Formation.

A likely candidate for the formation of planets is the core-accretion model (Klahr 2006, Weidenschilling 2000), where micron-sized dust in a protoplanetary disk accumulates over time to form kilometer-sized planetesimals. Since the dust grains are relatively small, a force other than gravitational attraction is needed to cause the dust grains to adhere to one another, and it has been suggested that electrostatic forces may be responsible (Xiang 2021). The interactions between charged dust grains and ionized gas in the protoplanetary disk provide a rich environment for complex plasma research (Cui 1994, Matthews 2012, 2013, 2018, Castrejon 2019).

1.2.2 Aerospace

The presence of complex plasma in the interplanetary medium presents technological challenges for satellites, probes, and crewed missions. Charged dust and ice particles in the Earth's ionosphere form noctilucent clouds and are responsible for the polar mesosphere summer echoes that are associated with strong radio echoes at frequencies between 50-1000 MHz (Klumov 2000). Similar structures have also been observed in the Martian ionosphere (Dubinskii 2019). Accumulation of charged dust grains on equipment and personnel can result in hazardous electric potential differences, decreased thermal dissipation, and may pose health concerns due to the abrasive nature of lunar soil (Dukes 2013, Kureshi 2020, Wang 2020).

1.2.3 Materials and Device Fabrication

Complex plasma research became of interest in the semiconductor manufacturing industry as early as the 1980s when electrically charged dust grains were identified as a

source of device contamination in plasma etching reactors (Selwyn 1989). Dust may form as a result of chemical changes in the plasma, or as debris from surfaces in contact with the plasma (Hollenstein 1994). Although dust was initially seen as a nuisance, precisely controlled complex plasma has yielded advancements in creating dust particles with desired traits to be used in other applications as well as the use of dust grains to seed thin films through plasma enhanced chemical vapor deposition (Kersten 2003).

1.2.4 Fundamental Physics

Dust has been experimentally observed to form liquid and crystalline phases similar to ionic clusters or colloidal suspensions (Chu 1994, Fortov 1997, Hartmann 2010), and it was found that phase transitions in the complex plasma were easily controlled in experimental plasma discharges by varying the radio-frequency (rf) power or pressure, which varies the coupling strength between dust grains (see Figure 1.3). As

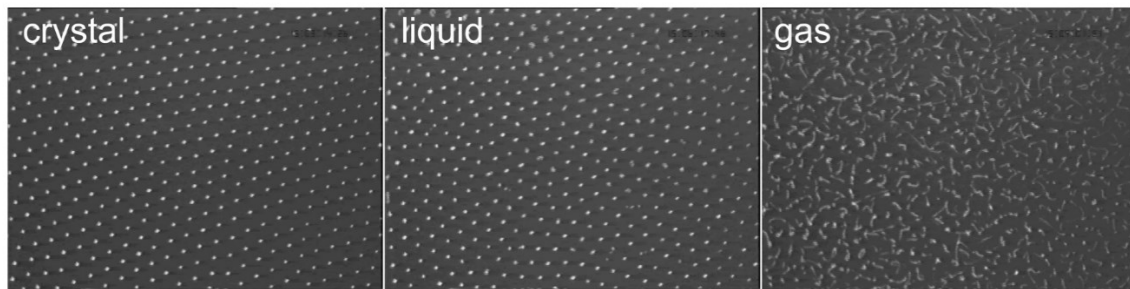


Figure 1.3 Experimental images of complex plasma exhibiting order indicative of (left panel) a crystal state, (center panel) a liquid-like state, and (right panel) a gaseous state. Dust appears white, background plasma appears dark gray. [Image initially published in Morfill (2009)].

such, complex plasma is now classified as the plasma state of “soft matter,” in which a material has a supramolecular and molecular component (here represented by the dust grains and the background plasma, respectively), exhibits softness on a macroscopic

level, has metastable states, and the overall structure depends on external conditions (Morfill 2009). The ability to observe molecular-level behavior in a complex plasma make it a useful analogue for microscopic systems due to the relative ease of observing dust grains at high spatiotemporal resolution (Fortov 2005b, Chaudhuri 2010).

1.3 Previous Work

1.3.1 Self-Organized Structures

1.3.1.1 Plasma Crystals Early calculations suggested that charged particles interacting in a plasma should be able to form into solid-like, crystalline structures (Ikezi 1986, Farouki 1992), which was confirmed by experimental observation of liquid and crystalline structures in an rf plasma (Chu 1994, Thomas 1994, Trottenberg 1995). The dust was observed to form a quasi-2D hexagonal crystal structure at low rf powers (e.g., experimental conditions provided in Chu 1994 were approximately 1 W at argon pressure of 200 mTorr). A top-down view of a plasma crystal formed in a similar experiment is shown in Figure 1.4, with the dust grains appearing as black dots on a white background. Dust grains in the plasma crystal levitate just above the lower electrode, where the force of Earth's gravity pulling the dust grains downward is balanced by the electric force from the charged lower electrode pushing the dust grains back upward. Since the balance between gravitational and electric forces occurs over a very narrow range of heights above the lower electrode, the plasma crystal tends to spread horizontally while remaining compressed into just a few layers in the vertical direction. When more energy is supplied to the system by increasing the rf power, the stability of the dust formation breaks down and the plasma crystal melts (Chu 1994). Interestingly, melting of the

plasma crystal is triggered by ion flow changes in the background plasma rather than by an increase in the temperature of the dust grains (Schweigert 1996).

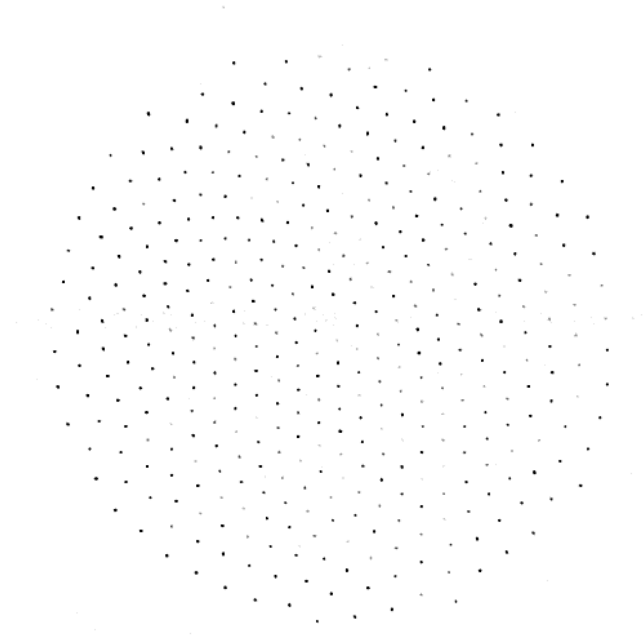


Figure 1.4 Top-down view of a plasma crystal with dust appearing as black dots on a white background. Image credit: CASPER, Hyde lab, Baylor University.

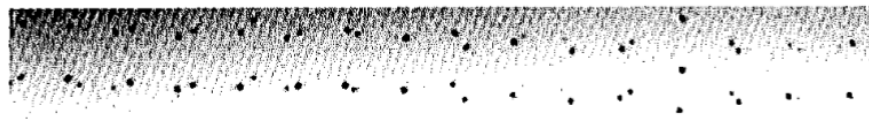


Figure 1.5 Side-view of two layers in a plasma crystal illustrating the vertical alignment of dust in adjacent horizontal layers. Dust appears as black dots on a white background. [Image taken from Figure 1 in (Melzer 1996)]

Trottenberg et al. (1995) noted that particles in neighboring horizontal layers were often aligned in vertical chains (like those seen in Figure 1.5, which shows a side-view of a plasma crystal), and “coupling within such a chain seem[ed] to be very strong because

when a particle changes the position in its horizontal plane, the entire chain follows.”

The vertical alignment of particles in adjacent crystal layers in the sheath of rf discharges was attributed to an attractive force arising from the motion of streaming ions (Melzer 1996, Schweigert 1996). Ions flowing past a dust grain form a wake, similar to the wake that forms as water flows around an obstacle (as illustrated in Figure 1.6), and become concentrated downstream from the dust. Schweigert et al. (1996) used Monte Carlo simulations to show that increased dust motion observed when the rf power was increased arose from an instability related to the ion flow that led to a phase transition in the plasma crystal, rather than being caused by the phase transition.



Figure 1.6 Photo illustrating water wakes formed behind ducks in water. Image credit: Anders Sandberg.

1.3.1.2 Strings, zigzags, and other structures In addition to quasi-2D crystals, the dust in complex plasma experiments has also been observed to form structures made up of smaller numbers of particles which exhibit interesting symmetry. By adjusting the ratio of confinement forces, the dust can be forced to align in a single chain, a pair of

parallel chains with alternating dust locations (a zigzag), or several offset chains (a helical structure), as shown in Figure 1.7. These configurations have been observed to

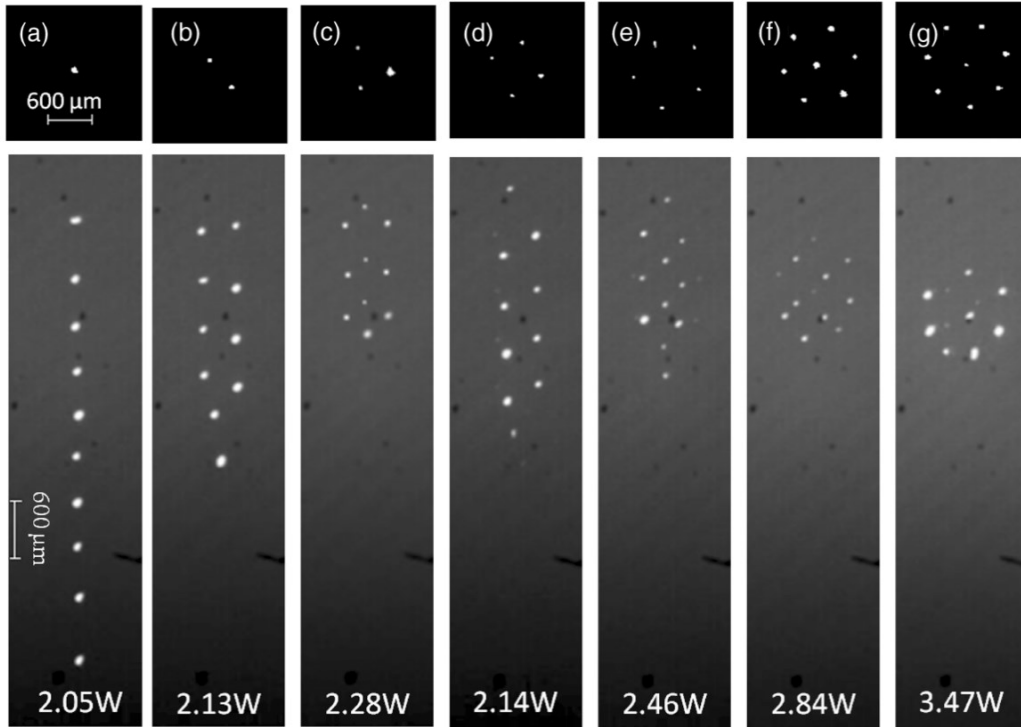


Figure 1.7 Images from Hyde (2013) showing dust formed into various configurations with number of chains increasing from left (one chain) to right (eight chains).

form with the dust aligned perpendicular to the direction of the ion flow (illustrated in Figure 1.8a), or with dust aligned parallel to the ion flow (illustrated in Figure 1.8b). Since ion wakes form downstream from a dust grain, the ion wakes that develop in a horizontally-aligned configuration of dust grains (Figure 1.8a) will be in a plane below the dust structure while the wakes that form in a vertically aligned configuration (Figure 1.8b) will be in line with the dust structure itself.

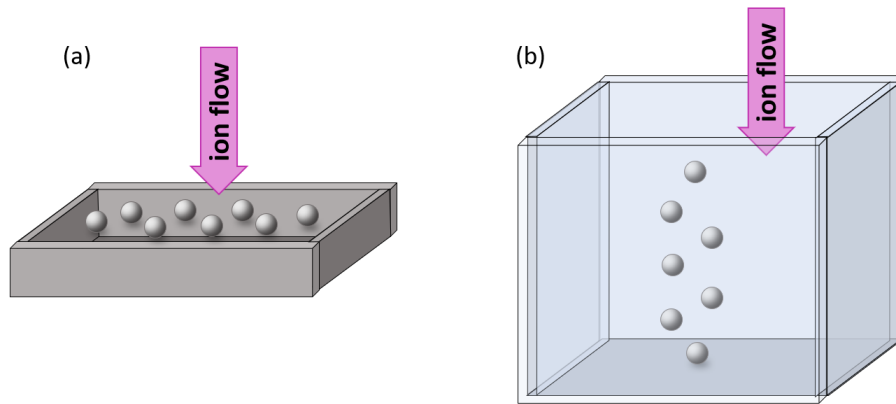


Figure 1.8 Illustration of dust structure formed (a) perpendicular to the ion flow direction, and (b) parallel to the ion flow direction.

1.3.2. *Interparticle Attraction*

Normally, the electric force between two dust grains with the same sign charge would cause the dust grains to repel each other, but they have been observed to move closer together as the dust organizes into stable structures. In this case, the stability of the dust structures requires another force to balance the interparticle repulsion, and several attractive forces have been suggested.

One example is the attractive force provided by streaming ions which can be attributed to a positive potential at the location of higher ion density in the ion wake. It was proposed that in cases when the ions are flowing faster than the ion acoustic velocity, the ion density is enhanced at regular intervals along the direction of the ion flow. This produces an oscillatory wake field downstream from a static dust grain that is sufficient to generate an attractive force between dust particles of the same sign charge (Vladimirov 1995, Ishihara 1996, Takahashi 1998). The attractive force responsible for aligning dust grains along the ion flow direction is asymmetric, propagating downstream along the

direction of ion flow and not upstream (Melzer 1999). The asymmetry of the attractive force was shown experimentally by perturbing the upper or lower dust grain in a vertically aligned pair. When perturbed, the downstream dust grain was found to follow the motion of the upstream grain, but the upstream grain was not observed to follow the lower dust grain when displaced.

Another attractive force between dust grains can be attributed to an asymmetry in the transfer of momentum from ions impinging on the grain, which Lampe et al. (2000) termed a shadowing force. Since some of the ion trajectories to a downstream dust grain will be blocked by an upstream dust grain, there will be an asymmetric number of ions collected on the lower half of the dust grain causing an apparent force directed toward the upper dust grain (although the authors noted it is expected to be significant only in low pressure or high density plasma).

Ions which become trapped in the potential well near a highly charged dust grain, but not collected by the dust grain, may also contribute to an attractive force between dust grains (Lampe 2001). Under these conditions, the trapped ions and negatively charged dust grain behave as a classical atom and may become polarized, possibly giving rise to van-der-Waals type interparticle interactions.

1.4. Present Work.

The self-organization of dust grains in a complex plasma offers a useful analogue for probing interactions that occur on a microscopic level, but interactions between charged dust grains and the background plasma environment have yet to be fully described. There are notable assumptions underlying the current framework for calculating the electric potential near charged dust grains, such as the assumption that the

dust grain is immersed in a stationary homogeneous plasma, or that the dust is sufficiently far from other dust grains which might perturb the plasma. This calls into question whether the analytic potentials are well-suited for describing the interaction between dust grains at the close interparticle spacing found in experimentally observed chains, zigzags, and helices.

In order to provide a more accurate description of the electric potential, detailed information is needed concerning the response of ions to the presence of charged dust grains. In this work, ion and dust grain motion and dust grain charging are modeled under the conditions present in microgravity and terrestrial complex plasma experiments where dust grains have been observed to self-organize. The information obtained about ion and dust response is analyzed to characterize resulting dust structure and minimum energy configurations. The electric potential is calculated directly from the locations and charges of ions and dust grains, and compared with commonly used forms of the electric potential. The goal of this work is to provide a useful description of the interaction between charged dust grains at the length scales relevant for self-organization, and describe conditions that lead to the formation of stable configurations of dust grains.

This dissertation is organized as follows:

Chapter Two contains an overview of physical processes in a complex plasma that are relevant for the current work. *Chapter Three* describes complex plasma experiments which were used for comparison and motivation of the present work, and a description of the numerical simulation.

Chapter Four presents the results from simulations of dust in microgravity conditions present at three stages within ionization waves, and compares with simulation

results when the time-averaged plasma conditions are considered. This chapter was published as [] Vermillion, K., Sanford, D., Matthews, L., Hartmann, P., Rosenberg, M., Kostadinova, E., Carmona-Reyes, J., Hyde, T., Lipaev, A. M., Usachev, A. D., Zobnin, A. V., Petrov, O. F., Thoma, M. H., Pustynnik, M. Y., Thomas, H. M., Ovchinin, A., 2022. "Influence of temporal variations in plasma conditions on the electric potential near self-organized dust chains." *Physics of Plasmas* 29, 023701. KV ran the simulations, performed the analysis, and wrote the initial manuscript with support from LM, EK, MR, and TH. The DRIAD simulation was initially developed by LM and modified by DS. PH provided PIC-MCC simulation data that were used as input for the present simulations. JC-R, EK, AML, ADU, AVZ, OFP, MT, MYP, HT, and TH facilitated obtaining and processing PK-4 data that was analyzed for comparison. AO performed the Campaign 7 PK-4 experiment used for comparison with simulation results. LM, EK, and TH provided improvements to manuscript organization, data visualization, and research direction. All authors contributed to revisions of the manuscript.

Support for this work from NSF grant number 1740203, NASA grant number 1571701, and the U.S. Department of Energy, Office of Science, Office of Fusion Energy Sciences under award number DE-SC-0021334, and by the National Office for Research, Development, and Innovation of Hungary (NKFIH) via grant 134462 is gratefully acknowledged. All authors gratefully acknowledge the joint ESA - Roscosmos "Experiment Plasmakristall-4" on-board the International Space Station. The microgravity research is funded by the space administration of the Deutsches Zentrum für Luft- und Raumfahrt eV with funds from the federal ministry for economy and technology according to a resolution of the Deutscher Bundestag under Grants No.

50WM1441 and No. 50WM2044. A. M. Lipaev and A. D. Usachev were supported by the Russian Science Foundation Grant No. 20-12-00365.

Chapter Five presents the results from simulations of one, two, and three stationary dust grains at various interparticle separation distances and orientations relative to the axial electric field which were performed to quantify the effect of the angle of offset relative to the ion flow direction on ion wake formation. This paper was submitted as [] Vermillion, K., Banka, R., Mendoza, A., Wyatt, B., Matthews, L., Hyde, T., 2022. “Interacting dust grains in complex plasmas: ion wake formation and electric potential.” arXiv. KV ran the simulations, performed the analysis, and produced the initial manuscript with support from LM and TH. RB assisted with development of the point charge ion wake analysis. AM and BW provided support with implementation of the simulations and analysis of results. LM and TH provided advice on improvements to the organization of the manuscript, data presentation, and interpretation of results. All authors contributed to preparation of the manuscript.

Chapter Six summarizes the conclusions drawn from this work including a review of the influence of ion wakes on the electric potential. An outline of future work which can be done to expand on the work accomplished so far is given, and concludes the dissertation.

CHAPTER TWO

Physical Processes in Complex (Dusty) Plasma

2.1 Characteristics of a Plasma

2.1.1 Ionization of Gas

A typical method to generate plasma in the laboratory is to apply a voltage to electrodes positioned at either end of a discharge chamber, forming either a constant (as in direct current, DC, discharge) or oscillating (as in capacitively coupled radio-frequency, ccrf, discharge) electric field (Raizer 1997). The electric field accelerates ions and electrons, which then collide with neutral gas atoms, transferring energy to the neutral gas and releasing additional ions and electrons. As the amount of energy in the gas is initially increased, raising the kinetic temperature of the gas atoms, ionization levels rise slowly according to the Saha equation, which may be expressed as

$$\frac{n_i n_e}{n_n} = V \left(\frac{2\pi m_e k_B T}{h^2} \right)^{\frac{3}{2}} \exp\left(-\frac{U_i}{k_B T}\right) \quad (2.1)$$

where n_i , n_n , and n_e are the ion, neutral gas, and electron densities, respectively, V is the volume occupied by the gas, m_e is the mass of an electron, T is the neutral gas temperature, h is Planck's constant, U_i is the ionization energy, and k_B is the Boltzmann constant (Schroeder 2000). As $k_B T$ increases beyond a threshold value, the proportion of ions to neutral atoms rises sharply, and the neutral gas transitions to a plasma (Chen 2018). A representative case is illustrated in Figure 2.1 with the values $V = 1 \text{ m}^3$, $U_i = 15.7 \text{ eV}$, and the total number of gas atoms $N_{total} = n_i + n_n = 4.83 \times 10^{22}$ (where

the gas pressure is 200 Pa). Under these conditions, the number of ionized gas atoms increases rapidly with increasing temperature when $k_B T$ reaches about 6% of U_i .

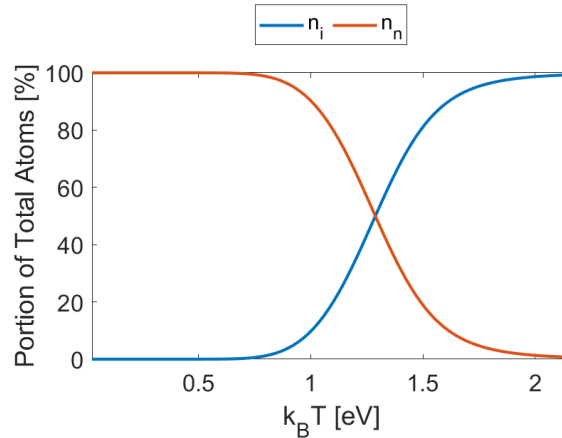


Figure 2.1 Illustration of the number of ionized and neutral gas atoms (n_i and n_n , respectively) as a function of temperature ($k_B T$) using the expression in Equation 2.1 with $U_i = 15.7$ eV, $V = 1$ m³, and $n_i + n_n = N_{\text{total}} = 4.83 \times 10^{22}$.

2.1.2 Quasi-Neutrality Condition

In the bulk of a plasma (sufficiently far away from the boundaries of the discharge chamber and any other surfaces in contact with the plasma), there are approximately equal numbers of ionized gas atoms and electrons, and the plasma is quasi-neutral at the macroscopic scale, meaning that any local asymmetry of charge is dissipated by the resulting electric forces. This process is illustrated in Figure 2.2, where (a) an initial excess of positive charges (orange circles) generates a local electric field that (b) exerts a force on the positive and negative charges (green circles) so that they reorient into (c) a more uniform distribution.

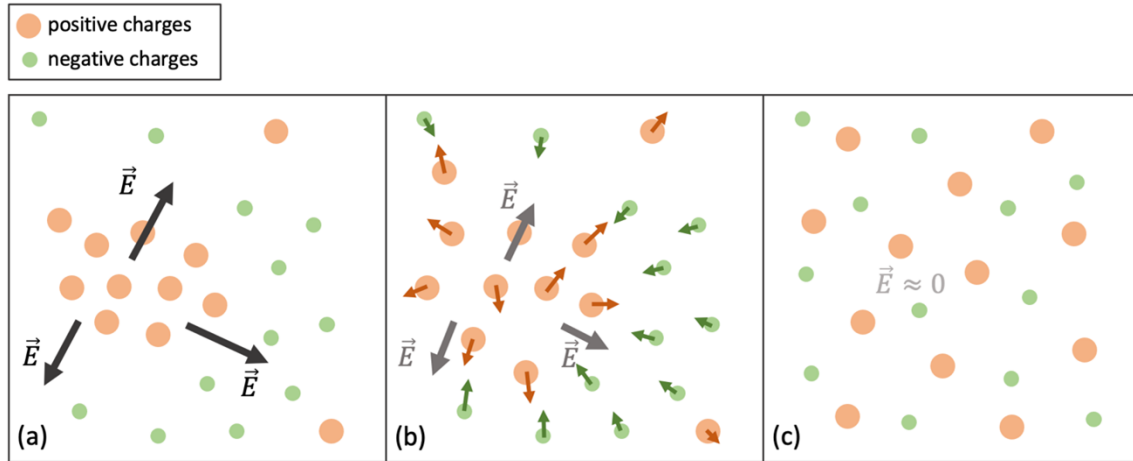


Figure 2.2 Illustration of a time-lapse depicting how a plasma bulk maintains quasi-neutrality. (a) Positive and negative charges are arranged with an unequal charge distribution that has formed a local electric field. (b) The charges are accelerated by the electric field so that the higher concentrations of positive and negative charges (orange and green circles, respectively) begin to disperse, with the acceleration direction represented by the orange and green arrows. (c) The charges reach an approximately neutral configuration with no regions of positive or negative charge concentration, and the electric field reduces to near zero at all points.

The scale at which the quasi-neutrality condition, $n_i q_i - n_e q_e = 0$, is applicable may be examined by estimating the largest region where non-neutrality may occur. Consider a sphere of radius r within a neutral plasma which initially contains equal numbers of electrons and ions with random velocities. The electrons within the sphere may (under unlikely circumstances) undergo random thermal fluctuations that result in the entirety of the electrons leaving the sphere and coming to rest just at the surface. The resulting imbalance of charges between the sphere of ions and the shell of electrons will produce an electric field that is directed radially outward from the sphere (similar to the illustration in Figure 2.2a). If no other sources of energy are present, then the amount of energy contained in the resulting electric field must be equal to the initial thermal energy

of the electrons (Bellan 2008). The initial thermal energy of the electrons with density n in a sphere with radius r at temperature T is

$$E_{\text{kinetic}} = \frac{3}{2} N k_B T = \frac{3}{2} \left[n \times \left(\frac{4}{3} \pi r^3 \right) \right] k_B T = 2\pi n k_B T r^3 \quad (2.2)$$

where $N = n \times \left(\frac{4}{3} \pi r^3 \right)$ is the number of electrons. The energy density contained in an electric field is $\epsilon_0 E^2 / 2$, where ϵ_0 is the permittivity of free space. The electric field, E , produced by the sphere of ions can be calculated using Gauss's law,

$$\oiint \vec{E} \cdot d\vec{A} = \frac{Q}{\epsilon_0}, \quad (2.3)$$

where Q is the amount of charge contained in the sphere of ions. With the initial ion density assumed to be equal to the initial electron density, n , the amount of charge in a sphere of ions is $Q = ne \times \left(\frac{4}{3} \pi r^3 \right)$, where e is the (positive) elementary unit charge.

Since the electric field is pointing radially outward, the angle between the vectors \vec{E} and $d\vec{A}$ is zero, which means the dot product on the left of Equation 2.3 is able to be rewritten as $\vec{E} \cdot d\vec{A} = E_r dA = E_r r^2 \sin \theta d\theta d\phi$ (where $dA = r^2 \sin \theta d\theta d\phi$ in spherical coordinates). Using these expressions for Q and $\vec{E} d\vec{A}$, Equation 2.3 can be rewritten as

$$\int_0^{2\pi} \int_0^\pi E_r r^2 \sin \theta d\theta d\phi = E_r r^2 (4\pi) = \frac{4\pi n e r^3}{3\epsilon_0} \quad (2.4)$$

which may be solved for the radial electric field to produce $E_r = ner/3\epsilon_0$. Using this result along with the expression for the energy density in an electric field yields the expression

$$\begin{aligned}
E_{\text{field}} &= \iiint \frac{\epsilon_0 E^2}{2} dV = \int_0^{2\pi} \int_0^\pi \int_0^r \frac{\epsilon_0}{2} \left(\frac{ner'}{3\epsilon_0} \right)^2 r'^2 \sin \theta dr' d\theta d\phi \\
&= \frac{n^2 e^2}{18\epsilon_0} \left(\frac{4\pi r^5}{5} \right), \tag{2.5}
\end{aligned}$$

where r' is a variable introduced to differentiate the integration variable from the upper integration limit in the radial direction. Setting the initial electron kinetic energy equal to the energy in the resulting electric field provides the relation

$$2\pi n k_B T r^3 = \frac{4\pi n^2 e^2 r^5}{90\epsilon_0}, \tag{2.6}$$

which may be solved to find the maximum radius, r , of a sphere that may spontaneously be evacuated of all electrons

$$r = \sqrt{\frac{45k_B T \epsilon_0}{ne^2}} \tag{2.7}$$

It is expected that the size of a region that can become completely depleted of electrons would be much smaller than a sphere described by the radius in Equation 2.7 since this approximation depends upon all electrons simultaneously traveling radially outward from a single point. Thus, the plasma may be considered quasi-neutral at lengths larger than $r \approx 463 (\text{K}\cdot\text{m})^{-1/2} \sqrt{T/n}$.

The quasi-neutrality condition breaks down near the boundaries of the plasma, referred to as the plasma sheath, where the electron and ion number densities are no longer equal. The physical extent of the sheath is measured by the Debye length (λ_D), which will be discussed further in Section 2.1.3.

2.1.3 Debye Shielding

The presence of charged surfaces in a plasma can disrupt the quasi-neutrality described above due to the excess of charges on the surface. Electrons and ions near the charged surface respond by being repelled (for like charges) or attracted (if oppositely charged), forming a cloud of opposite charges that shield the excess charge on the surface from the rest of the plasma. This is illustrated in Figure 2.3, where (a) a negatively charged dust grain, represented by a large dark green circle, is inserted into an otherwise neutral plasma. The dust grain exerts a force on other charges in the plasma, (b) accelerating ions (orange circles) toward the dust grain and electrons (small, light green circles) away from the dust grain along the directions indicated by the orange and green arrows, respectively, until (c) the cloud of ions shields the negatively charged dust grain from the rest of the plasma. The width of the shielding cloud that forms will depend on conditions in the plasma so that higher plasma density (more charges per unit volume) will tend to decrease the width of the shielding cloud, while plasma particles with a higher kinetic energy (higher ion and electron temperatures) will tend to increase the width of the shielding cloud. The process by which the oppositely charged shielding cloud forms is referred to as Debye shielding, and the Debye length (λ_D , illustrated by the light gray circle in Figure 2.3c) represents the distance at which the electric potential is decreased by a factor of $1/e$ relative to the surface of the dust grain.

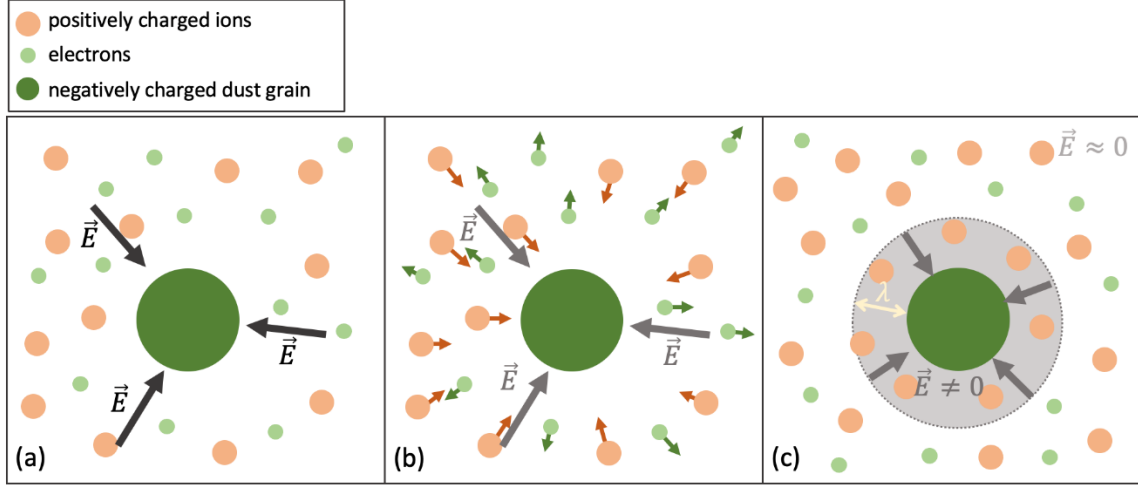


Figure 2.3 Illustration of the plasma response when a negatively charged dust grain, represented by the large dark green circle, is inserted into a neutral plasma (a). The electric field generated by the dust grain accelerates ions (orange circles) and electrons (small, light green circles) along the directions indicated by the orange and green arrows, respectively (b). A cloud of positively charged ions forms around the dust grain (c), with the width of the shielding cloud being the Debye length, λ_D , represented by the light gray circle.

To calculate the Debye length for a plasma, consider a neutral, uniformly distributed plasma with electron and ion densities, n_e and n_i , temperatures, T_e and T_i , and charges, q_e and q_i , where $q_e = -q_i = -e$, and e being the elementary charge $e = 1.6022 \times 10^{-19}$ C. Far from any disturbances in the plasma, the quasi-neutrality condition gives $n_{e0} = n_{i0} = n_0$. An electrostatic potential ϕ will be formed when a test charge is inserted into the plasma, and after the ions and electrons have reached a new equilibrium, the potential can be described by Poisson's equation

$$\nabla^2 \Phi = -\frac{\rho}{\epsilon_0}, \quad (2.8)$$

where the charge density $\rho = -e(n_i - n_e)$ is the sum of positive and negative charge densities. If the ions are assumed to have a fixed density, so that $n_i = n_{i0} = n_0$,

Poisson's equation becomes

$$\nabla^2 \Phi = -\frac{e}{\epsilon_0} (n_0 - n_e) \quad (2.9)$$

Next, the electron density, n_e , can be determined by integrating the velocity distribution function for electrons

$$\begin{aligned} n_e &= \int_0^\infty 4\pi n_{e0} \left(\frac{m_e}{2\pi k_B T_e} \right)^{\frac{3}{2}} \exp \left[-\frac{m_e v^2 - 2e\Phi}{2k_B T_e} \right] v^2 dv \\ &= n_0 \exp \left[\frac{e\Phi}{k_B T_e} \right]. \end{aligned} \quad (2.10)$$

Substituting the results from Equation 2.10 into 2.9 gives

$$\nabla^2 \Phi = -\frac{en_0}{\epsilon_0} \left(1 - \exp \left[\frac{e\Phi}{k_B T_e} \right] \right). \quad (2.11)$$

In the case that $|e\phi/k_B T_e| \ll 1$, which is satisfied when $\phi \ll k_B T_e/e \approx (8.62 \times 10^{-5} \text{ V}\cdot\text{K}^{-1})T_e$, the exponential term may be expanded using a Taylor series (keeping only the linear term)

$$\begin{aligned} \nabla^2 \Phi &\approx -\frac{en_0}{\epsilon_0} \left[1 - \left(1 + \frac{e\Phi}{k_B T_e} \right) \right] \\ &= \frac{e^2 n_0}{\epsilon_0 k_B T_e} \Phi. \end{aligned} \quad (2.12)$$

Taking advantage of the spherical symmetry of the system, this reduces to the one-dimensional equation

$$\frac{1}{r^2} \frac{\partial}{\partial r} \left(r^2 \frac{\partial \Phi}{\partial r} \right) = \frac{e^2 n_0}{\epsilon_0 k_B T_e} \Phi. \quad (2.13)$$

Then Equation 2.13 reduces to

$$\frac{\partial^2 \Phi}{\partial r^2} + \frac{2}{r} \frac{\partial \Phi}{\partial r} - \frac{e^2 n_0}{\epsilon_0 k_B T_e} \Phi = 0 \quad (2.14)$$

which may be solved to provide the solution

$$\Phi(r) = \frac{Q_d}{4\pi\epsilon_0} \exp \left[-\frac{r}{\lambda_D} \right] \quad (2.15)$$

where the first term represents the Coulomb potential when $r \ll \lambda_D$, and λ_D is the Debye length, defined as

$$\lambda_D = \sqrt{\frac{\epsilon_0 k_B T_e}{n_0 e^2}}. \quad (2.16)$$

2.2 Dust Grain Charging

2.2.1 Mechanisms of Dust Grain Charging

Surfaces in contact with a plasma will collect electrons and ions through random collisions, with the net charge on the surface determined by the balance of electron and ion currents. This process also applies to objects immersed in a plasma, such as micrometer-sized dust grains. A common method for estimating the charge on a dust grain is to determine the electron and ion charging currents using the Orbit Motion Limited (OML) method (described in Section 2.2.1.1). However, it is important to note that the charge collected by a dust grain is composed of many discrete collisions with electrons and ions rather than a continuous current, as suggested by the OML method. This will be discussed further in Section 2.2.1.2.

2.2.1.1 Orbit Motion Limited (OML) method. The OML method was first introduced by Mott-Smith and Langmuir in 1926 to describe an electrical discharge through gases by examining the I-V characteristics of an electrode immersed in the discharge. The OML method has since been further refined by Bohm, Burhop, and Massey in 1949, Allen, Boyd, and Reynolds in 1957, Laframboise in 1966, and Allen in 1992, among others. In the case of an uncharged dust grain, only ions and electrons with

an impact parameter smaller than the dust grain radius will be collected (illustrated in Figure 2.4a), so the collision cross-section is $\sigma = \pi r_d^2$. When the dust grain is charged, however, oppositely charged particles will be attracted and particles of the same sign will be repelled, increasing the impact parameter for oppositely charged particles and decreasing the impact parameter for particles of the same sign (illustrated in Figure 2.4b).

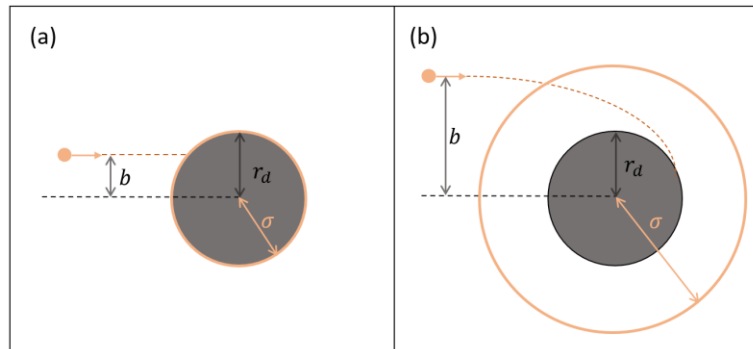


Figure 2.4 Illustration showing the trajectory of a charged particle (filled orange circle) moving toward (a) a neutral dust grain and (b) an oppositely charged dust grain. The collision cross-section, σ , is indicated by the solid orange circle in both panels and coincides with the dust grain radius for the uncharged dust grain. The attractive potential increases σ when the particles are oppositely charged, as in panel (b), and decreases σ when the particles have the same sign (not shown).

The effective cross-section for charged dust grains is needed to calculate the amount of charge collected by the grain and can be determined by examining the equations governing the motion of charged particles. Consider an incoming particle with charge q and mass m , moving toward a dust grain with surface potential ϕ_d . Let the initial velocity of the charged particle be v , and the final velocity when the charged particle collides with the dust grain be v_f . The constants of motion for a charged particle in the field near a small, spherical charged collector are the angular momentum ($J =$

mr_v) and the energy ($E = mv^2/2 + \phi$) (Allen 2000). The conservation of momentum and energy for a charged particle are then

$$mbv = mr_d v_f \quad (2.17a)$$

and

$$\frac{1}{2}mv^2 = \frac{1}{2}mv_f^2 + q\phi_d. \quad (2.17b)$$

Solving for the impact parameter, b , from Equations 2.17a and 2.17b yields

$$b = r_d \left(1 - \frac{2q\phi_d}{v^2 m}\right)^{1/2}, \quad (2.18)$$

so that the effective cross-section for a charged particle impacting a charged dust grain is $\sigma(v)_{\text{effective}} = \pi[r_d^2(1 - 2q\phi_d/v^2 m)] = \sigma(1 - 2q\phi_d/v^2 m)$. For electrons approaching a negatively charged dust grain, $q\phi_d > 0$ and the second term on the right of Equation 2.18 is negative, causing the effective cross-section to be smaller than the dust grain radius. If the incoming particle is an ion, $q\phi_d < 0$ and the second term on the right of Equation 2.18 is positive, resulting in an effective cross-section that is larger than the dust grain radius (Bellan 2008).

Using the collision cross-section for a charged dust grain, the electron and ion currents to the dust grain may be calculated by multiplying the cross-section by the velocity distribution and integrating over allowable velocities. Considering the particles to have a Maxwellian distribution, the integration becomes

$$I_i = \iiint q_i \sigma(\vec{v}) \vec{v} f(\vec{v}) d\vec{v} \quad (2.19)$$

where $f(\vec{v})$ is the Maxwell-Boltzmann distribution for velocity in three dimensions

$$f(\vec{v}) = n_0 \left(\frac{m}{2\pi k_B T}\right)^{\frac{3}{2}} \exp\left[-\frac{mv^2}{2k_B T}\right], \quad (2.20)$$

where $v^2 = v_x^2 + v_y^2 + v_z^2$. Substituting Equation 2.20 into 2.19 and using the expression for $\sigma(v)$ calculated previously, the integration may be written in spherical coordinates with $d\vec{v} = dv_x dv_y dv_z = 4\pi v^2 dv$

$$\begin{aligned}
I_i &= \int_0^\infty q_i \pi r_d^2 \left(1 - \frac{2q_i \phi_d}{v^2 m_i}\right) v n_i \left(\frac{m_i}{2\pi k_B T_i}\right)^{3/2} \exp\left[-\frac{m_i v^2}{2k_B T_i}\right] 4\pi v^2 dv \\
&= 4\pi^2 q_i r_d^2 n_i \left(\frac{m_i}{2\pi k_B T_i}\right)^{3/2} \int_0^\infty \left(1 - \frac{2q_i \phi_d}{v^2 m_i}\right) v^3 \exp\left[-\frac{m_i v^2}{2k_B T_i}\right] dv \\
&= 4\pi^2 q_i r_d^2 n_i \left(\frac{m_i}{2\pi k_B T_i}\right)^{3/2} \left\{ 2 \left[\left(\frac{k_B T_i}{m_i}\right)^2 - \frac{q_i \phi_d}{m_i} \left(\frac{k_B T_i}{m_i}\right) \right] \right\} \\
&= 4\pi q_i r_d^2 n_i \sqrt{\frac{k_B T_i}{2\pi m_i}} \left(1 - \frac{q_i \phi_d}{k_B T_i}\right) \tag{2.21}
\end{aligned}$$

In the case of electrons incident on a negative dust grain, only those electrons with a kinetic energy equal to the potential energy at the dust grain surface will be collected. As a result, any electron with a velocity less than $v_{\min} = \sqrt{2q_e \phi_d / m}$ will be deflected and will not contribute to the electron current to the dust grain. Calculating the current is then carried out in the same manner as for the ion collection, but with the lower bound of integration set to v_{\min} :

$$\begin{aligned}
I_e &= \int_{v_{\min}}^\infty q_e \pi r_d^2 \left(1 - \frac{2q_e \phi_d}{v^2 m_e}\right) v n_e \left(\frac{m_e}{2\pi k_B T_e}\right)^{3/2} \exp\left[-\frac{m_e v^2}{2k_B T_e}\right] 4\pi v^2 dv \\
&= 4\pi^2 q_e r_d^2 n_e \left(\frac{m_e}{2\pi k_B T_e}\right)^{3/2} \times \\
&\quad \left\{ \int_{v_{\min}}^\infty v^3 \exp\left[-\frac{m_e v^2}{2k_B T_e}\right] dv - \frac{2q_e \phi_d}{m_e} \int_{v_{\min}}^\infty v \exp\left[-\frac{m_e v^2}{2k_B T_e}\right] dv \right\} \tag{2.22}
\end{aligned}$$

Integrating the first integral by parts and simplifying the expression gives:

$$I_e = 4\pi q_e r_d^2 n_e \sqrt{\frac{k_B T_e}{2\pi m_e}} \exp\left[-\frac{q_e \phi_d}{k_B T_e}\right] \quad (2.23)$$

A neutral dust grain in a typical laboratory discharge in the absence of other charging mechanisms (e.g., photoemission, secondary electron emission, or thermionic emission) will quickly acquire a negative charge due to the electrons having a larger thermal velocity and colliding more frequently with the grain. The final equilibrium charge on the dust grain is given by the balance of the electron and ion currents to the grain surface so that $I_i + I_e = 0$. Setting Equation 2.21 equal to Equation 2.23 gives the relation

$$q_i n_i \sqrt{\frac{T_i m_e}{T_e m_i}} \left(1 - \frac{q_i \phi_d}{k_B T_i}\right) = -q_e n_e \exp\left[-\frac{q_e \phi_d}{k_B T_e}\right] \quad (2.24)$$

which may be solved numerically for particular values of electron and ion temperatures, densities, masses, and charges to determine an approximation for the surface potential of the dust grain, ϕ_d . In the case of singly-charged hydrogen, $q_i = -q_e = e$, $n_e = n_i$, and $T_i = T_e = T$, Equation (2.24) can be simplified to

$$\sqrt{\frac{m_e}{m_i}} \left(1 - \frac{e\Phi_d}{k_B T}\right) = \exp\left[\frac{e\Phi_d}{k_B T}\right], \quad (2.25)$$

and, using the values $m_i = 1.67 \times 10^{-27}$ kg and $m_e = 9.11 \times 10^{-31}$ kg, the classic Spitzer potential is recovered (shown in Figure 2.5):

$$\Phi_d = -2.5 \frac{k_B T}{e} \quad (2.26)$$

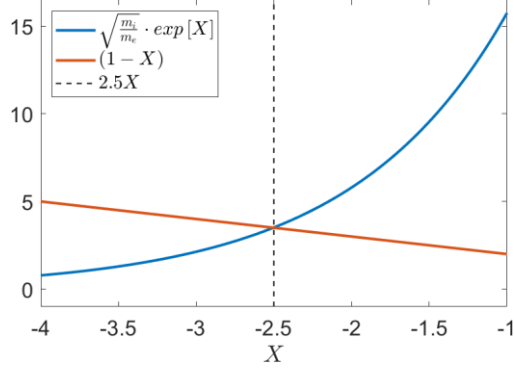


Figure 2.5 Plot of the left and right sides of Equation 2.26 for the case of singly-charged hydrogen with $X = e\Phi_d/k_B T$.

The charge on a spherical dust grain may be approximated by treating the dust grain as a spherical capacitor using the expression

$$Q_d = C\Phi_d, \quad (2.27)$$

where the capacitance C of the dust grain may be expressed as the capacitance of two concentric spheres with a separation distance λ_D using $C = 4\pi\epsilon_0(r_d + r_d^2/\lambda_D)$ (Whipple 1981). If the dust grain is small, so that $r_d \ll \lambda_D$, the capacitance reduces to $C = 4\pi\epsilon_0 r_d$, and the dust grain charge is $Q_d = 4\pi\epsilon_0 r_d \Phi_d$.

2.2.1.2 Discrete nature of charge collection. The charge collected by a dust grain may be approximated using the OML method, but the charging process does not follow a smooth curve, as suggested by the results in Equations 2.21 and 2.23. Rather, the dust grain collects discrete amounts of charge at each collision with an ion or dust grain, and the frequency of the collisions is best described by the probabilities (i) that any collision occurs and (ii) whether the collision is with an electron or an ion (Cui 1994, Goree 1994). Using these considerations, numerical simulations have shown that the charge on a dust grain fluctuates around the equilibrium charge, with fluctuations comprising a greater

percentage of the total charge as dust grain size is reduced due to the dependence of the total charge on the radius of the dust grain (Cui 1994, Goree 1994, Matthews 2018).

Results from numerical simulations using the discrete method of charging dust grains show good agreement between the average charge collected by a grain and the charge predicted by continuous charging models. However, it is important to consider the range of charge variation, particularly for small dust grains where the charge fluctuation may even result in the reversal of the dust grain charge under certain plasma conditions.

2.3 Timescales in a Complex (Dusty) Plasma

Complex plasmas are comprised of particles that span many orders of magnitude in size. As a result, there is a large variation in the characteristic timescales at which the particles respond to changes in the plasma environment. Relevant timescales for the electrons, ions, and dust grains can be determined by examining the response to local disturbances. Consider a neutral plasma comprised of a moveable slab of electrons with a uniform density that completely overlaps with a fixed slab of ions with a density equal to that of the electrons ($n_i = n_e = n_0$). If the slab of electrons is displaced relative to the fixed ions by a distance of L , there will be a region composed only of positive charges at one end of the plasma and a region composed only of negative charges at the other end. For this case, an electric field will form between the two charged regions, with a magnitude

$$E = \frac{en_0L}{\epsilon_0}. \quad (2.28)$$

When the displaced slab of electrons is released, the force from the electric field will accelerate the electrons according to the equation of motion

$$m_e \frac{d^2 L}{dt^2} = -eE \quad (2.29)$$

which may be rewritten using Equation (2.28) in the familiar form of a harmonic oscillator

$$\frac{d^2 L}{dt^2} = -\left(\frac{e^2 n_0}{m_e \epsilon_0}\right) L \quad (2.30)$$

with the solution $L(t) = L_0 \cos(\omega_{pe} t)$ where the frequency of oscillation is the electron plasma frequency (Gurnett 2005)

$$\omega_{pe} = \sqrt{\frac{e^2 n_0}{m_e \epsilon_0}}. \quad (2.31)$$

If the plasma consisted instead of a moveable slab of ions and a fixed slab of electrons, the ion plasma frequency determined following the same method gives

$$\omega_{pi} = \sqrt{\frac{e^2 n_0}{m_i \epsilon_0}}. \quad (2.32)$$

The electron and ion plasma frequency also define the characteristic timescales for the electrons and ions, τ_{pe} and τ_{pi} , called the electron plasma period and ion plasma period, respectively

$$\tau_{pe} = \frac{2\pi}{\omega_{pe}} = 2\pi \sqrt{\frac{m_e \epsilon_0}{e^2 n_0}} \quad (2.33)$$

$$\tau_{pi} = \frac{2\pi}{\omega_{pi}} = 2\pi \sqrt{\frac{m_i \epsilon_0}{e^2 n_0}}. \quad (2.34)$$

Relevant timescales for the motion of dust grains with charge Ze (where Z is the number of elementary charges on the dust grain, typically electrons) may be described by the dust plasma frequency and dust plasma period, which are defined in a method similar to the expressions derived for electrons and ions

$$\omega_{pd} = \sqrt{\frac{e^2 Z^2 n_d}{m_d \epsilon_0}} \quad (2.35)$$

and

$$\tau_{pd} = 2\pi \sqrt{\frac{m_d \epsilon_0}{e^2 Z^2 n_d}}. \quad (2.36)$$

The dust, ion, and electron masses may be ordered $m_d \gg m_i \gg m_e$, which allows the dust, ion, and electron plasma frequencies and plasma periods to be ranked $\omega_{pe} \gg \omega_{pi} \gg \omega_{pd}$ and $\tau_{pd} \gg \tau_{pi} \gg \tau_{pe}$. The difference in response times among the dust, ions, and electrons are commonly exploited in experiments and simulations, which will be discussed further in Chapter 3.

2.4 Ion Wakes

Ions in a plasma will drift along the direction of an applied electric field with a drift velocity, v_{di} , that is proportional to the strength of the electric field. Since ions are much lighter than charged dust grains, the dust grains can be considered fixed on the timescales relevant to ion motion. The positively charged ions in the vicinity of a negatively charged dust grain will be deflected from the original trajectory due to the attractive force of the dust grain. For ions with an impact parameter less than the collection radius, the deflection will cause the ions to collide with the dust grain (as illustrated in Figure 2.4b). For ions that are deflected by the dust grain but have an

impact parameter larger than the collection radius, the altered ion trajectories will overlap in a region downstream from the dust grain leading to an enhancement of the local ion density, commonly referred to as an ion wake. This effect is illustrated in Figure 2.6 for ions (small orange circles) flowing left to right past a dust grain (large gray circle).

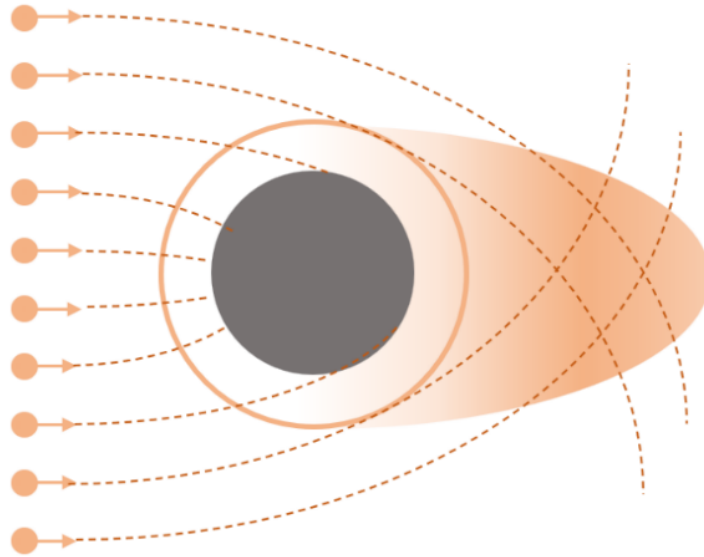


Figure 2.6 Illustration depicting the deflection of ions (small orange circles) flowing left to right in the vicinity of a charged dust grain (gray circle). The ions with an impact parameter less than the collection radius (open orange circle) are collected by the dust grain, while trajectories of ions with an impact parameter larger than the collection radius will intersect downstream from the dust grain. The region of enhanced ion density downstream from the dust grain is called the ion wake (semi-opaque orange region to the right of the dust grain).

Ions flowing past a dust grain in a DC electric field will form an asymmetric ion wake downstream from the dust grain, like the one shown in Figure 2.6. In contrast, if the electric field symmetrically switches directions at a frequency ω_{DC} (where $\omega_{pd} < \omega_{DC} < \omega_{pi}$), the ions will flow past the dust grain during both phases of the polarity switching and form a symmetric ion wake on both sides of the dust grain along the axis of the electric field (Figure 2.7).

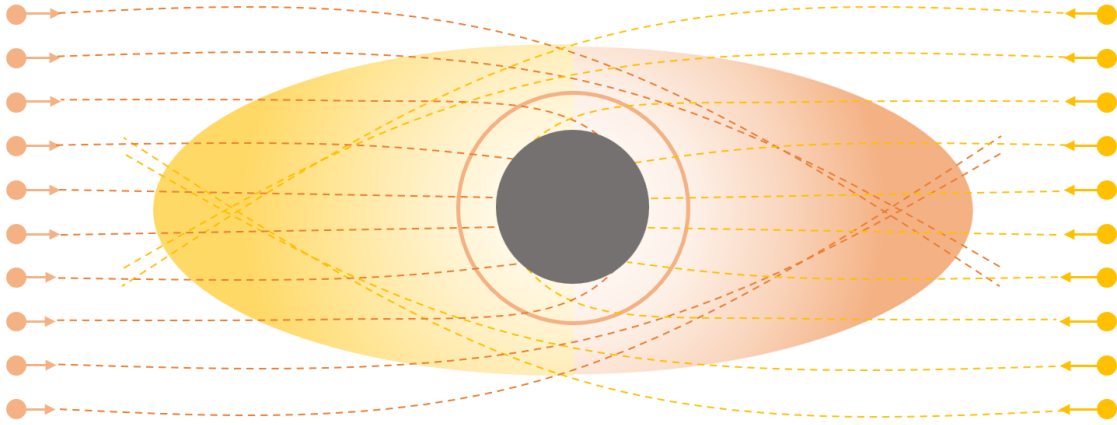


Figure 2.7 Illustration of the symmetric ion wake formed in the case of uniform polarity switching of the electric field direction. Ions flowing left to right (orange) form a wake to the right of the dust grain, while ions flowing right to left (yellow) form a wake to the left of the dust grain.

2.4.1 Ion Wake Characteristics

The location, size, and amount of charge contained in an ion wake are important features for determining the nature of interactions between other dust grains and the ion wake. These characteristics depend on the background plasma conditions as well as the charge, location, and number of dust grains immersed in the plasma.

2.4.1.1 Location of the ion wake. Since an ion wake forms as ions flow past a dust grain, the ion wake is not composed of a stationary set of ions, but rather describes a region through which a higher concentration of ions flow when compared to the rest of the plasma. In order to simplify calculations involving the ion wake location, the ion wake is often treated as a point charge (Ivlev 2000, Qiao 2013, Melzer 2014, Matthews 2020) with the location of the ion wake corresponding either to the position where the peak ion density value is found, or the center-of-charge in the wake (analogous to the

center-of-mass). The distance from a dust grain to the center-of-charge in the ion wake can be calculated using the equation

$$\ell_j = \left[\sum_{i=1}^N q_i (r_{j,i} - r_{j,\text{dust}}) \right] / \left[\sum_{i=1}^N q_i \right] \quad (2.37)$$

where the subscript j indicates the coordinate x , y , or z , N is the number of ions in the ion wake, q_i is the charge of the ion, $r_{j,i}$ is the position of the i^{th} ion, and $r_{j,\text{dust}}$ is the position of the dust grain. The point charge representation of an ion wake was found to poorly match experimental conditions in pressures less than 2 Pa (Banka 2022), but is expected to be reasonably reliable in cases where the dust grain and ion wake are relatively stable, for example as in a strongly-coupled dust structure (Matthews 2020).

2.4.1.2 Size of the ion wake. The spatial extent of the ion wake can be determined by calculating the region where the ion density is larger than the background ion density by a given threshold. Even in the absence of charged dust grains there will be statistical fluctuations in the ion density at any precise position in the plasma, so it is useful to set the threshold ion density value to be sufficiently above the background ion density value so that perturbations from the charged dust grain are isolated (typically $1.2 n_i/n_{i0}$ or larger).

The ion drift velocity is proportional to the strength of the electric field and, as shown in Equation 2.8, inversely proportional to the ion collection radius. This means that a charged dust grain will have a reduced influence on the trajectories of ions as the electric field strength increases, causing fewer ions to be collected by the dust grain and the point where ion trajectories overlap to move farther downstream from the dust grain. An illustration of this effect is shown in Figure 2.8, where an AC electric field is applied

to a series of dust grains with the strength of the electric field increasing from top to bottom rows in the figure. The size of the ion wake is extended along the ion flow direction as the axial electric field strength increases, and becomes narrower in the direction perpendicular to the ion flow.

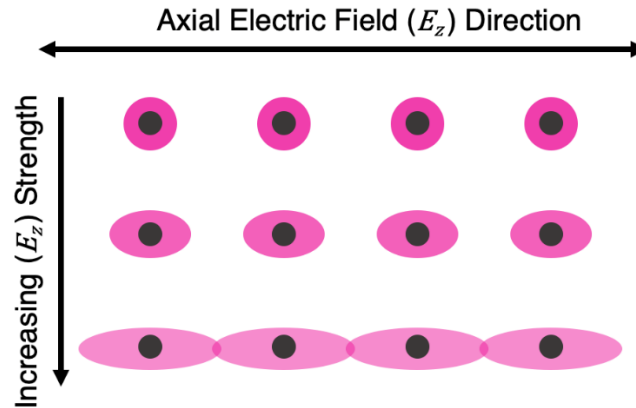


Figure 2.8 Illustration of the effect of increasing electric field strength on the location and extent of the ion wake (pink) near a chain of dust grains (black circles). The top row represents a case with no applied electric field, the middle row represents a moderate axial electric field, and the bottom row represents a large axial electric field.

2.4.1.3 Charge in the ion wake. Similar to the method of determining the size of the ion wake, the amount of charge in an ion wake can be determined by summing the average number of ions in the region where the ion density exceeds the background ion density by some threshold value. The charge in the wake determines the strength of attraction between the ion wake and other dust grains when considering the wake as a separate point charge, or reduces the effective charge on the dust grain when only considering dust-dust interactions.

CHAPTER THREE

Complex (Dusty) Plasma Experiments and Simulations

3.1 Plasmakristall-4 (PK-4) Microgravity Experiment

The Plasmakristall-4 (PK-4) microgravity dusty plasma experiment installed on the International Space Station (ISS) is the most recent iteration of a series of experiments that have been in place on the ISS since the turn of the century (Pustylnik 2016). The motivation for the series of microgravity experiments was to study three-dimensional complex plasma in an environment where large electric fields are not needed to compensate for the force of gravity on dust grains, allowing the relatively smaller dust-dust and dust-ion forces to dominate interactions. The Plasmakristall experiments have been used to study long-range phenomena, including the formation of liquid-like dust chains, three-dimensional phase transitions, dust acoustic waves, the transition between laminar and turbulent flow, lane formation, and shear flow instabilities (Usachev 2004, Dietz 2017, Thomas 2019). An overview of the experimental setup of the PK-4 ISS is provided in Section 3.1.1, and a brief outline of the results is presented in Section 3.1.2.

3.1.1 Experimental Equipment Setup

The PK-4 ISS is capable of generating either a DC or rf plasma within the glass plasma chamber. The chamber is composed of three 30-mm-diameter glass tubes welded together into a π -shaped configuration, illustrated in Figure 3.1. An electrode is placed at opposite ends of the discharge on the two 180-mm-long side tubes, and the gas flow is directed from the side tube with the active electrode to the side with the passive electrode

(clockwise in Figure 3.1). There are three dust dispensers on each side tube, labeled D1-D6 in Figure 3.1, which are attached at the connection between the side tubes and the main tube. The approximately 200-mm-long working area is positioned at the center of the 500-mm-long main tube and may be visualized by the particle observation cameras (labeled C1 and C2 in Figure 3.1), and the plasma glow observation camera (not shown). The optical manipulation laser enters the discharge through the flange at the left end of the main tube, and the illumination laser enters through the flange at the right end of the main tube (Pustylnik 2016).

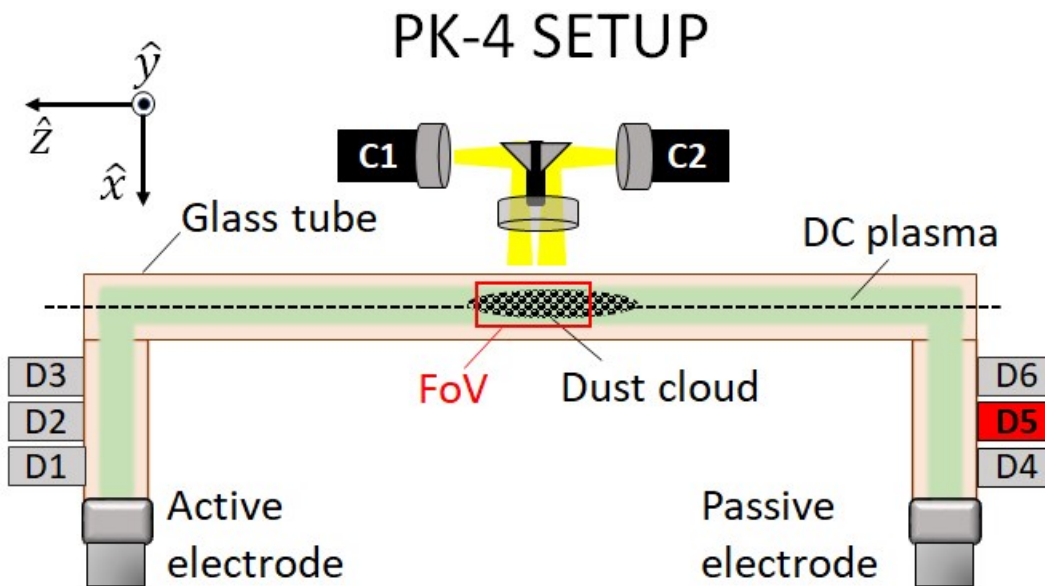


Figure 3.1 Illustration of the PK-4 ISS experiment showing the π -shaped plasma chamber, dust dispensers (labeled D1-D6), active and passive electrodes, particle observation cameras (C1 and C2), and the field-of-view (FoV) for imaging the experiment. [this figure was originally published in (Vermillion 2021)]

The plasma in the PK-4 may be generated from neon or argon, and working neutral gas pressure can be set between 10-200 Pa. The DC discharge in the PK-4 is generated by a high-voltage power supply which can provide up to a 3.1 mA current at

2.7 kV and operates in either a pulse generator or arbitrary generator mode. The pulse generator mode is used for polarity switching procedures, where the magnitude of the current is constant and the polarity (and axial electric field direction) reverses at the specified time intervals (Pustylnik 2016). If the polarity switching is employed with equal positive and negative polarity durations at a frequency $\omega_{DC} > \omega_{pd}$, the dust grains immersed in the plasma are unable to respond to a given polarity direction before it reverses, and the dust will be trapped. However, if the polarity switching is asymmetric, the dust grains will experience a net force and will be pushed along the discharge tube. In this manner, dust inserted at the dust dispensers may be transported along the discharge tube to the working area, held fixed within the field-of-view for the desired duration, and finally flushed from the discharge chamber.

The plasma glow in the PK-4 ISS is visualized using the plasma glow observation (PGO) camera, a 640×480 pixel video camera with a 25 fps frame rate. The PGO camera images the plasma chamber through three filters: (i) 703.2 nm spectral line of neon, (ii) 585.2 nm spectral line of neon, and (iii) a neutral filter that registers light generated by the plasma and light scattered off of the dust grains from the illumination and manipulation lasers (Pustylnik 2016). The neutral filter can therefore be used to observe the overall distribution of dust grains within the discharge chamber.

The dust is visualized using the particle observation (PO) cameras, which are 1600×1200 pixel video cameras with up to 35 fps frame rate at maximum resolution, or about 70 fps with a resolution of 1600×480 pixels. Each pixel in PO camera 1 corresponds to $14.18 \pm 0.02 \times 14.25 \pm 0.02$ $\mu\text{m}/\text{pixel}$ (horizontal \times vertical), and

$14.20 \pm 0.03 \times 14.31 \pm 0.03 \mu\text{m}/\text{pixel}$ (horizontal \times vertical) for PO camera 2 (Pustylnik 2016).

3.1.2 Experimental Results

Analysis of footage obtained from the Plasmakristall microgravity experiments has revealed interesting phenomena, including self-excited or externally excited dust acoustic and dust density waves, turbulence, phase transitions, and liquid-like dust chains aligned along the axial electric field direction (Usachev 2004, Ivlev 2008, Ivlev 2011, Dietz 2017, Thomas 2019, Pustylnik 2020, Dietz 2021).

It has been observed that dust grains can be triggered to organize into chains by adjusting the polarity switching of the electric field. The transition from isotropic dust to fluid-like dust chains can be forced in the Plasmakristall experiment by adjusting the field switching from a constant DC electric field to an AC electric field with completely symmetric polarity switching. The transition back to isotropic from fluid-like dust chains occurs as the polarity switching becomes more asymmetric (Ivlev 2011, Dietz 2021). The mechanism responsible for dust chain formation is still an active area of research, but one common theory is that the symmetry of the ion wakes that form in an AC field are responsible for the stability of the dust chains, while the interactions between charged dust grains and the asymmetric ion wakes that form in a DC field lead to non-reciprocal interactions and decreased dust chain stability. The interaction energy between a pair of charged dust grains has been described using an expansion of the wake potential over the ion drift velocity resulting in the equation

$$W(r, \theta) \cong Q^2 \left[\frac{e^{-r\lambda}}{r} - 2 \sqrt{\frac{2}{\pi}} \frac{M_T \lambda^2}{r^3} \cos \theta - 0.43 \frac{M_T^2 \lambda^2}{r^3} (3 \cos^2 \theta - 1) + \dots \right] \quad (3.1)$$

for a DC electric field (Ivlev 2011), and

$$W(r, \theta) \cong Q^2 \left[\frac{e^{-r/\lambda}}{r} - 0.43 \frac{M_T^2 \lambda^2}{r^3} (3 \cos^2 \theta - 1) \right] \quad (3.2)$$

in the case of an AC electric field, where θ is the angle between the electric field and \vec{r} it the separation between the two dust grains, $M_T^2 = \langle u_i^2 \rangle / v_T^2$ is the thermal Mach number, $v_T^2 = T_n / m_i$ is the thermal velocity of the ions, and λ is the shielding length (Ivlev 2008). However, dust chains have been observed to form in the PK-4 at Mach numbers much lower than the threshold values predicted using Equations 3.1 and 3.2.

3.2 Ground-Based Experiments

Comparisons with the microgravity PK-4 experiments can be performed using ground-based complex plasma experiments, including the PK-4BU at Baylor University in Waco, Texas, and the BUD-DC operated in Budapest, Hungary.

3.2.1 PK-4BU Experimental Equipment Setup

The PK-4BU is a ground-based replica of the PK-4 ISS, with hardware chosen to be as close as possible to the hardware used on the PK-4 ISS. A photo of the PK-4BU experiment is provided in Figure 3.2, with relevant components labeled. The plasma discharge in the PK-4BU is composed of a π -shaped, 30-mm inner diameter cylindrical quartz glass tube, appearing filled with a bright pink plasma in Figure 3.2. The active electrode is positioned on the same side tube as the gas inflow (shown on the left in Figure 3.2) and is connected to a high voltage power supply capable of operation in polarity switching mode with a frequency up to 1000 Hz. The passive electrode is attached to the opposite side tube, and illumination and manipulation lasers are positioned at each end of the main tube. The dust shaker is positioned near the

connection between the left side tube and the main tube in the upper left corner of Figure 3.2.

Experiments using the PK-4BU are imaged using two Photron Fastcam Mini UX 50 high-speed cameras capable of a frame rate of 2,000 fps at 1280×1024 pixel resolution or 2,500 fps at 1280×800 pixel resolution. The side view camera is positioned along the side of the discharge tube, and the top view camera is positioned above the discharge tube (viewing the main tube at 90° to the first camera). The discharge can also be simultaneously observed using a Basler pilot piA1600-35gc camera capable of a frame rate of 35 fps at 1608×1208 pixel resolution (not shown in Figure 3.2). The PK-4BU apparatus is attached to a table that can be rotated so that the main discharge tube may be positioned parallel or perpendicular to the direction of the Earth's gravitational force (Schmidt 2020).

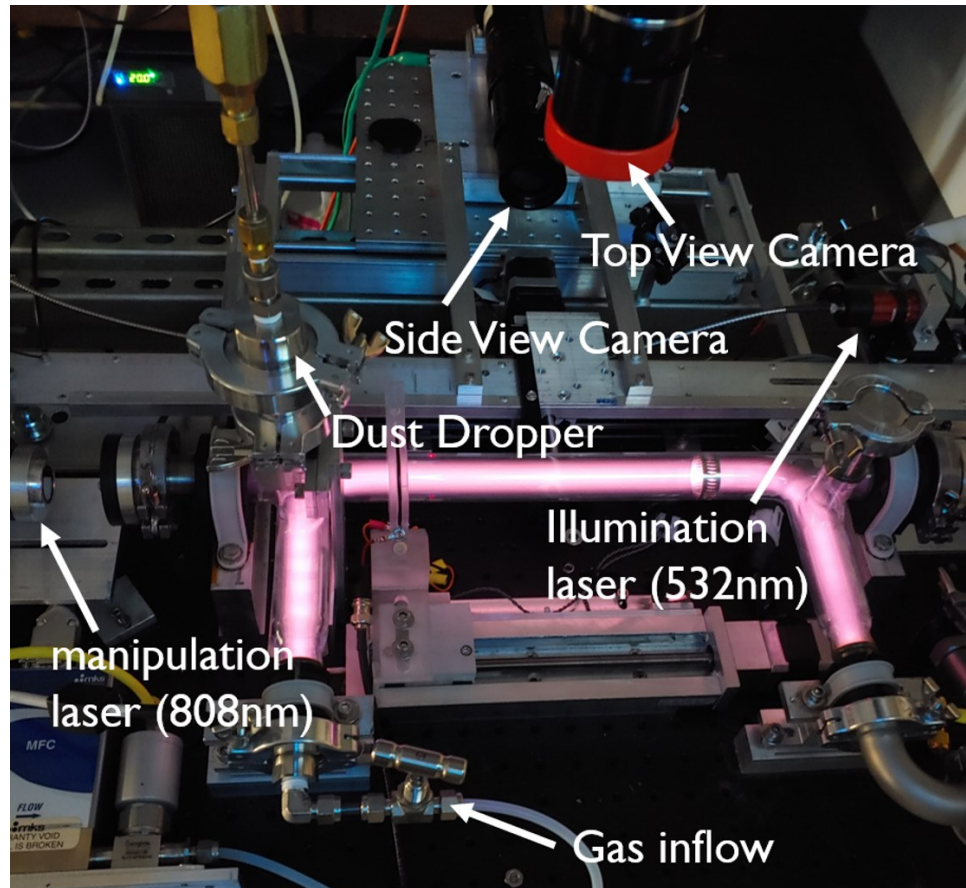


Figure 3.2 Photo of the PK-4BU showing the position of the side view camera, top view camera, illumination laser, gas inflow, manipulation laser, and dust dropper (clockwise from top). Photo credit: CASPER, Hyde Lab, Parker Adamson.

3.2.2 BUD-DC Experimental Equipment Setup

The BUD-DC experiment is composed of a 30-mm inner diameter straight cylindrical glass discharge tube. The flat active and passive electrodes are placed 400 mm apart on the ends of the discharge tube, with the active electrode powered by a DC power supply. Observation of the BUD-DC is performed using an Allied Vision Prosilica GX1050 CCD camera capable of 112 fps at the maximum 1024×1024 pixel resolution, and single channel light intensity measurements are obtained using a Hamamatsu H7732P-11 photomultiplier tube based photon counting module (Hartmann

2020). The BUD-DC experiment is designed to resemble the PK-4BU experiment, while also closely matching the geometry used in Particle-in-Cell with Monte Carlo Collisions (PIC-MCC) simulations of the discharge (Hartmann 2020).

3.2.3 PK-4BU and BUD-DC Experimental Results

High-speed video data collected in the PK-4BU experiment and PIC-MCC simulations of the BUD-DC experiment revealed the presence of fast-moving ionization waves in the positive column of the DC plasma, shown in Figure 3.3. The characteristics of these ionization waves were found to depend on the neutral gas pressure, as can be seen when comparing electron and ion temperatures obtained at 40 Pa (Figure 3.4) with those obtained at 60 Pa (Figure 3.5). The ionization waves at 40 Pa generated fluctuations in plasma parameters which were separated by periods when the parameters returned to values near the background values. This is exemplified in the large peaks in the ion temperature in Figure 3.4 which are separated by more than 150 μs between ionization wave fronts, during which time the ions are able to thermalize with the neutral gas (Matthews 2021). In contrast, the ion temperature in Figure 3.5 is found to undergo large fluctuations which persist throughout the simulation, and although the electron temperature exhibits period peaks, the value of the electron temperature remains in constant flux with variable minimum and maximum values. Since the formation of dust structures is dependent on the attractive force arising from the ion wakes, the difference in characteristics of ionization waves at 40 and 60 Pa is likely to have a measurable impact on the formation and stability of dust chains formed in the PK-4.

The observed ionization waves have a phase velocity ranging from 500-1200 m/s in neon plasma, with plasma parameters such as the ion and electron densities, electric

field, and drift velocity undergoing large oscillations during the peak-to-peak time for the ionization waves (Hartmann 2020). Specific findings from the analysis are presented in Chapter 4.

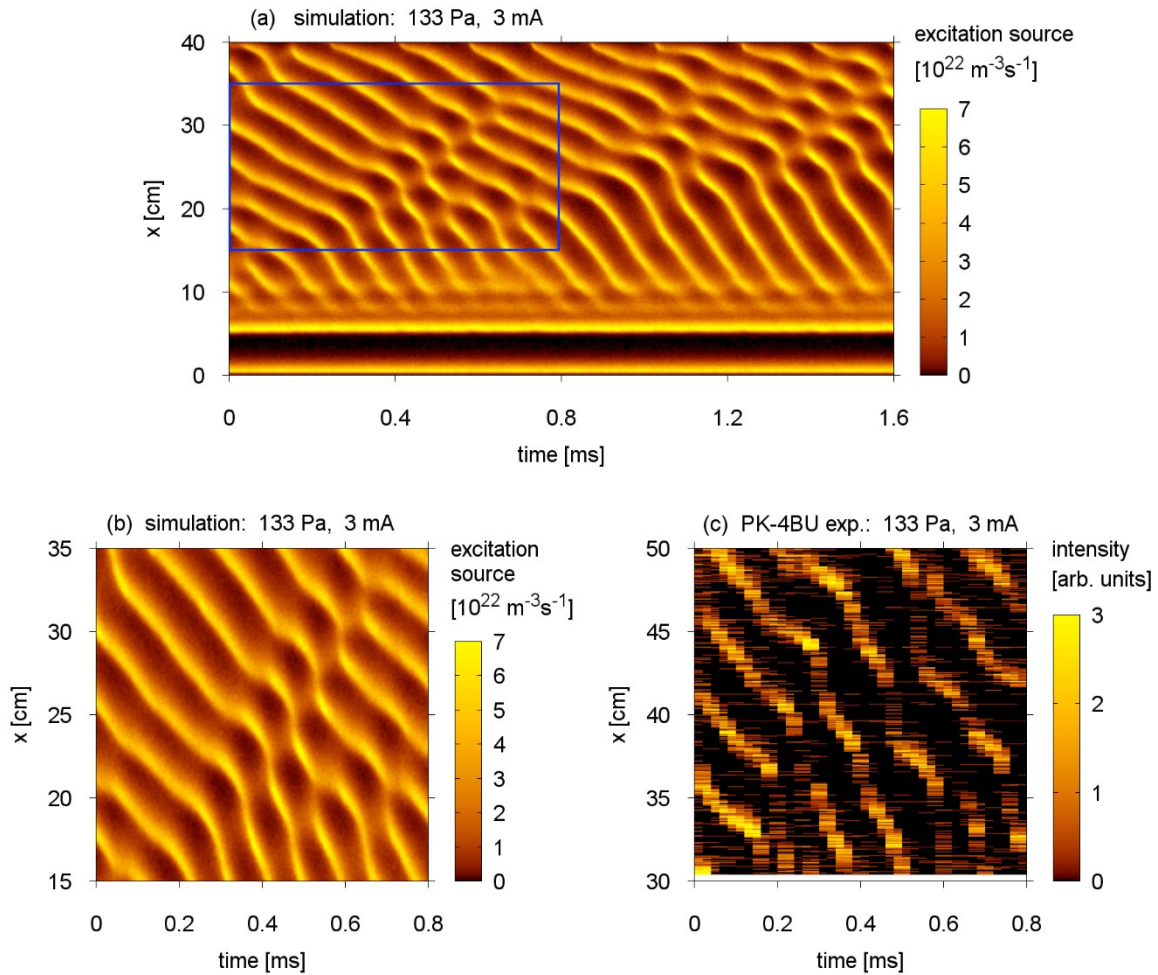


Figure 3.3 Ionization waves observed in (a) the PIC-MCC simulations of the BUD-DC experiment at 133 Pa with discharge current of 3 mA. The blue rectangular area of panel (a) is shown in more detail in panel (b), which is compared with the PK-4BU experimental results in (c). [Image originally published in Hartmann 2020]

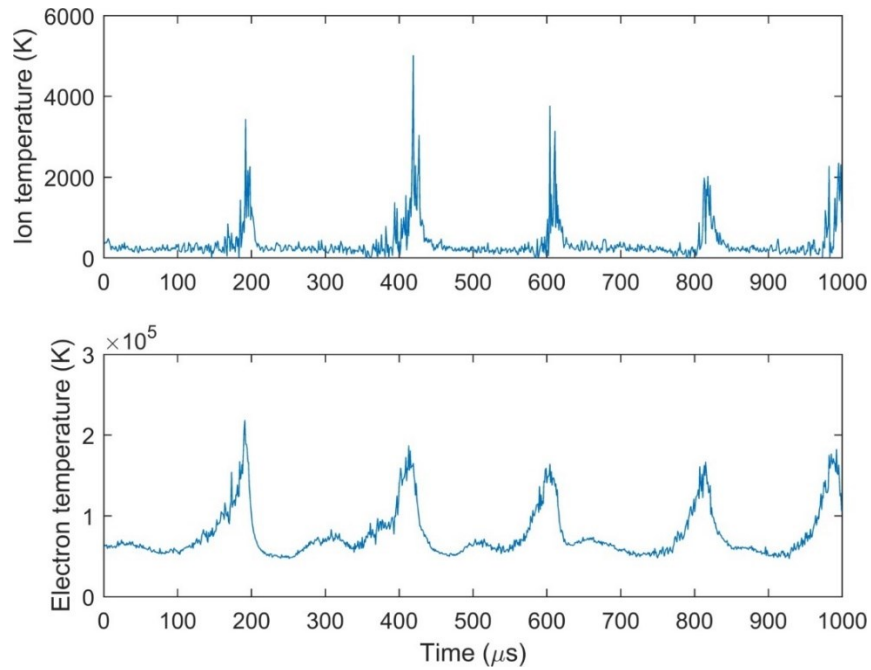


Figure 3.4 Ion (top) and electron (bottom) temperatures obtained from PIC-MCC simulation of the BUD-DC discharge at 40 Pa neutral gas pressure.

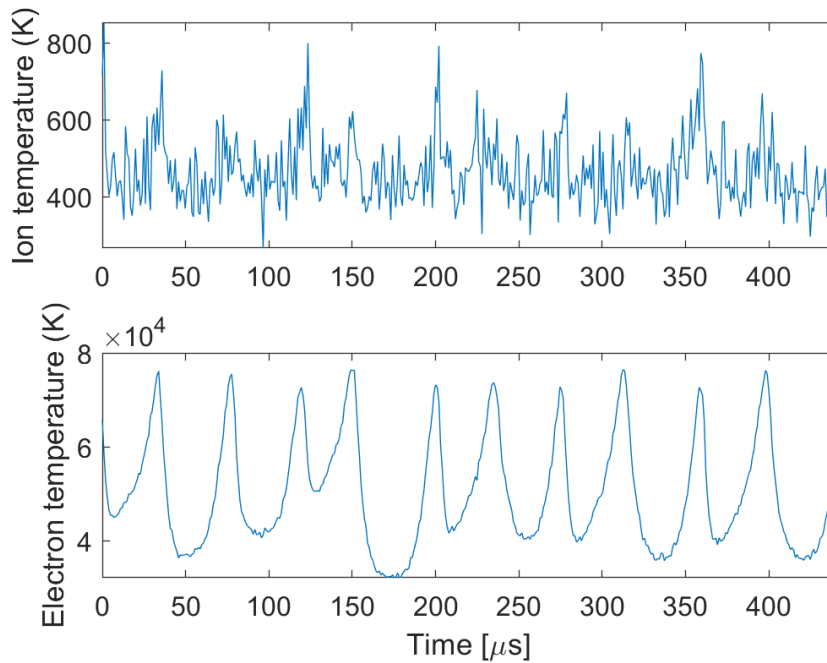


Figure 3.5 Ion (top) and electron (bottom) temperatures obtained from PIC-MCC simulations of the BUD-DC discharge at 60 Pa neutral gas pressure.

3.3 Dynamic Response of Ions And Dust (DRIAD) Simulation

DRIAD is a molecular dynamics simulation that was developed to model the motion of ions and dust grains, each on their own timescales, as well as the variations of dust grain charge in response to the changing ion concentrations. The code is implemented following the molecular asymmetric dynamics (MAD) code outlined in Piel (2017), where the nonlinear shielding of a dust grain by the ions is approximated by treating the force on ions by dust grains as a Coulomb force and the force on dust grains from ions as a shielded Yukawa force. Details of the implementation of the asymmetric treatment of forces are provided in Matthews (2020) and outlined below. The number of individual ions contained in a simulation region would be intractable to model individually, even using modern parallel computation techniques. Instead, DRIAD models superions which each represent 100-200 individual ions. The charge-to-mass ratio of an individual ion is preserved, and the equations of motion that would describe a single ion are therefore applicable for calculations involving superions.

3.3.1 Ion Motion

The motion of an ion with mass m_i is governed by the equation of motion

$$m_i \ddot{\vec{r}} = \vec{F}_{ij} + \vec{F}_{iD} + \vec{F}_E(z) + \vec{F}_{bound}(r, z) + \vec{F}_{in}. \quad (3.3)$$

The electrostatic force, \vec{F}_{ij} , between ion i and ion j is derived from a Yukawa potential

$$\vec{F}_{ij} = \sum_{i \neq j}^{N_i} \frac{q_i q_j}{4\pi \epsilon_0 r_{ij}^3} \left(1 + \frac{r_{ij}}{\lambda_{De}}\right) \exp\left(-\frac{r_{ij}}{\lambda_{De}}\right) \vec{r}_{ij}, \quad (3.4)$$

where q_i and q_j are the charge of ions i and j , respectively, and r_{ij} is the distance between ions i and j . The shielding for ion-ion interactions is provided by the electrons,

so the shielding length used in Equation 3.4 corresponds to the electron Debye length,

$$\lambda_{De} = \sqrt{\epsilon_0 k_B T_e / (n_e e^2)},$$
 as discussed in Section 2.1.3.

The region near the negatively charged dust grain is depleted of electrons, so the force exerted by the dust grains on the i^{th} ion, \vec{F}_{iD} , is derived from a bare Coulomb potential

$$\vec{F}_{iD} = \sum_d^{N_D} \frac{q_i Q_d}{4\pi\epsilon_0 r_{id}^3} \vec{r}_{id}, \quad (3.5)$$

where Q_d is the charge of dust grain d and r_{id} is the distance from dust grain d to the i^{th} ion.

The force on the ions due to the applied electric field, $\vec{E}(z)$, is

$$\vec{F}(z) = q_i \vec{E}(z) \quad (3.6)$$

where the electric field is directed along the center axis of the simulation cylinder. The applied electric field is set as a constant value, and polarity switching of the electric field may be added so the direction of the applied electric field reverses at the desired frequency.

The ions outside the simulation (which are not directly modeled) exert a force on ions inside the simulation through a bounding electric field, $\vec{F}_{bound}(r, z) = q_i \vec{E}_{bound}(r, z)$. The bounding electric field is taken to be the negative gradient of the potential inside a cylindrical cavity in an otherwise homogeneous distribution of ions, $\vec{E}_{bound}(r, z) = -\nabla\Phi_{cavity}$. To determine the electric potential in a cylindrical cavity, it is first assumed that ions outside the cylinder are uniformly distributed and extend to distances far from the simulation region (effectively considering the uniform distribution to extend in $r, z \rightarrow \infty$). In such a situation, the electric potential at all points will be the

same and equal to a constant value, $\Phi_{total} = c$. Next, the uniform distribution of ions is subdivided so that the ions inside the simulation bounds and ions outside the simulation bounds are considered separately, Φ_{in} and Φ_{out} , respectively. The sum of the two regions will still be equal to a constant value since no other changes have been made, which gives $\Phi_{total} = \Phi_{in} + \Phi_{out}$. If the ions within the simulation boundary are then removed from the uniform distribution of ions, the remaining potential is $\Phi_{total} - \Phi_{in} = \Phi_{out}$. Since the total potential is just a constant value, $\Phi_{out} = c - \Phi_{in}$ (illustrated in Figure 3.3). Thus, the potential from the ions outside the simulation is equivalent to the potential of a cylinder of uniformly distributed ions subtracted from a constant value.

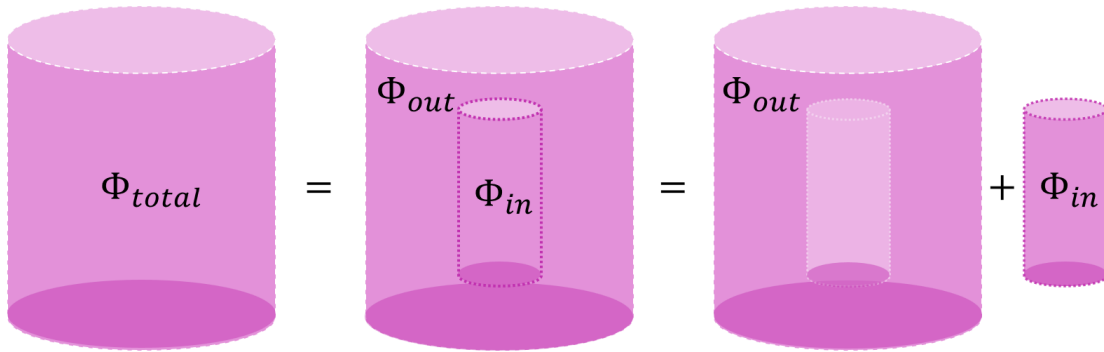


Figure 3.6 Illustration depicting the calculation of the potential from ions outside the simulation region (Φ_{out}) as the potential from ions inside the simulation region (Φ_{in}) subtracted from the total potential (Φ_d).

Ion-neutral collisions, \vec{F}_{in} , in DRIAD are treated using the null-collision method (Skullerud 1968, Donko 2011), where the isotropic and backscattering cross-sectional collision data are taken from the Phelps database (hosted by LXCat project) (Carbone 2021). At each timestep, the number of ions which undergo ion-neutral collisions is calculated, and then those ions which are selected for collision are collided with a target

randomly selected from a Maxwellian distribution. This method is faster since a random variable is not chosen for each ion at each timestep, rather all the ions are considered collectively and a random set of ions is chosen to undergo collisions.

Due to the large difference in timescales of motion between the ions and dust grains, the ion motions are allowed to evolve to equilibrium while the dust grains are held fixed, after which time the dust grain motion will step forward one timestep in response to the new configuration of ions. The ion motion is calculated with a timestep on the order of $\Delta t_i = 0.01 \mu\text{s}$, and 100-1000 ion timesteps (N_{t_i}) are calculated between each dust timestep. The user sets the ion timestep length and the number of ion timesteps for each dust timestep when initializing DRIAD so that $N_{t_i} \times \Delta t_i$ is sufficient to allow the ions to reach equilibrium before the next dust timestep.

3.3.2 Dust Motion

The motion of a dust grain with mass m_d and charge Q_d at the position \vec{r} is given by the equation of motion

$$m_d \ddot{\vec{r}} = \vec{F}_{di} + \vec{F}_{dD} + \vec{F}_E(z) + \vec{F}_{drag} + \vec{F}_B + \vec{F}_C. \quad (3.7)$$

The force of ions acting on dust grains, \vec{F}_{di} , is calculated at each ion timestep. In contrast to the force of the dust on the ion, the force of the ions on the dust is taken to be a Yukawa potential

$$\vec{F}_{di} = \frac{1}{N_{t_i}} \sum_{t_i=1}^{N_{t_i}} \sum_{i=1}^{N_i} \frac{q_i Q_d}{4\pi\epsilon_0 r_{di}^3(t_i)} \left(1 + \frac{r_{di}(t_i)}{\lambda_{De}}\right) \exp\left(-\frac{r_{di}(t_i)}{\lambda_{De}}\right) \vec{r}_{id}(t_i), \quad (3.8)$$

where $r_{di}(t_i)$ is the distance between the i^{th} ion and dust grain d at ion timestep t_i . This asymmetric treatment of the ion and dust forces has been shown to preserve the nature of

the ion wakefield (Piel 2007). At each dust timestep, the cumulative force of the ions acting on the dust grain is averaged over the elapsed number of ion timesteps that have occurred since the previous dust timestep.

In the case of dust-dust interactions, the plasma shielding is generally due to the ions. Since the ions are modeled explicitly in the simulation, the force between dust grains, \vec{F}_{dD} , is treated as a Coulomb interaction

$$\vec{F}_{dD} = \sum_{d=1}^{n_d} \frac{Q_d Q_D}{4\pi\epsilon_0 r_{dD}^3} \vec{r}_{dD} \quad (3.9)$$

where Q_d and Q_D are the charges on dust grains d and D , respectively, and r_{dD} is the distance between dust grains d and D .

The force on the dust grains due to the DC electric fields present in the discharge tube is $\vec{F}_E(z) = Q_d \vec{E}(z)$, where $\vec{E}(z)$ is the electric field applied along the central axis of the simulation cylinder. If polarity switching is used, the electric field will reverse directions at the specified time interval, otherwise, the electric field will remain constant. The electric field could also represent the electric field in the plasma sheath in ground-based complex plasma experiments.

The neutral gas exerts a drag force on the dust grains proportional to the velocity of the gas with respect to the dust, $\vec{F}_{drag} = m_d \beta \vec{v}$, where the constant of proportionality, β , is given by

$$\beta = \delta \frac{4 r_d^2 P}{3 m_d} \sqrt{\frac{8\pi m_g}{k_B T_n}} \quad (3.10)$$

with a material-dependent coefficient δ ($\delta \approx 1.44$ for the case of melamine formaldehyde dust in argon gas), neutral gas pressure P , the neutral gas atom mass m_g , and neutral gas temperature T_n .

The random thermal motions resulting from the dust being immersed in a thermal bath are included through the force $\vec{F}_B = \eta(t) \cdot \zeta$, where $\eta(t)$ is a normally distributed random number centered about zero selected using

$$\eta(t) = \cos(2\pi x_2) \sqrt{-2 \log(x_1)} \quad (3.11)$$

where x_1 and x_2 are numbers between 0 and 1, which are generated using the C++ standard library. The random number determined by Equation 3.11 at each timestep represents a scaling factor for ζ , so that the correlation of the dust motion gives the dust a set temperature, where ζ is given by

$$\zeta = \sqrt{\frac{2\beta k_B T_n}{m_d \Delta t_d}}. \quad (3.12)$$

The confinement force, \vec{F}_C , is added to the dust grains to simulate the experimental conditions. In the case of simulating dust in a PK-4 environment, \vec{F}_C adds the force that dust grains in the simulation would experience from dust grains outside the simulation. In the case of simulating dust grains in a terrestrial plasma, the confining force may be provided by a confining potential imposed to trap the dust in a particular region of an experiment, such as an inset in the lower electrode of a GEC reference cell or a glass box used to add horizontal confinement for vertical dust structures.

When dust grains are simulated in a microgravity environment, Equation 3.7 represents the complete equation of motion. If the dust grains are simulated in a terrestrial environment, another force due to Earth's gravity must be added, which is

equal to $\vec{F}_G = m_d \vec{g}$, and the force of the applied electric field must be sufficient to levitate the dust grain against the additional force of gravity.

3.3.3 Dust Grain Charging

Dust grains in DRIAD charge due to electron and ion currents to the dust grain surface. Since the simulation does not model the motion of the electrons directly, the electron current to the dust grain is calculated using OML theory (described in Section 2.2), assuming the electrons follow a Boltzmann-distribution

$$I_e = 4\pi r_d^2 n_e e \left(\frac{k_B T_e}{2\pi m_e} \right)^{\frac{1}{2}} \exp\left(\frac{e\Phi_d}{k_B T_e} \right). \quad (3.13)$$

The ion current to the dust grain consists of the N_i ions that cross the collection radius b_c ,

$$b_c = r_d \left(1 - \frac{2q_i \Phi_d}{m_i v_s^2} \right)^{\frac{1}{2}} \quad (3.14)$$

where v_s is the characteristic velocity of the ions

$$v_s = \left(\frac{8k_B T_i}{\pi m_i} + v_i^2 \right)^{\frac{1}{2}} \quad (3.15)$$

and v_i is the drift speed of an ion, which can be related to the sound speed, c_s , through the relation $v_i = M c_s$. The charge collected by the dust grain during a timestep is then the sum of the electron and ion currents

$$\Delta Q_d = I_e \Delta t + N_i Q_i \quad (3.16)$$

with fluctuations in the charge occurring due to the discrete nature of ion collection.

Since each ion collection event adds the amount of charge contained in a superion (with the charge in a single superion $Q_I \approx 200q_i$), the expected fluctuations due to discrete

charging are exaggerated. This is resolved by using a weighted average to update the dust grain charge at each timestep of the form

$$Q_d(t) = 0.95 \cdot Q_d(t - 1) + 0.05 \cdot Q_{avg}(t) \quad (3.17)$$

where $Q_{avg}(t)$ is the average of the charge added at each of the 100-200 ion timesteps during the current dust timestep multiplied by the dust timestep.

CHAPTER FOUR

Influence of Temporal Variations in Plasma Conditions on the Electric Potential Near Self-Organized Dust Chains

This chapter was published as [1]: Katrina Vermillion, Dustin Sanford, Lorin Matthews, Peter Hartmann, Marlene Rosenberg, Evdokiya Kostadinova, Jorge Carmona-Reyes, Truell Hyde, Andrey Lipaev, Alexandr D. Usachev, Andrey V. Zobnin, Oleg F. Petrov, Markus H. Thoma, Mikhail Y. Pustynnik, Hubertus M. Thomas, Alexey Ovchinin, “Influence of temporal variations in plasma conditions on the electric potential near self-organized dust chains,” *Physics of Plasmas* 29, 023701, (2022).

4.1 Introduction

The self-organization of dust grains in a flowing plasma offers insight into the interplay among charged species in a complex plasma environment. Ground-based experiments have studied the formation of dust structures in the sheath region of a plasma (Kompaneets 2007), where a large vertical electric field is required to balance the gravitational force acting on the dust particles. Ions drift relative to the more massive dust grains, with the ion drift velocity (v_i) corresponding to the strength of the applied electric field. The presence of positively charged ion wakes is thought to be responsible for the non-reciprocal interactions that have been observed between negatively charged dust grains in a flowing plasma (Ivlev 2015, Kliushnychenko 2017).

In contrast, microgravity dusty plasma experiments performed on parabolic flights (Thoma 2006) or on the International Space Station (currently through the Plasmakristall-4, PK-4, experiment) (Fortov 2005a, Ivlev 2011, Khrapak 2016, Thoma 2010, Pustynnik 2016, Thomas 2019) enable investigations of dust dynamics in the near-absence of gravitational influence, where the smaller effects from the dust-dust, dust-ion, and drag

forces are the primary drivers of the dust motion. In microgravity experiments, the dust cloud can be levitated within the bulk of the discharge plasma where electric fields are weaker, and ion flow speeds are lower, than typically found in a plasma sheath. In order to confine the dust within the field of view, the polarity of the DC discharge of the PK-4 device undergoes polarity switching at a frequency $\omega_{pi} > \omega_{ps} > \omega_{pd}$ (where ω_{pi} is the ion plasma frequency, ω_{ps} is the polarity switching frequency, and ω_{pd} is the dust plasma frequency). As a result, the regions of enhanced ion density are symmetrically stretched along the direction parallel to the external electric field (illustrated in Figure 4.1). This allows for a more detailed examination of the interaction between dust grains and the surrounding plasma environment, especially as it relates to the formation of dust particle chains, dust density waves, and other interesting phenomena which have previously been reported (Arp 2012, Zobnin 2018, Takahashi 2019, Pustyl'nik 2020, Dietz 2021). The complex interactions between ion wakes and the charged dust grains are thought to guide the homogeneous-to-string transition (Lipaev 1997, Fortov 1997, Melzer 1996, Melzer 1999), resulting in behavior similar to that observed in conventional electrorheological (ER) fluids (Ivlev 2008).

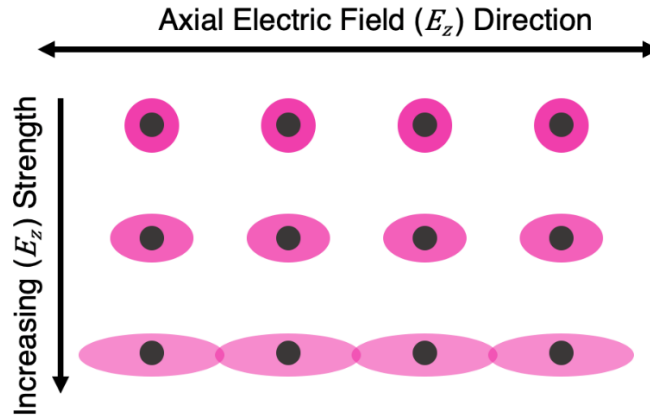


Figure 4.1 Illustration showing the qualitative behavior of the shielding ion cloud surrounding dust grains as the alternating axial electric field strength (E_z) increases. In the top row, representing $E_z = 0$, the shielding cloud is spherical and close to the dust grain. In the middle row, representing a moderate increase in E_z , the shielding ion clouds begin to stretch in the axial direction. In the bottom row, representing E_z above a critical value, the ion clouds are even more distorted and stretch across the entire region between individual dust grains.

Recent ground-based observations of ionization waves under the conditions present in the PK-4 experiment have been reported (Hartmann 2020), and the impact that these observed ionization waves can have upon the plasma parameters of interest for dust chain formation suggest that further investigation is warranted. PIC-MCC simulations of the plasma at 40 Pa found that the ions thermalized with the neutral gas between ionization fronts, with a large increase in the ion drift velocity associated with the passing of an ionization wave (Matthews 2021). Previous work investigated the effect of the large axial electric field associated with the ionization waves on the stability of the dust chains using numerical simulations of the dust charging and dynamics in the thermalized plasma (Matthews 2021). The results were obtained by increasing the applied electric field, representing different possible averages of the electric field, while the temperature and density of electrons and ions were unchanged. The increased electric field strengths

imposed a drift velocity on top of the thermal motion of the ions obtained from the average plasma conditions between ionization wave peaks, while the use of constant ion and electron temperatures and plasma densities resulted in a constant shielding length for all electric field strengths considered. It was found that the electric field strength corresponding to the ionization wave front was more favorable to dust chain formation than a homogeneous plasma described by the average plasma conditions.

In this work, the behavior of dust and ions in the PK-4 experiment at 60 Pa is investigated in order to match the conditions used in later experimental campaigns. PIC-MCC simulations of the plasma at 60 Pa found that the thermal velocity of ions in the plasma remained about 12% higher than expected if the ions were to thermalize with the neutral gas, and electron and ion temperatures were found to vary continuously (Hartmann 2020). As a result, the current investigation was designed to incorporate the variations in electron and ion temperatures and plasma densities, which allows the effect of changing screening length on the resulting dust chains to be probed. The simulation of the ion and dust dynamics also allows examination of the electric potential near interacting charged dust grains in the case of an anisotropic plasma with ion-neutral collisions. The configuration of the electric potential gives insight into the stability of the dust structures formed in the dynamic plasma context.

4.1.1 PIC Model of PK-4

Previous theoretical results of dust dynamics have been obtained using the assumption that the positive column of the discharge plasma is homogeneous along the axial direction on timescales relevant to the dust dynamics (Sukhinin 2013). Although DC plasma discharges are known to contain self-excited oscillations over a large range of

frequencies and varied plasma conditions (Rohlana 1972), the frame rates used to record the PK-4 ISS glow limit observations to those processes which occur on ms or longer timescales (Pustynnik 2016). Video data collected from the PK-4 experiment appears to be homogeneous, though the presence of fast-moving ionization waves cannot be excluded.

The 2D particle-in-cell with Monte Carlo collisions (PIC-MCC) model (Donko 2021) of local plasma parameters in the PK-4 system used in (Hartmann 2020) revealed the presence of fast-moving ionization waves with a phase velocity in the range of 500 – 1200 m/s. The PIC-MCC model uses the simplified geometry of a 400-mm-long straight discharge tube with an inner diameter of 30 mm, and the cathode and anode placed at each end.

The PIC-MCC simulation was validated against the ground-based experiment BUD-DC. Experimental data collected from the BUD-DC with an exposure time of 40 ms shows that global discharge structure and current dependence are properly captured by the PIC-MCC simulation. However, the PIC-MCC simulation also revealed the presence of fast-moving ionization waves. This finding was confirmed by discharge light emission sequences collected using a high-speed CCD camera with frame rates of 50,000 fps in the PK-4 BU.

4.1.2 Results from PIC Model of PK-4

The main feature revealed by the PIC-MCC model is that conditions within the positive column of the PK-4 discharge lead to large, fast-moving ionization waves occurring on timescales on the order of 10 kHz. The local plasma parameters within the ionization waves vary by as much as an order of magnitude from the time-averaged

values, as shown in Figure 4.2. Further, the frequency of the ionization waves is high enough to prevent the ions from thermalizing with the neutral gas between subsequent peaks of the ionization waves, which results in continuously varying plasma conditions. This is in contrast with the PIC-MCC results obtained at 40 Pa used for the simulation in (Matthews 2021), where the regions between ionization waves were shown to be relatively homogeneous and punctuated only by brief variations in plasma conditions.

The heating of electrons and ions (Figure 4.2a) is accompanied by large variations in the axial electric field (Figure 4.2b), followed by a depletion of both ions and electrons as the ionization wave passes (Figure 4.2c). The time delay between peaks in the different plasma parameters is logical, considering that the charge separation provided by the imbalance of electrons and ions produces the large electric field observed in the ionization wave. This offset between maximum and minimum values in various parameters leads to interesting consequences for the formation of ion wakes and dust structures and will be discussed below.

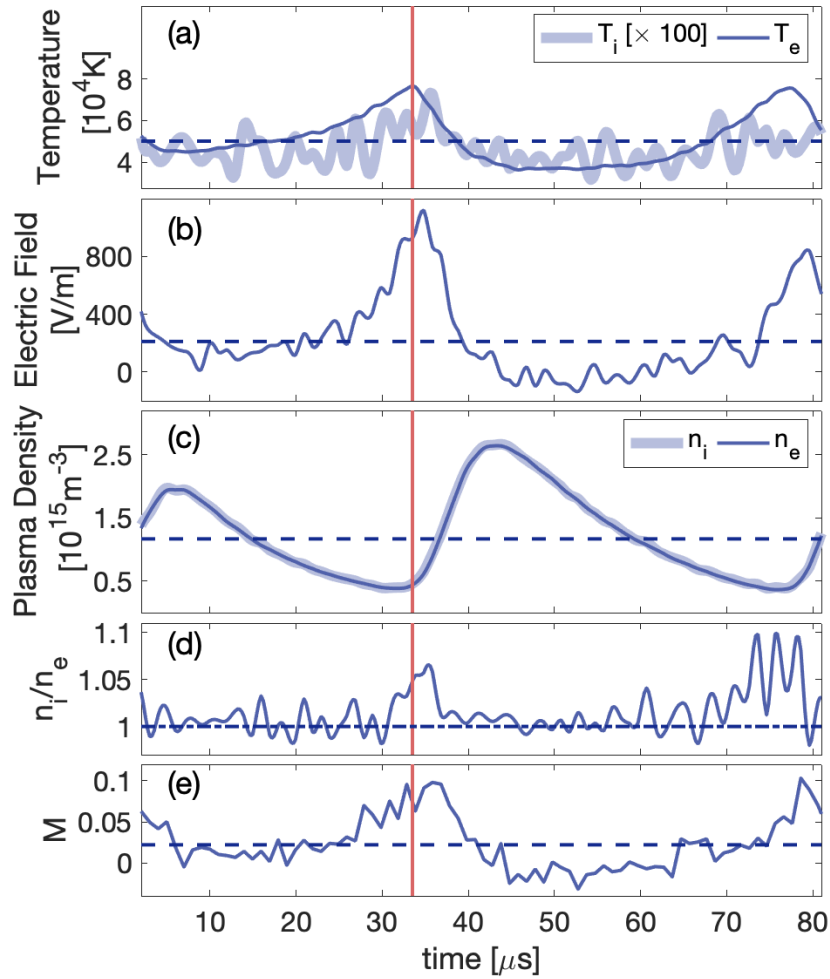


Figure 4.2 Results from the PIC-MCC model illustrating time-varying (a) electron and ion temperatures, T_e and T_i , (b) axial electric field, E_z , (c) electron and ion number densities, n_e and n_i , (d) the ratio of n_i to n_e , and (e) the Mach number, M . The associated time-averaged value of the parameters are indicated by a dashed line corresponding to the values $\langle T_e \rangle = 50107 \text{ K} = 4.32 \text{ eV}$, $\langle E_z \rangle = 211.1 \text{ V/m}$, $\langle n_e \rangle = 1.18 \times 10^{15} \text{ m}^{-3}$, and $\langle M \rangle = 0.022$, respectively. The dot-dashed line in (d) corresponds to $n_i/n_e = 1$. The vertical red line in each panel marks the time of the first peak in temperature. Discharge parameters are neon gas, pressure = 60 Pa, current = 2 mA.

4.1.3 Implications for String Formation

Previous investigations of dust particle chain formation have focused on time-averaged plasma parameters due to the dust particle's large inertia and, therefore, large

response time compared with other plasma species (Arp2012) (with dust typically moving on a millisecond timescale while ions respond on a microsecond timescale). However, as illustrated in Figure 4.2, ionization waves in the plasma lead to large oscillations in the axial electric field, plasma number densities, and the electron and ion temperatures (based on the mean kinetic energies) on a microsecond timescale (Hartmann 2020), which in combination impact the formation of ion wakes in complex plasmas. Since the character of the ion wake changes dramatically, further investigation is needed to determine if this is translated into the dust motion.

Interactions between dust grains and a flowing plasma have been characterized using the Mach number, $M = v_i/c_s$, where v_i is the ion drift velocity and $c_s = \sqrt{k_B T_e/m_i}$ is the ion sound speed (as in Hutchinson 2012). The Mach number (representing the ion flow speed) is shown in Figure 4.2e. Previous investigation of intergrain forces in low-Mach plasma wakes using a particle-in-cell code (Hutchinson 2012) found that wake enhancements are not present when the flow velocity is less than $0.3 c_s$, given $T_e/T_i = 100$ (as is the case in the current investigation, shown in Figure 4.2a). Moreover, it was noted that grain-aligning forces would be negligible and likely would not be responsible for the formation of dust chains at low Mach numbers. As shown in Figure 4.2e, the range of ion flow speeds found are all much less than this threshold value suggesting that, in this case, the dust should be unlikely to form strings. However, results from PK-4 experiments show that the modeled conditions do lead to the formation of long (tens of particles) stable dust strings, suggesting that the established criteria for string formation may be incomplete.

4.2 Methods

4.2.1 Data Selection

The current investigation seeks to isolate the influence that the changing plasma conditions have on the stability of dust chains. In this study we model a small volume within the dust cloud, focusing on the dynamics of a single chain of 20 dust grains with a radial confinement force designed to mimic the effect of surrounding dust chains. The structure of the electric potential surrounding the dust chain, including the contributions from the charged dust grains and the localized concentrations of ions, is examined at different times within the ionization wave. The electron and ion temperatures, which influence dust grain charging and the ion dynamics, reach values within ionization waves that are two to six times the background values (see Figure 4.2a and c). The plasma densities also impact the formation of wake structures around the charged dust grains, which in turn influences both the formation and the stability of the dust chain. The axial electric field (Figure 4.2b) which drives the ion flow leading to wake formation and dust chain stability, reaches peak values in the ionization waves as large as 20 times the value between peaks. Evidently, each of these parameters impact stability and formation of dust chains, and the specific contribution from any individual component could be difficult to isolate. However, the time offset between peak values seen in Figure 4.2 results in the plasma parameters varying in time with respect to each other, which allows for closer observation of the impact each parameter may have.

Specific regions from the time history are selected based on the behavior of the electric field for the present investigation. The plasma conditions within the identified regions of interest are used in the MD simulation to investigate their effect on string

formation, and results are subsequently compared to dust dynamics where the full time-averaged plasma conditions are used. Time-averaged plasma conditions are usually used in simulation or analysis of dust dynamics since the changes in the plasma, which occur on the scale of microseconds, is very short compared to the dust time scale, which is on the order of milliseconds. The different plasma conditions investigated here are: Case (1) *Full Time Average*, where the values of each parameter averaged over a time span (440 μs) covering several ionization waves are considered; Case (2) *Between E_z Peaks*, where only data between the large peaks in the axial electric field are considered, representing a region of minimum ion flow; Case (3) *Rising E_z and Minimum n_i* , where data within the rise of the axial electric field are considered, corresponding to a time when electron and ion number densities are depleted; Case (4) *Full-Width Half-Maximum E_z Peaks*, where the data is averaged over the FWHM of peaks in the axial electric field, representing the maximum ion flow. A representative time interval indicating the data selected for each of the averaging cases is illustrated in Figure 4.3, and the resulting averaged plasma parameters for each case are listed in Table 4.1.

Table 4-1 Plasma parameters used for each of the four averaging cases. Note that $+(-)$ values for E_z and $v_{z,ion}$ indicate parallel (anti-parallel) orientation relative to the tube axis.

Parameter	Full time average	Between E_z peaks	Rising E_z and Min. n_i	FWHM E_z peaks
E_z (V/m)	211.1	-45.2	474.3	814.8
n_{e0} (m^{-3})	1.17×10^{15}	1.58×10^{15}	4.32×10^{14}	6.29×10^{14}
n_{i0} (m^{-3})	1.18×10^{15}	1.59×10^{15}	4.43×10^{14}	6.48×10^{14}
T_e (K)	50107	37549	65330	69767
T_i (K)	466	425	509	565
$v_{z,ion}$ (m/s)	111.5	-29.8	231.7	377.3
Mach (M)	0.022	0.008	0.043	0.070
ω_{pi} (MHz)	10.1	11.7	6.2	7.5

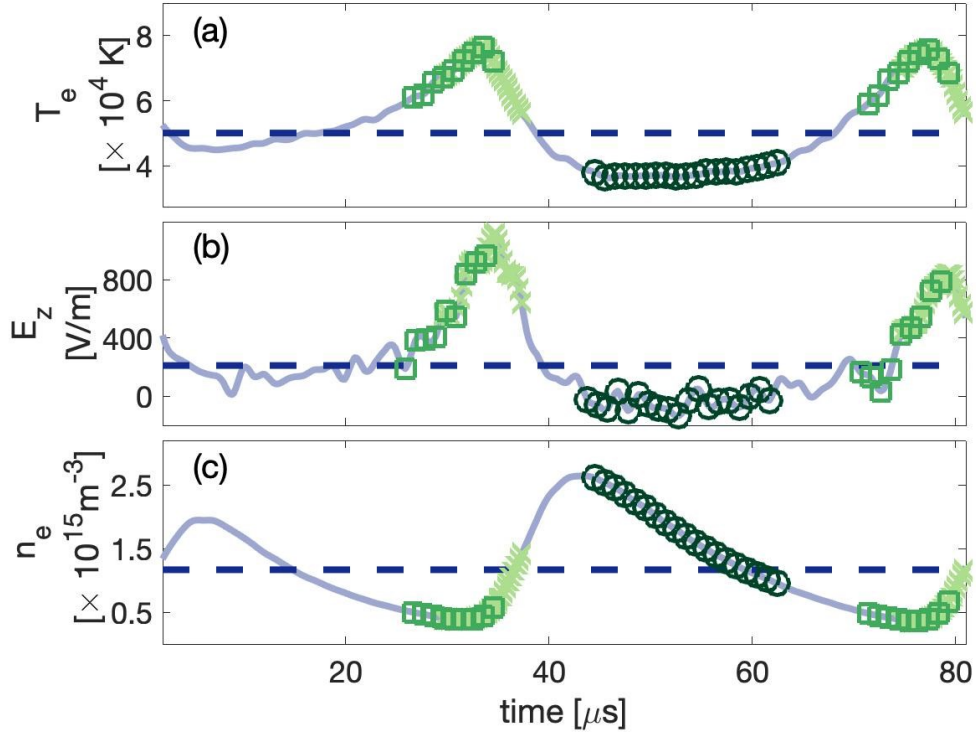


Figure 4.3 Results of the PIC-MCC model showing (as a solid line) the time-varying (a) electron temperature, T_e , (b) axial electric field, E_z , and (c) electron number density, n_e . The data points selected for the various averaging schemes are denoted by: Between E_z Peaks (dark green circles), Rising E_z and Minimum n_i (medium green squares), and FWHM E_z Peaks (light green x's). For comparison, the Full Time Average value of each variable is shown as a dashed horizontal line extending over the full extent in each plot.

4.2.2 Simulating Ion and Dust Motion

The numerical model used to simulate the dust and ion dynamics is DRIAD (Dynamic Response of Ions And Dust). This model is described in detail in Section 3.3 and (Matthews 2020), and here we provide only a brief overview of the components relevant to the current investigation. The dust and ion timesteps were set to $\Delta t_d = 10^{-4}$ s and $\Delta t_i = 10^{-9}$ s, respectively.

The confinement force, \vec{F}_c , simulates the effect of neighboring dust chains outside the simulation region. The confinement is included using the expression

$$\vec{F}_c = \omega_d^2 Q_d \vec{r} \quad (4.1)$$

where the confining strength, ω_d^2 is proportional to

$$\omega_d^2 \propto \frac{C \tilde{Q}}{4\pi\epsilon_0\Delta^2} \left(1 + \frac{\Delta}{\lambda_{De}}\right) \exp\left(-\frac{\Delta}{\lambda_{De}}\right) \quad (4.2)$$

with \tilde{Q} and Δ representing the expected average dust charge and inter-grain separation estimated from results in the PK-4 experiment. The constant C is used to scale the confining force provided by surrounding chains and is based on the expected inter-chain spacing and average dust grain charge. To aid in comparison, the value of ω_d^2 was set to the same value for each of the four cases considered ($3.96 \times 10^6 \text{ V/m}^2$), and the confinement force of Equation 4.1 is ultimately proportional to the charge on a dust grain in the simulation.

In the experiment, the confinement force (\vec{F}_c) would be provided by discrete dust grains present in the neighboring dust chains. Although the influence from individual dust grains does lead to a "ripple" in the resulting potential along the axial direction, simulation of the Yukawa potential resulting from regularly spaced neighboring dust chains revealed maximum deviations from a smooth potential to be on the order of a few hundredths of a mV. The use of a smooth confinement force is therefore considered to be a reasonable approximation for the current investigation.

Note that no axial confinement force is imposed by the simulation other than the polarity switching of the axial electric field. The dust grains are allowed to spread in the z-direction to reach their equilibrium axial interparticle spacing.

4.3 Results

Dust charging and dynamics for 20 dust grains were simulated using the plasma conditions shown in Table 4.1 for each of the four cases. All of the simulations used neon gas with neutral gas pressure $P = 60$ Pa, neutral gas temperature $T = 295$ K, electric field polarity switching frequency of 500 Hz, dust radius $a = 1.69$ μm , and dust mass density corresponding to that of melamine formaldehyde (1.51 g/cm^3). The simulation region is a cylinder of radius 840 μm and length 8050 μm , which provides enough space for the dust grains to reach the expected average interparticle spacing determined from the PK-4 experiment with at least one electron Debye length between the axial ends of the simulation and the outermost dust grain. Dust grains are prevented from leaving the simulation region by a strong confinement force at the simulation boundaries. The dust was initially placed in a region roughly 450 μm in diameter near the center of the simulation region. The dust cloud expanded, and was allowed to evolve for 1.2 seconds, with the dust in each case reaching equilibrium after approximately 1.0 seconds. The dust configuration in each case was found to be stable during the final 200 ms (which covers at least 2 dust plasma periods (τ_d), and the final 100 ms of data was used for the results presented below. The same plasma conditions used in Cases 1-4 of Table 4.1 were also used to model a single stationary dust grain, where only dust grain charging and the motions of ions are considered. The ion density and electric potential near the isolated dust grains are compared with those from the simulation results for the chains

formed by the dynamic dust grains, and relevant results are provided in the following sections. The final average grain charges and interparticle separations are listed in Table 4.2. The magnitude of the grain charge increases with the electron temperatures and the ion flow speed, which also leads to a greater interparticle separation due to the stronger repulsion between grains. However, there is not a linear relationship between the grain charge and interparticle spacing, due to the distribution of ion density and the resulting electric potential, as explained below.

Table 4-2 Size of the cylindrical simulation region expressed in Debye lengths, final average interparticle spacing, and final average dust grain charge for each case.

Parameter	Units	Full time average	Between E_z peaks	Rising E_z and Min. n_i	FWHM E_z peaks
Electron Debye Length, λ_{De}	(μm)	450.3	335.5	838.5	715.8
Ion Debye Length, λ_{Di}	(μm)	43.4	35.7	74.0	64.4
Radius (838.5 μm)	(λ_{De})	1.9	2.5	1.0	1.2
Length (8050 μm)	(λ_{De})	17.9	23.8	9.6	11.3
Interparticle spacing, d	(μm)	345	246	363	370
	(λ_{De})	0.77	0.73	0.43	0.52
	(λ_{Di})	7.9	6.9	4.9	5.7
Charge	(e^-)	2260	2040	2270	2630

4.3.1 Ion Density

The ion densities averaged over the final 0.1 seconds for each of the four cases simulating 20 moving dust grains are shown in Figure 4.4. Note that the plot is zoomed in on the central part of each chain so that the details in the radial direction are visible. The dust grains are shown as grayscale dots, where the color of the dot indicates the magnitude of the distance from the xz-plane (out-of-plane direction), with black indicating dust grains positioned in the xz-plane and white indicating a displacement of

$0.25 \lambda_{De}$, the maximum out-of-plane distance found at equilibrium. The colorbar indicates the ion density normalized to the background ion density far from the dust, n_i/n_{i0} , where values for n_{i0} for each case are given in Table 4.1. From the data shown in Figure 4.4, it is clear that the different cases lead to different ion wake structures, as expected since the extent and location of an ion wake formed in the presence of a charged dust grain depends on the external electric field and resultant ion drift velocities.

In Case 1 (which uses the full time average of plasma parameters, Figure 4.4a) and in Case 2 (which is averaged over the minimal external electric field between ionization wavefronts, Figure 4.4b), the dust forms a somewhat aligned chain with most of the disorder seen in the out-of-plane direction, and the large ion density maxima centered around the dust grains. In Case 3 (averaged over the rise in external electric field, Figure 4.4c), the ion density maxima are less intense and are elongated between the dust grains, and the chain structure shows considerably less displacement out-of-plane. Case 4 (averaged over the FWHM peaks of the external electric field), Figure 4.4d, shows results similar to that of Case 3, with even greater enhancement of ion density between grains. The results shown in Figure 4.4 lead to two broad classifications of the four averaging cases: low ion flow with distinct ion clouds collected around each dust grain (as in Cases 1 and 2), and high ion flow resulting in elongation and merging of the ion clouds (as in Cases 3 and 4).

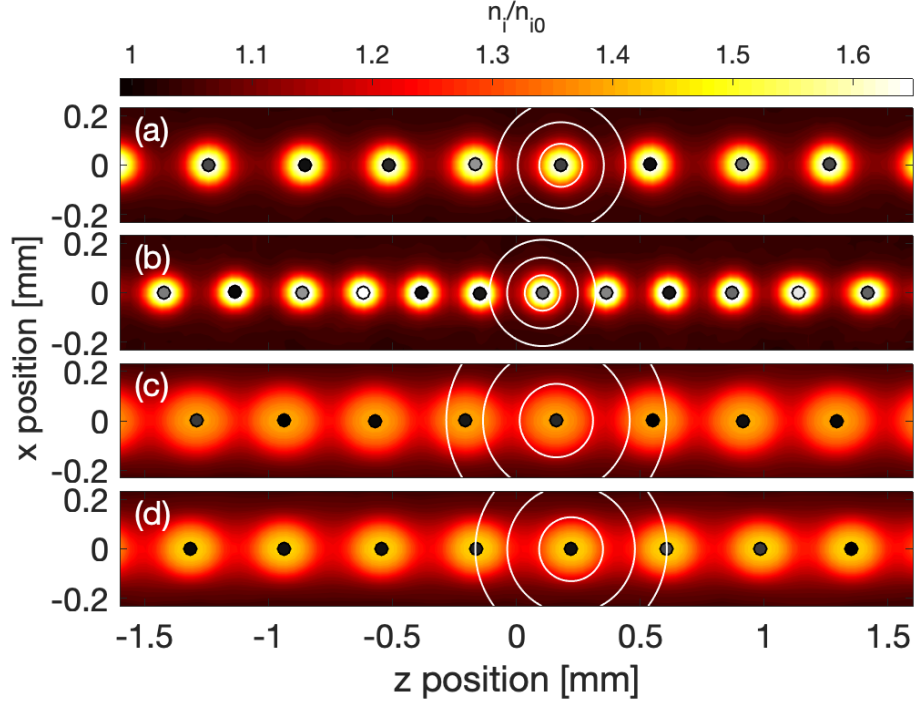


Figure 4.4 Plot of ion density for (a) Case 1: Full Time Average, $n_{i0} = 1.18 \times 10^{15} \text{ m}^{-3}$, (b) Case 2: Between E_z Peaks, $n_{i0} = 1.58 \times 10^{15} \text{ m}^{-3}$, (c) Case 3: Rising E_z and Minimum n_i , $n_{i0} = 4.32 \times 10^{14} \text{ m}^{-3}$, (d) Case 4: FWHM E_z Peaks, $n_{i0} = 6.29 \times 10^{14} \text{ m}^{-3}$. The colorbar corresponds to the ion density normalized to the background ion density far from the dust: n_i/n_{i0} . The shade of the dust grain indicates distance along the y axis (in or out of the page), with black indicating dust grains positioned in the xz-plane and white indicating dust grains $0.25 \lambda_{De}$ from the xz-plane. The three concentric white circles in each plot indicate the distances $2, 4,$ and $6 \lambda_{Di}$ from the location of one of the dust grains.

The various ion and electron temperatures and plasma densities result in a different ion Debye length for each of the four averaging cases examined (the Debye lengths for each case are provided in Table 4.2). Using the white circles (indicating radii of $2, 4,$ and $6 \lambda_{Di}$) in Figure 4.4 as a guide, it is evident that a significant transition has occurred between Cases 1 and 2 and Cases 3 and 4. In Cases 3 and 4, the average interparticle spacing is smaller ($\sim 5\text{-}6 \lambda_{Di}$) than in Cases 1 and 2 ($\sim 7\text{-}8 \lambda_{Di}$). The close proximity of dust grains with respect to the ion Debye length in Cases 3 and 4 are paired

with a smearing-out of the ion density enhancement along the axial direction, while the more isolated dust grains in Cases 1 and 2 correspond to highly localized regions of ion density enhancement.

4.3.2 Electric Potential

The simulation results for the electric potential have a large variation in the background potential along the z-axis, illustrated in Figure 4.5a, as the ions accumulate near the dust chain and normalized ion density is near unity at the ends of the chains. This overall variation in the background potential is expected to be an artifact of the simulation and is eliminated by subtracting a fit to the potential along a line parallel to the z-axis at a radial distance of $9 \lambda_{Di}$. At this distance the axial potential profile is essentially unaffected by the presence of the dust grains (as defined by the normalized ion density being equal to one). The total potential of the ions and dust (indicated by a solid line) and the fit to the background potential (indicated by a dot-dashed line) are shown in Figure 4.5a. The resulting potentials along the z-axis are shown in Figure 4.5b, and the more uniform potential along the z-axis allows for a direct comparison between the four averaging cases considered.

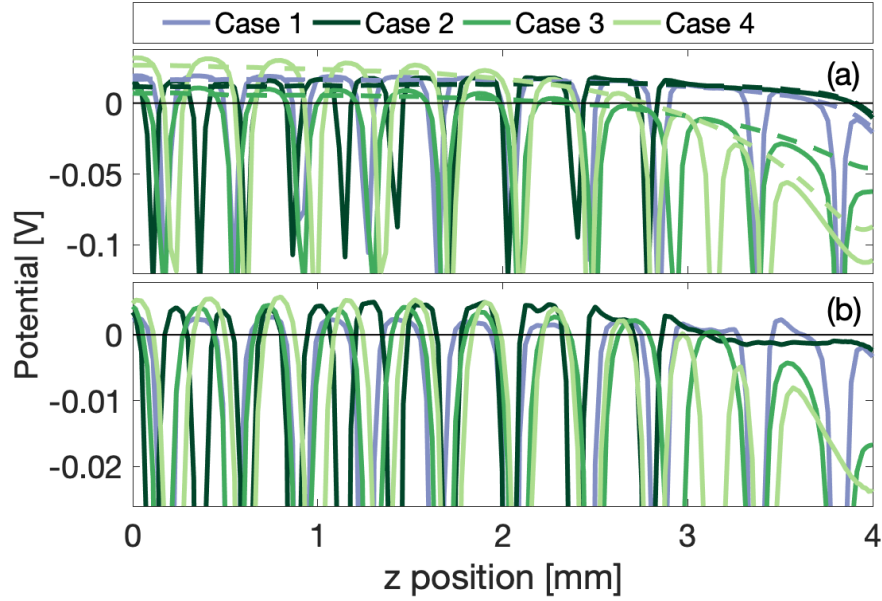


Figure 4.5 Plots showing (a) the total electric potential from the DRIAD simulation along the z -axis (solid lines) and the fit to the axial potential taken at a radial distance of $9 \lambda_{Di}$ from the z -axis (dashed lines), and (b) the resulting total electric potential after subtracting the fit to the axial potential. The horizontal black line indicates the level $V = 0$ in both plots.

The electric potential data, a combination of the negatively charged dust and positive ion wakes, $\Phi = \Phi_{ion} + \Phi_{dust}$, averaged over the final 0.1 seconds are shown in Figure 4.6 for each of the four cases with 20 moving dust grains. As in Figure 4.4, the view is zoomed in on the central portion of the chain to show the detail in the radial direction, and the grayscale color of the dust grains indicates the distance from the xz -plane (out of the page). The relative scale of ion Debye lengths for each case are indicated by the concentric black circles surrounding the central dust grain, with radii corresponding to 2, 4, and $6 \lambda_{Di}$. Each case shows a negative potential well at the dust grain locations, with the extent and depth of the potential well correlated to the magnitude of the charge on the dust grain, which increases with ion flow speed. The maximum positive potential is located between 3-5 λ_{Di} from a dust grain and moves

closer to a grain as the spacing of the dust grains (in ion Debye lengths) decreases. The magnitude of the positive potential between dust grains in Case 3 (Figure 4.6c) is $\sim 75\%$ larger than Case 1 (Figure 4.6a) and $\sim 30\%$ larger than in Case 2 (Figure 4.6b). Case 4 (Figure 4.6d), which corresponds to the largest dust grain charge, has positive potential values $\sim 90\%$ and $\sim 40\%$ larger than Cases 1 and 2, respectively.

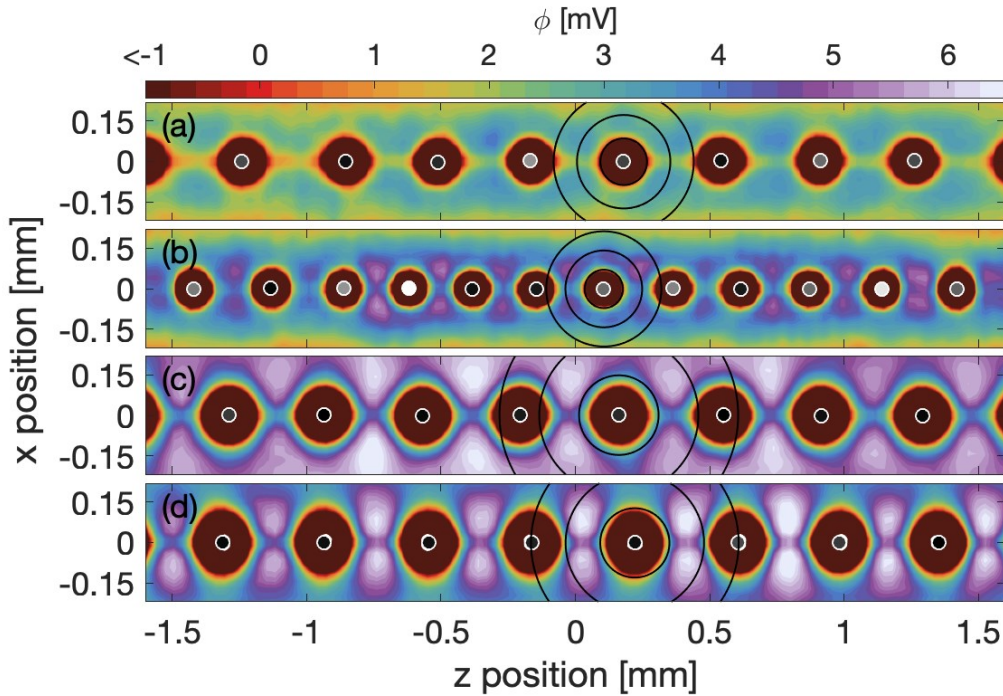


Figure 4.6 Plots showing electric potential for (a) Case 1: Full Time Average, (b) Case 2: Between E_z Peaks, (c) Case 3: Rising E_z and Minimum n_i , (d) Case 4: FWHM E_z Peaks averaging cases. The shade of the dust grain indicates distance from the y -axis (out of the page), with black indicating dust grains positioned on the xz -plane and white indicating dust grains farther from the xz -plane. The three concentric black circles in each plot indicate the distances 2, 4, and 6 λ_{Di} from the location of one of the dust grains.

The large interparticle spacing in Case 1 (Figure 4.6a) relative to the ion Debye length results in minimal overlap of the potential from individual dust grains, allowing the form of the overall potential structure to closely resemble that of an isolated dust grain. In contrast, the close proximity of dust grains relative to the ion Debye lengths in

Case 3 and Case 4 (Figure 4.6c and d, respectively) lead to interesting behavior that differs from a simple superposition of the electric potential from each individual dust grain, which will be discussed further in Section 4.4.

4.3.3 Chain Structure

The final average interparticle spacing in each case are indicated in Table 4.2 measured in μm , λ_{De} , and λ_{Di} . The final interparticle spacing found in Case 1 (representing the time-averaged plasma conditions) was $345 \mu\text{m}$, which is larger than the $230 \mu\text{m}$ average interparticle spacing observed in the experiment. Cases 3 and 4 also have larger interparticle spacing (363 and $370 \mu\text{m}$, respectively) than that observed in the experiment. Case 2 most closely matches the experiment with $d = 246 \mu\text{m}$. It is evident that using the time-averaged plasma conditions results in an over-prediction of the particle charge and a correspondingly large interparticle spacing.

To characterize the order seen in the dust chains in each case, the pair correlation function, $g(r) = (\langle \sum_{i \neq 0} \delta(\vec{r} - \vec{r}_i) \rangle) / \rho$, where $\rho = (\text{number of particles}) / (\text{volume})$, was calculated for each averaging case, shown in Figure 4.7. The pair correlation functions are calculated for the central 12 dust grains using the dust positions over the final 0.1 seconds of simulation time. Order is indicated by well-defined, sharp peaks in the $g(r)$ function at distances corresponding to integer multiples of the average interparticle spacing. As shown in Figure 4.7, the greatest correlation is seen for Cases 3 and 4 (which correspond to smaller interparticle separation measured in Debye lengths). Cases 1 and 2 show the least order in the $g(r)$ function, which correlates with the increased disorder in the out-of-plane direction noted in these cases and larger interparticle separation measured in Debye lengths.

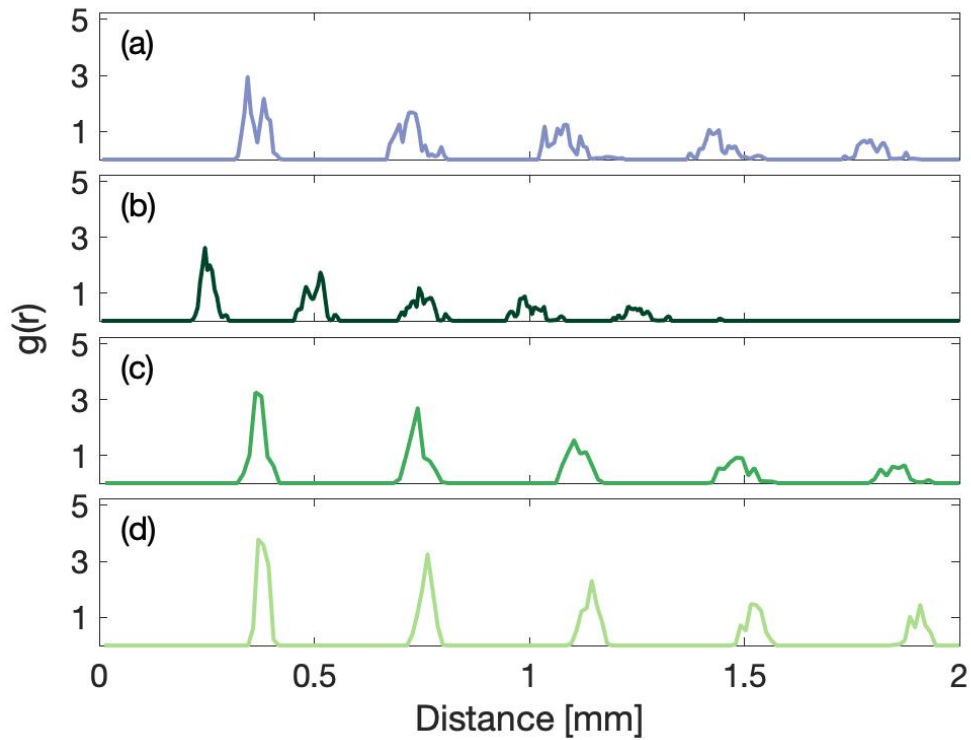


Figure 4.7 Plot of $g(r)$ pair correlation functions for (a) Case 1: Full Time Average, (b) Case 2: Between E_z Peaks, (c) Case 3: Rising E_z and Minimum n_i , (d) Case 4: FWHM E_z Peaks averaging cases.

The pair correlation functions also allow for comparison between the DRIAD simulation results and results obtained from microgravity experiments. Parameters used for the current simulation closely match experimental conditions during Campaign 7 of the PK-4 experiment, which were 70 Pa neon gas, 0.7 mA current, 500 Hz electric field switching frequency, and 1.69 μm radius dust grains. Video data were collected at 71.4 fps, from which 2D images of the dust cloud were analyzed using particle tracking over 90 frames. Three chains comprised of 11 dust grains each were selected from the dust cloud and are highlighted in the top pane of Figure 4.8. These particular chains were selected for analysis because they were similar in length to those analyzed in the

simulation and remained intact over the entire time interval. The pair correlation functions for the three selected chains were calculated and averaged over 30 frames (equivalent to 420 ms), and results are shown in the bottom three panes of Figure 4.8. The color of the pair correlation plots in the bottom three panes of Figure 4.8 correspond to the color used to highlight the dust grains in the image of the dust cloud shown in the top pane.

Qualitatively comparing the results in Figure 4.8 with those in Figure 4.7, the shape of the first five nearest neighbor peaks in the pair correlation function obtained from experimental data most closely match the results in Case 3 (which is averaged over the rise in external electric field) and Case 4 (which is averaged over the FWHM peaks of the external electric field). The plasma conditions in Cases 3 and 4 lead to the greatest order in the dust chains. Although the average interparticle spacing seen in Case 2 is closer to the PK-4 experimental results, the chain formed in Case 2 shows little order compared with the long range order seen in the experimental results.

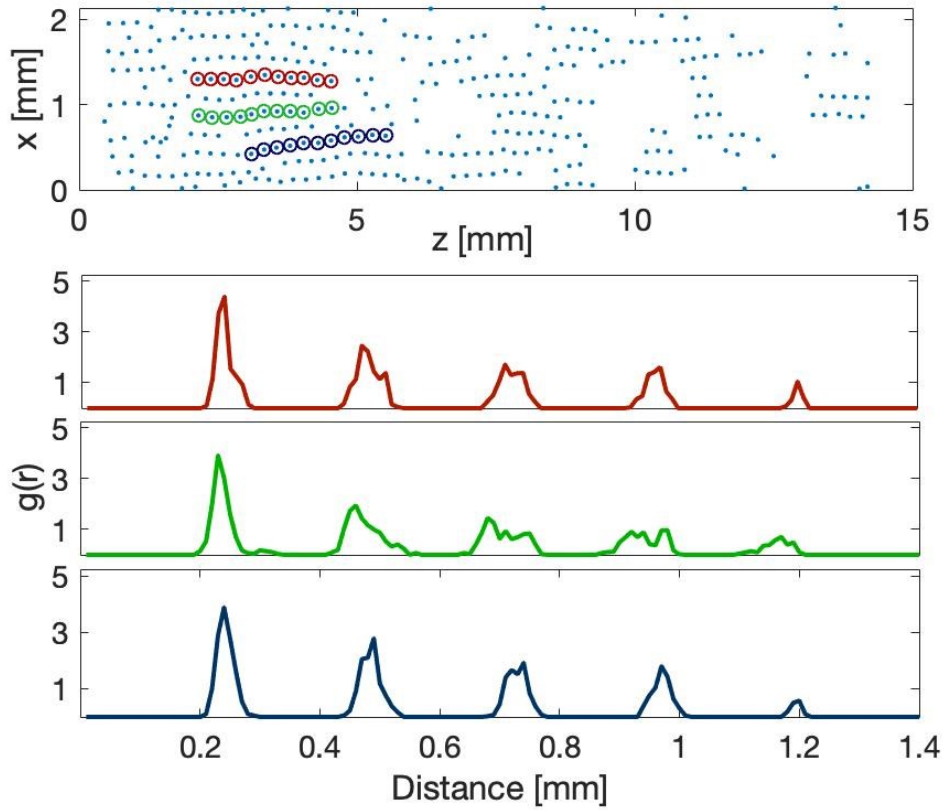


Figure 4.8 Results from analysis of video data obtained during Campaign 7 of the PK-4 ISS experiment showing (top panel) chains chosen for analysis and (bottom 3 panels) the corresponding pair correlation functions for the three selected chains, averaged over 30 frames. Colors used to highlight chain particles in the top panel correspond to the color of the $g(r)$ function in the bottom three panels.

4.4 Discussion

The structure of the ion wake around dust grains has been shown to impact the formation and stability of dust chains in a complex plasma (Ivlev 2008, Matthews 2020). From the $g(r)$ plots it is apparent that Cases 3 and 4 have undergone a transition to a more ordered structure than that found in the results from Cases 1 and 2. The increase in order is correlated with the transition from spherical, isolated ion density clouds surrounding the dust in Cases 1 and 2 to the ion density enhancement becoming more

uniform along the length of the dust chain (parallel to the electric field), and decreased interparticle spacing relative to the ion Debye length.

The increased interparticle spacing in the simulated results (Figure 4.7) when compared with the experimental results (Figure 4.8) is likely due to increased dust charge due to lower dust number density (n_d) in the DRIAD simulation. The visualized portion of the experimental dust cloud used for analysis in Figure 4.8 contains 347 dust particles in a $2.5 \text{ mm} \times 15 \text{ mm}$ window, and is illuminated by a laser sheet with a FWHM extent that varies between 40-220 μm (characterized in Pustyl'nik 2016). This yields a dust number density within the PK-4 ISS experiment on the order of $n_d \approx 10^{10} - 10^{11} \text{ m}^{-3}$, while Langmuir probe measurements in the dust-free discharge (Pustyl'nik 2016) show an electron density on the order of $n_e \approx 4 \times 10^{14} \text{ m}^{-3}$. The charge on dust grains in microgravity conditions at 60 Pa are theoretically estimated in (Antonova 2019) to be $Q_d \approx 2 \times 10^3 e^-$, indicating that as much as 50% of the electrons present in the dust cloud reside on the dust grain surface. It is therefore logical to conclude that the neighboring dust chains present in the experiment lead to a decrease in the electron density within the dust cloud (dependent on the dust number density) that is unaccounted for in the current simulation. If this depletion of the electrons were taken into account, the charge on the dust grains in the simulation conditions would be reduced. However, even with this limitation, the qualitative behavior of the pair correlation function seen in the experiment most closely matches the simulation results in Cases 3 and 4.

Models describing the electric potential surrounding charged particles in a plasma are useful for both planning experiments and analyzing their results, but the assumptions used in the derivation of a given model and its range of applicability must be carefully

considered. The large variation of ion density, electric potential, and the resulting order characterized by $g(r)$ in Cases 2-4 from the full time average plasma conditions in Case 1 suggest that electric potential models which are based on averaged plasma conditions may not fully describe the environment in the PK-4 experiment with the presence of the recently observed ionization waves.

4.4.1 Comparison with Common Electric Potential Equations

The simplest model for the electric potential surrounding a point charge is the *Coulomb potential*

$$\phi(r) = \frac{Q}{4\pi\epsilon_0 r} . \quad (4.3)$$

This form of potential is only dependent on the distance r from the point charge, and therefore fails to capture any effects resulting from local non-neutrality of the charge distribution close to a dust grain. To account for the changes in charge distribution near a dust grain, it is necessary to use the slightly more complex form of electric potential developed by H. Yukawa (Yukawa 1934), which is typically adapted for use in the field of complex plasmas as the *Yukawa potential*

$$\phi(r) = \frac{Q}{4\pi\epsilon_0 r} \exp\left(-\frac{r}{\lambda_D}\right) \quad (4.4)$$

The Yukawa potential (also sometimes referred to as a Debye-Hückel potential) is dependent not only on the distance from the point charge, but also on the temperature and number density of the charged species within the plasma through the term λ_D in the exponent.

While the Yukawa potential does improve upon the Coulomb potential by taking into account the shielding provided by mobile charges in the plasma, it fails to account

for the changes in potential structure that arise from a flowing plasma. A potential model based upon the Bhatnagar-Gross-Krook collision operator has been developed by R.

Kompaneets (Kompaneets 2007), which has the form

$$\phi(\vec{r}) = \frac{Q}{|\vec{r}|^3} F_{BGK}(\theta) + \mathcal{O}\left(\frac{1}{|\vec{r}|^3}\right), \quad (4.5)$$

with

$$F_{BGK}(\theta) = -\sqrt{\frac{8}{\pi}} \frac{u \lambda_{D,T_n}^2}{v_{T_n}} \cos \theta + \left(2 - \frac{\pi}{2}\right) \frac{u^2 \lambda_{D,T_n}^2}{v_{T_n}^2} (1 - 3 \cos^2 \theta) + \mathcal{O}(u^2) \quad (4.6)$$

where $\lambda_{D,T_n} = \sqrt{T_n/(4\pi n_0 e^2)}$, u represents the drift velocity, $v_{T_n} = \sqrt{T_n/m_n}$, and θ represents the angle between \vec{r} and the direction of ion drift. This form has been adapted to account for the symmetric ion wake present in a plasma subjected to an alternating external electric field (as in Ivlev 2010), yielding the form referred to here as the

Multipole Expansion Potential:

$$V(r, \theta) = Q \left[\frac{\exp\left(-\frac{r}{\lambda_{Di}}\right)}{r} - 0.43 \frac{M_T^2 \lambda_{Di}^2}{r^3} (3 \cos^2 \theta - 1) \right], \quad (4.7)$$

where $M_T = u_i/v_{Ti}$ is defined as the "thermal" Mach number, and θ represents the angle between the external electric field driving the ion drift and \vec{r} .

The analytic forms of the electric potential were developed by considering either a single, isolated probe or the interaction between two probes separated by large distances (relative to the ion Debye length). The development of the Multipole Expansion potential relies on the underlying assumption that the thermal Mach number is small ($M_T \ll 1$) and that the distance from the dust grain is much larger than the ion Debye length ($r \gg \lambda_{Di}$), as well as the assumptions inherent in the BGK collision operator, namely that

the collision frequency is velocity independent and only charge exchange collisions are considered.

To compare directly with the analytic potential forms, the plasma conditions used in Cases 1-4 were applied to a single, stationary dust grain located at the origin. The plasma conditions in the four cases are identical to those from Table 4.1, discussed in Sections 4.2.1 and 4.2.2, with the only change being that the dust grain does not move. The ion density data from the single, stationary dust grain simulations are shown in the right column of Figure 4.9. The magnitude of ion density enhancement surrounding the dust grains is largest for Case 2 (Figure 4.9d), as is the case for the simulations containing 20 dust grains. However, asymmetry in the ion density enhancement in Case 3 (Figure 4.9f) and Case 4 (Figure 4.9h) is much less pronounced than in the 20 dust grain simulations (Figure 4.4a and b, respectively). This result suggests that it is the interaction between closely spaced neighboring dust grains (relative to the scale of λ_{Di}) in addition to the plasma conditions which lead to the formation of the elongated ion wake structures found in Cases 3 and 4 (Figure 4.4c and d, respectively), and not the result of the plasma conditions alone. Simulation results for the electric potential of a single stationary dust grain along the axial direction are shown in the left column of Figure 4.9 and compared to the analytic potential forms.

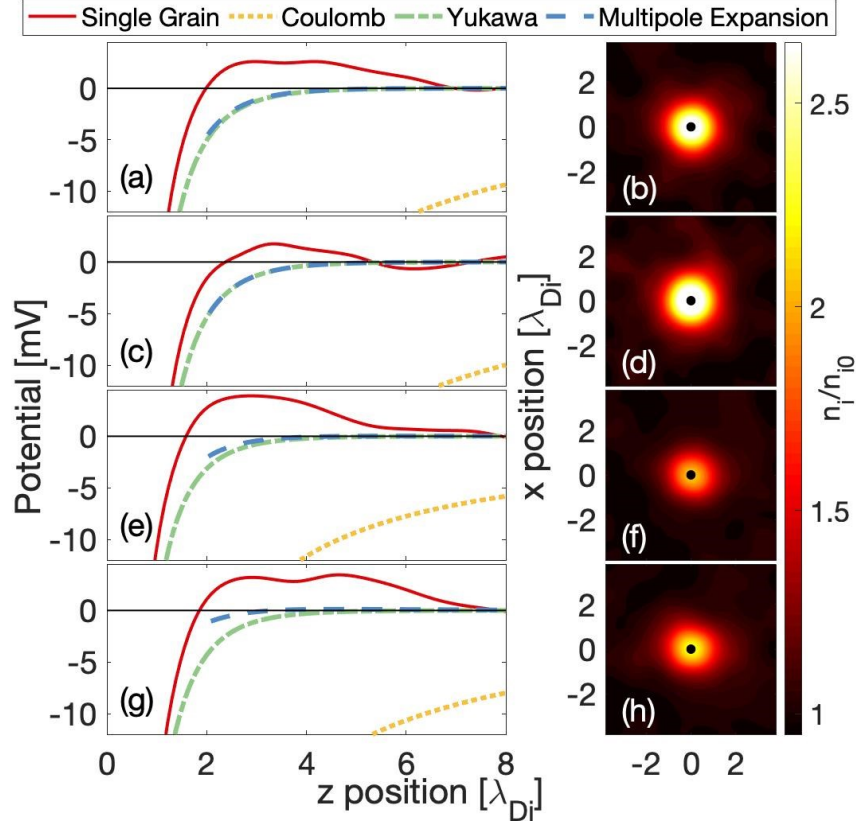


Figure 4.9 Results from simulations of a single dust grain in plasma conditions corresponding to Case 1: Full Time Average (a and b), Case 2: Between E_z Peaks (c and d), Case 3: Rising E_z and Minimum n_i (e and f), and Case 4: FWHM E_z Peaks (g and h). The total electric potential (left column) from simulations (solid red line) is compared with the Coulomb Potential (dotted yellow line), Yukawa Potential (dot-dashed green line), and Multipole Expansion potential (dashed blue line). The ion density (right column) values are normalized to the background ion density (n_{i0}) for each case, which are (b) Case 1: $n_{i0} = 1.18 \times 10^{15} \text{ m}^{-3}$, (d) Case 2: $n_{i0} = 1.58 \times 10^{15} \text{ m}^{-3}$, (f) Case 3: $n_{i0} = 4.32 \times 10^{14} \text{ m}^{-3}$, and (h) Case 4: $n_{i0} = 6.29 \times 10^{14} \text{ m}^{-3}$.

In all four cases it is seen that the Yukawa potential and Multipole Expansion potential agree more closely with the simulation results and with each other than does the Coulomb potential. However, both the Yukawa and Multipole Expansion forms predict a more negative potential than that obtained from the simulation results within a distance $r \lesssim 5 \lambda_{Di}$. Figure 4.9 shows that the difference between the Coulomb potential and the other potentials decrease as λ_{Di} increases, while the difference between the Yukawa

potential and Multipole Expansion potential decreases with decreasing Mach number. To account for the breakdown in the validity of the Multipole Expansion form of the potential as $r \rightarrow 0$, the region $r < 2 \lambda_{Di}$ has been omitted from the line plots in Figure 4.9. The Coulomb potential predicts a larger negative potential than the simulation results due to the lack of an exponential shielding term.

Contour plots showing comparisons between the potential forms and simulation results from each of the four averaging cases with single, stationary dust grains are shown in Figure 4.10. The region corresponding to $2 \lambda_{Di}$ from the dust grains is indicated on plots Figure 4.10m-p by the black circles, which correspond to the minimum radial extent considered valid for the Multipole Expansion potential in Equation 4.9. The asymmetry in the Multipole Expansion potential for Cases 3 and 4 (thought to contribute to the transition to flow-aligned dust chains) (Ivlev 2011) is evident only within the region $r < 2 \lambda_{Di}$, which is excluded by the requirement that distance be much larger than the ion Debye length.

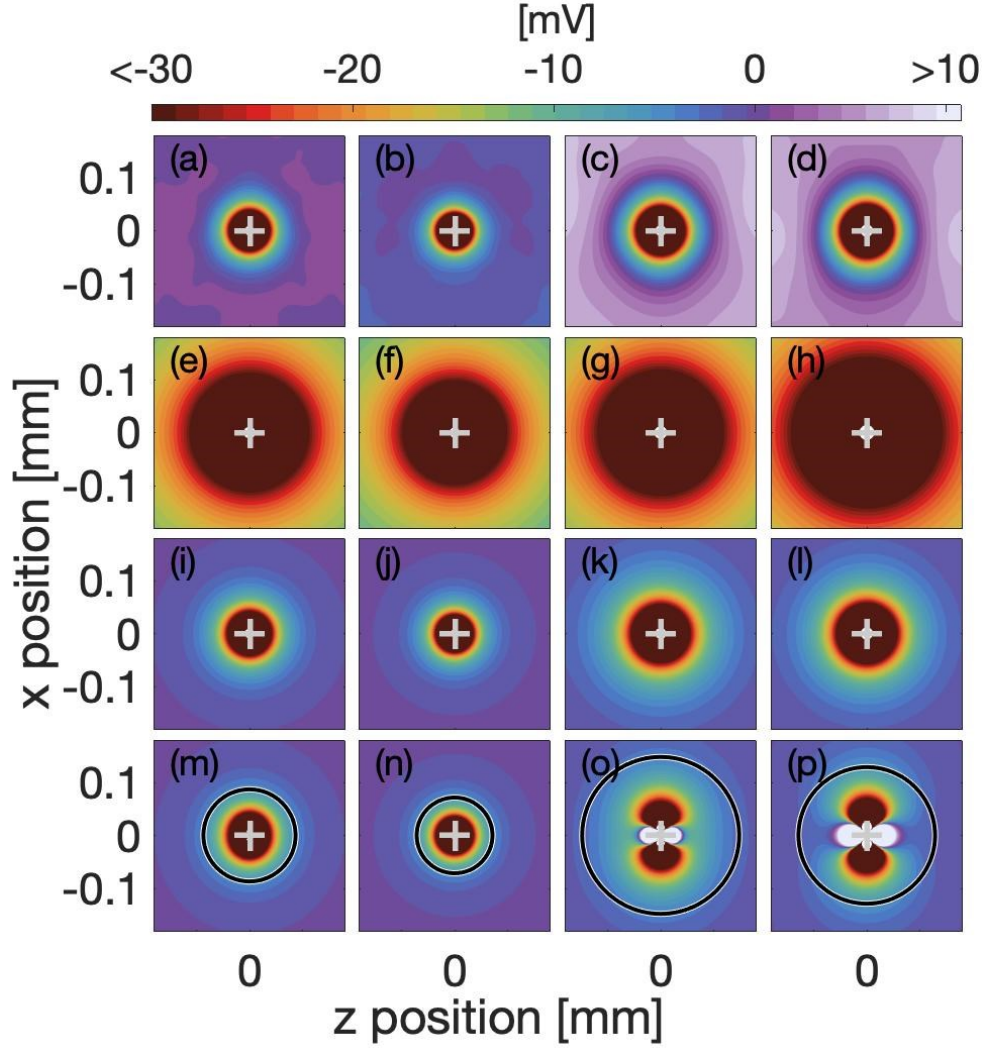


Figure 4.10 Comparison of the simulation results for a single, isolated dust grain (top row: a, b, c, and d) with the Coulomb Potential (second row: e, f, g, and h), Yukawa Potential (third row: i, j, k, and l), and the Multipole Expansion Potential (bottom row: m, n, o, and p). The conditions used for the single grain simulations correspond to the conditions in Table 4.1 for Case 1 (first column), Case 2 (second column), Case 3 (third column), and Case 4 (fourth column). The black circles in the bottom row (m-p) correspond to the radial distance of $2 \lambda_{Di}$ from the dust grain, which is indicated by the gray cross ('+') in each plot.

One may ask how applicable these results are to the case where more than one dust grain is present, and whether the case of multiple dust grains may be adequately represented by a superposition of the potentials of many single dust grains. To address

this question, the results of the simulations with 20 moving dust grains are compared with the Coulomb potential, Yukawa potential, Multipole Expansion potential, and with the single dust grain simulation results superimposed at each of the 20 dust grain locations, shown in Figure 4.11. The Multipole Expansion Potential is shown only in the regions farther than $2 \lambda_{Di}$ from any dust grains, to accommodate the restricted range of validity of this potential form. As expected, the Coulomb potential form shows the greatest deviation from the simulation results for a 20 dust grain chain, with a more negative potential between dust grains for all of the plasma conditions examined. The agreement between the superposition of single dust grain potentials (dotted pink line) and the potential from the 20 dust grain simulation (solid red line) is best for Case 2 (with the lowest axial electric field, ion drift velocity, and dust grain charge). The agreement worsens as the axial electric field, ion drift velocity, and dust grain charge increase, a finding which is consistent with previous studies of the interaction between dust grains with anisotropic ion wakes (Ivlev 2008, Yaroshenko 2021).

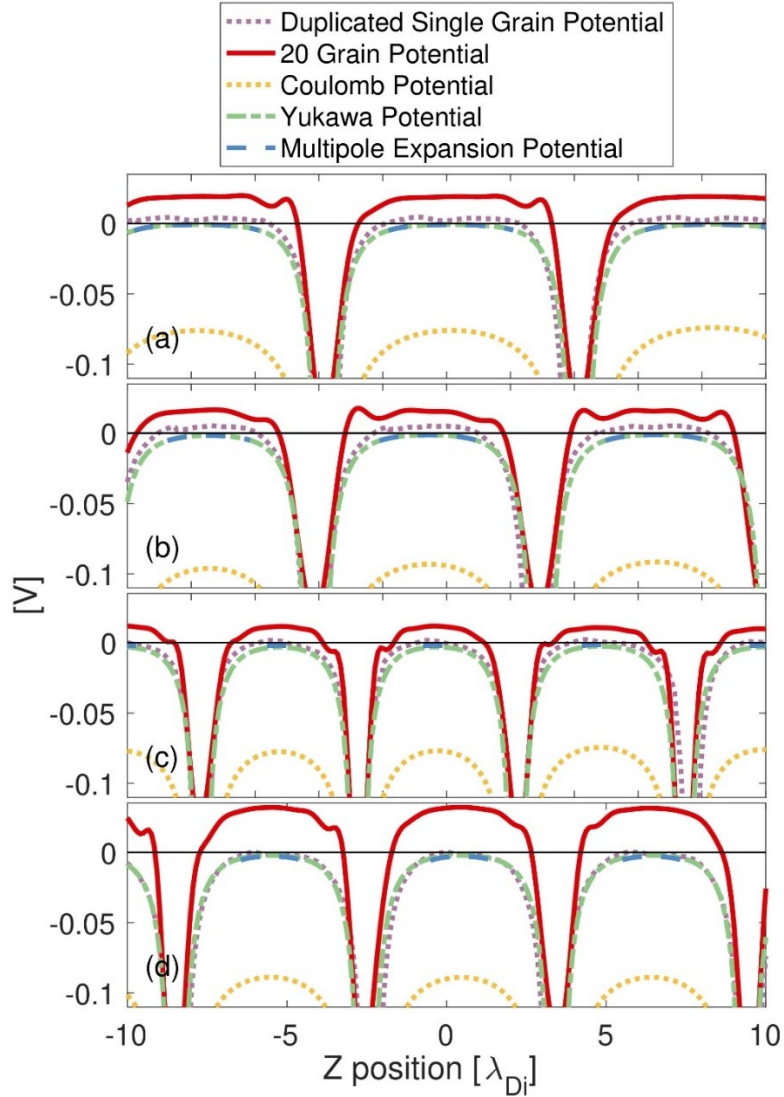


Figure 4.11 Comparison of the superimposed single dust grain simulation results (dotted pink line) with the 20 dust grain simulation results (solid red line), Coulomb Potential (dotted yellow line), Yukawa Potential (dot-dashed green line), and the Multipole Expansion Potential (dashed blue line). Results are shown for (a) Case 1, Full Time Average, (b) Case 2, Between E_z Peaks, (c) Case 3, Rising E_z and Minimum n_i , and (d) Case 4, FWHM E_z Peaks.

Contour plots of the electric potential comparing the results from the simulations of 20 dust grains with the Yukawa and Multipole Potential forms are provided in Figure 4.12. The simulation results in Figure 4.12a-d correspond to the results shown in Figure

4.6, zoomed in on a smaller axial range to allow for closer comparison with the analytic potential forms. The Yukawa potentials corresponding to each of the four averaging cases are shown in Figure 4.12e-h, and contour plots of the Multipole Expansion potential are shown in Figure 4.12i-l. The region corresponding to $2 \lambda_{Di}$ from the dust grains is indicated on plots Figure 4.12i-l by the black circles, which correspond to the minimum radial extent considered valid for the Multipole Expansion potential in Equation 4.7.

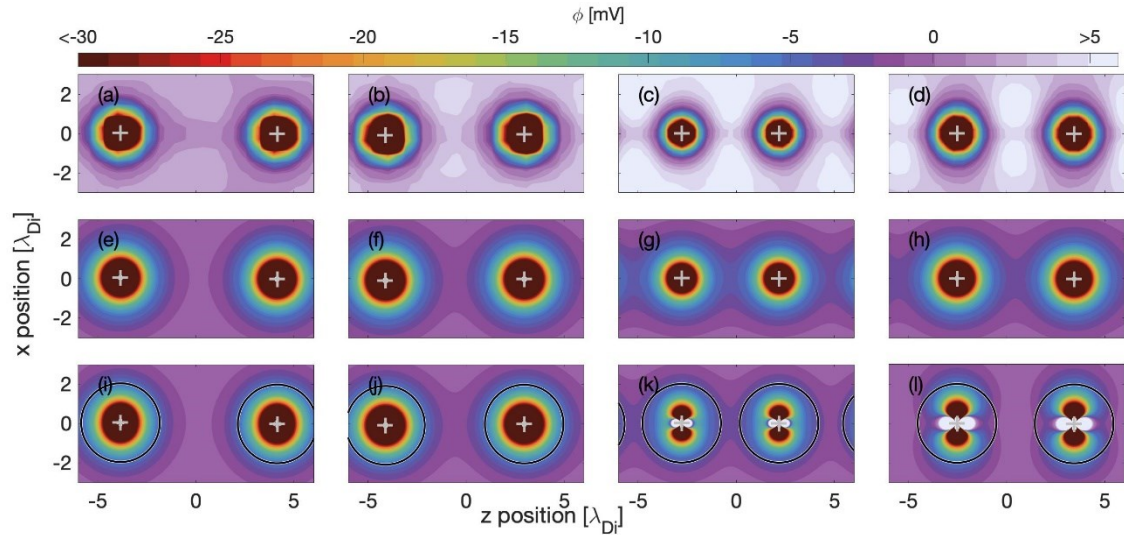


Figure 4.12 Figure 4.12. Comparison of electric potential from the simulation (top row, a-d) with the analytic potential forms discussed in Section 4.4.1: the Yukawa Potential is shown in the middle row (e-h), and the Multipole Expansion Potential is shown in the bottom row (i-l). The first column on the left (a, e, and i) shows Case 1 (Full Time Average), the second column (b,f, and j) shows Case 2 (Between E_z Peaks), the third column (c, g, and k) shows Case 3 (Rising E_z and Minimum n_i), and the fourth column (d, h, and l) shows Case 4 (FWHM E_z Peaks). Positions of dust grains are marked with a gray cross (+). Black circles in i-l indicate the radius $2 \lambda_{Di}$ from dust grains.

Careful consideration of the results shown in Figure 4.12 makes it evident that the simulation results are not adequately described by the expressions for dust potential using the Yukawa potential or the Multipole Expansion potential given by Equation 4.7. The

comparison between a 3D PIC simulation and the numerical solution of linearized electrostatic potential carried out in (Ludwig 2012) showed that the charge and potential of the downstream grains can be significantly modified by wake effects in a system of several grains, and the wake pattern can show significant deviation from the potential determined from a linear combination of a wake behind a single grain in subsonic flows. These results are supported by the results presented in Figure 4.11, where it is seen that the linear superposition of single dust grain potentials deviates from the simulation of 20 dust grains for ion sound speeds as low as $0.07 M$ (corresponding to Case 4). These findings also correlate with the comparison shown in Figure 4.12, where it is seen that the potential for the dust strings is not well represented by the models developed for isolated grains.

Many stable self-organized dust structures have been observed in ground-based and microgravity plasma environments, but the available models for electric potential have been found to be not well suited for describing the interactions between large numbers of dust grains. Further description of the electric potential structure is needed, given that the dynamics of charged species within a complex plasma and the form of electric potential are inextricably linked, and will be the focus of a forthcoming study.

4.4.2 Dust Grain Charging

The time a dust grain takes to reach equilibrium charge ($\sim 60\text{-}100 \mu\text{s}$) is longer than the time it takes for an ionization wave to pass ($\sim 50 \mu\text{s}$ peak-to-peak), meaning that the actual dust charges will differ from those shown in Table 4.2. As a simple model for the dust grain charging and de-charging during the various phases in ionization waves, we may consider the dust grain to be a spherical capacitor and evaluate the charging and

de-charging time as a dust grain transitions between the plasma conditions in Cases 2, 3, and 4. Simulation results show that time to reach the new equilibrium charge after transitioning between cases was found to be 60-100 μs , with the longest time taken when transitioning from the conditions in Case 4 to the conditions in Case 2 (which has the longest ion plasma period, shown in Table 4.1).

As a rough approximation for the expected equilibrium charge for dust grains exposed to evolving plasma conditions due to ionization waves, a simple capacitor model was used to calculate the charge on a dust grain as a function of time as the grain charged or discharged in the plasma conditions associated with Cases 2-4. This model was used to generate the piece-wise charging curve shown in Figure 4.13. The final average charges in Cases 2-4 are shown as dot-dashed horizontal lines in shades of green, and the average equilibrium charge reached by the capacitor model in evolving conditions is shown as a dot-dashed horizontal pink line. The piece-wise charging curve is shown by the thick solid line, with the color of the line segments corresponding to charging following the transition from Case 4 to Case 2 (dark purple), the transition from Case 2 to Case 3 (dark pink), and the transition from Case 3 to Case 4 (light pink). Over 40 μs (the approximate peak-to-peak time for the ionization waves), the charge fluctuates on the order of $\sim 200 e^-$, with a time-averaged charge of $2150 e^-$, which is lower than the charge predicted by Case 1. This lower charge would result in smaller interparticle spacing, more closely matching that observed in the experimental data (Figure 4.8). However, it is important to note that this simple model is based upon constant conditions present within snapshots in time of dynamically varying plasma conditions, and as such may vary from the equilibrium charge found in an experimental environment. In light of

the impact fluctuating charges will have on the formation and stability of dust structure, future investigations utilizing time varying plasma parameters are needed to further quantify the impact ionization waves have on dust dynamics in the PK-4 environment.

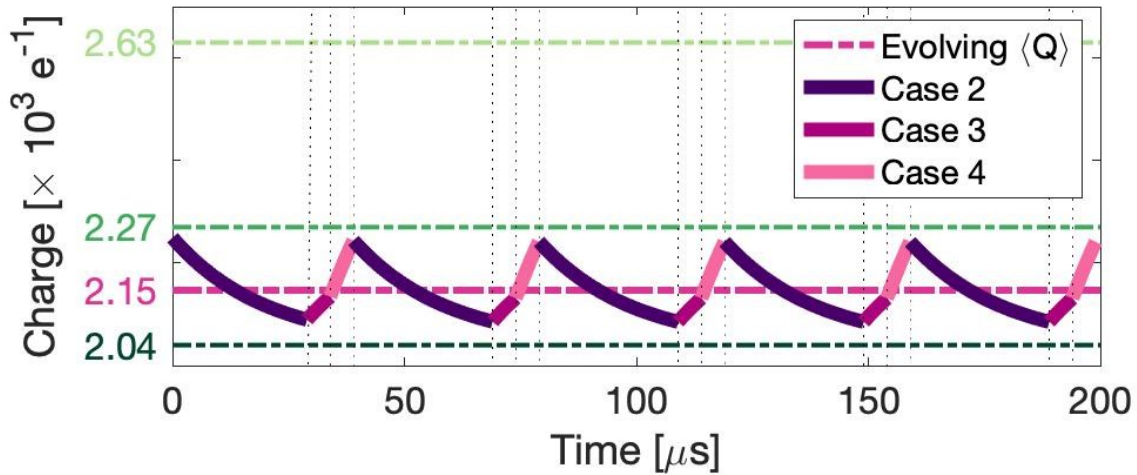


Figure 4.13 Plot indicating the charge over time on a dust grain undergoing transitions between Cases 2, 3, and 4. The color of the solid line segments in the charging curve indicates the particular transition, with dark purple corresponding to charging following the transition from Case 4 to Case 2, dark pink corresponding to charging following the transition from Case 2 to Case 3, and light pink corresponding to charging following the transition from Case 3 to Case 4. The vertical dotted black lines indicate the transitions, and horizontal dot-dashed lines indicate the final equilibrium charge in dark green for Case 2 ($2040 e^-$), medium green for Case 3 ($2270 e^-$), light green for Case 4 ($2630 e^-$), and pink for the average charge resulting from transitions between Cases 2-4 ($2150 e^-$).

4.5 Conclusion

Varying conditions within the ionization waves present in the PIC-MCC simulation of conditions within the PK-4 ISS (Hartmann 2020) have a significant impact on the formation of dust chains. The effect of fast-moving ionization waves on the formation of ordered dust particle chains and the resulting electric potential structure has been investigated by first identifying regions of interest within the time evolving plasma conditions (shown in Figure 4.3), labeled as the four cases: (1) *Full Time Average*, where

the values of each parameter are averaged over a time span (440 μs) encompassing several complete ionization waves; (2) *Between E_z Peaks*, where only the data in the interval between the large peaks in the axial electric field are considered, representing a region of minimum ion flow and a steady, constant plasma column; (3) *Rising E_z and Minimum n_i* , where the data within the rise of the axial electric field are considered, corresponding to an interval where electron and ion number densities are depleted; and (4) *Full-Width Half-Maximum E_z Peaks*, where the data is averaged over the FWHM of peaks in the axial electric field, representing the maximum ion flow. The specific plasma parameters identified for each case (listed in Table 4.1) were then modeled using DRIAD, a molecular dynamics simulation capable of resolving dust and ion motions on each of their respective timescales, and results for the ion density (Figure 4.4), electric potential (Figure 4.6), and analysis of the final dust structure (Figure 4.7) have been presented for each of the four cases.

Although considered separately in this investigation, it is important to recall that the conditions of Cases 2, 3, and 4 represent different features within the ionization waves, with each case describing an interval of 10-20 μs within a full ionization wave (with peak-to-peak interval of $\sim 40 \mu\text{s}$), while the relevant dust dynamics occur on a timescale of 100 μs . As such, in the time-evolving experimental system, the decreased ion wake structure and diminished order for Case 2 (Figure 4.4b and Figure 4.7b) is immediately followed by the enhanced wake and order found in Case 3 (Figure 4.4c and Figure 4.7c). As the ionization wave moves past a dust chain, conditions between ionization wave peaks (minimum ion velocities and maximum ion density) lead to an increase in ion current and subsequent decrease in the magnitude of charge on the dust

grains, which allows dust grains to move closer together. As the wave continues past the dust grains (with increased ion velocities and minimum ion density), the increased ion focusing leads to an enlarged region of positive potential between dust grains is the largest. Even though the average charge on dust grains increases during this phase, the large positive potential in the strongly focused ion wake allows for smaller interparticle spacing relative to the shielding length, as well as increasing the grain alignment. As shown in Figure 4.7c-d, this leads to the largest order in the resulting dust chain. The lower particle charge found using the capacitor charging model (Figure 4.13) allows for the smaller interparticle spacing, which more closely matches the experiment, while the enhanced ion wakes during the ionization waves contributes to the stability of the chain.

The balance between the various parameters is not captured by the full time average (Case 1), and as such, it is likely that the full time average does not provide an accurate representation of the conditions to be used to model dust dynamics. Additionally, further work is needed in modeling the effect of ions through a modification of the potential of charged dust grains, as the current analytic models do not match the ion behavior.

CHAPTER FIVE

Interacting Dust Grains in Complex Plasmas: Ion wake formation and electric potential

This chapter was submitted as []: Katrina Vermillion, Rahul Banka, Bryant Wyatt, Lorin Matthews, Truell Hyde, 2022 “Interacting Dust Grains in Complex Plasmas: Ion wake formation and electric potential,” ArXiv.

5.1 Introduction

Under laboratory conditions, micrometer-sized particles (referred to as dust) will typically acquire a negative charge due to the high mobility of electrons, with the final charge determined from the balance of electron and ion currents to the dust grain surface. The negatively charged dust grains influence the motion of other charged species by repelling electrons and attracting ions, forming a region of electron depletion near the dust grain surface and, in a flowing plasma, accumulating positively charged ions in a region downstream from the dust grain. This region of excess positive charge due to the accumulation of deflected ions (called the ion wake) can interact with other dust grains, and has been suggested as one possible mechanism for the self-organization of dust grains into experimentally observed complex structures (Vladimirov 1995, Melandsø 1996, Melzer 1999, Shukla 2009, Miloch 2010).

Complex plasmas are proving to be a valuable analogue for microscopic systems due to the easily visible dust grains. The self-organization of these dust grains into single chains (Kong 2011), zigzags (Hyde 2013), twisted helices, and other complex structures can provide insight into the ordering of materials at the molecular scale. However, a complete description of the mechanism(s) responsible for the self-organization of these

dust structures requires an understanding of the electric potential, which is dependent upon the local plasma densities, the location and charge of the dust grains, and any externally imposed confinement. Unfortunately, the precise location and magnitude of the charge contained in the ion wake is challenging to predict even for isolated charged dust grains, which leaves our present understanding of the self-organization of dust grains incomplete.

Previous studies have noted apparent differences between conventional descriptions of the electric potential (which were developed for isolated charged dust grains or stationary plasma) and simulation results both for multiple dust grains and close to the surface of a dust grain in flowing plasma (Lampe 2000, Ikkurthi 2008, Zobnin 2008, Ikkurthi 2010, Piel 2017, Matthews 2020, Vermillion 2022). The electric potential surrounding a charged dust grain in a flowing plasma is inherently asymmetric due to the formation of the positive ion wake downstream from the dust grain (Vladimirov 2003, Lampe 2000), and the introduction of additional dust grains further complicates the structure of the electric potential. The goal of the present study is to quantify the variability of the electric potential near multiple charged dust grains in a flowing plasma by comparing simulation results for a single stationary dust grain with those obtained from simulations of two and three stationary dust grains positioned at varying interparticle separation distances and angular orientations relative to the ion flow direction. The paper is organized as follows: a brief review of ion wakes is presented in Section 5.2, an overview of the simulation and input parameters are provided in Section 5.3, results from the simulations are presented in Section 5.4, a discussion of the electric potential fitting is provided in Section 5.5, and Section 5.6 contains concluding remarks.

5.2 Background

Numerous experiments (Chu 1994, Arp 2005, Melzer 2006, Kong 2011, Sheridan 2012, Hyde 2013, Lisin 2020) and simulations (Lampe 2000, Ikkurthi 2008, Zobnin 2008, Ikkurthi 2010, Miloch 2012) have been performed to investigate the plasma conditions under which dust grains self-organize, and identify the mechanism(s) responsible for the transition from one configuration of dust grains to another. Among these studies, positively charged ion wakes have been considered as a probable mechanism for self-organization of dust structures observed under certain plasma conditions. The interaction between a positive ion wake produced below one dust and other negatively charged dust grains reduces the effective repelling force between negatively charged dust grains. A simplified description of this interaction treats the ion wake as a single charged particle (or point charge) located at the center-of-charge in the ion wake, and may represent a suitable model under conditions where the point charge can be considered to have a constant charge and position relative to the dust grains (Melzer 1996, Zhdanov 2009, Couédel 2011, Melzer 2014, Matthews 2020).

The accumulation of excess positive charge in the ion wake below a dust grain also represents a significant alteration to the local electric potential near a charged dust grain (Lampe 2000). Dust grains separated by more than two electron Debye lengths perpendicular to the ion flow direction have been found to charge to approximately the same level as a single dust grain, and tend to form ion wakes which are positioned directly downstream from the grains. However, when dust grains are positioned closer together (i.e., at a fraction of the electron Debye length (Vladimirov 2003)), the ion

wakes tend to merge into a single, larger ion wake with a larger magnitude of positive charge accumulation. As a result, the simplified point charge model for a single, isolated dust grain fails to represent the spatial ion density variations near multiple closely spaced dust grains, and an accurate calculation of the electric potential in this case requires higher resolution of the local ion density (Block 2015, Miloch 2012, Ikkurthi 2010, Matthews 2020). An additional complicating factor is that the commonly-used shielded Coulomb, or Yukawa, potential is known to break down close to the surface of a dust grain and in regions where the anisotropy of the plasma density leads to variable shielding lengths (Lampe 2000). Other forms of the electric potential have been developed based upon particular velocity distributions and ion collisionality (as in Kompaneets 2007b), but were developed for distances far from a dust grain and do not provide insight to interactions between dust grains with the small interparticle spacing typically found in chains, zigzags, and helices (Hyde 2013, Kamimura 2012).

5.3 Methods

The electric potential in a complex plasma is directly related to the distributions of charged species, and a complete description of the minimum energy configuration of any collection of dust grains necessarily requires an adequate description of the electric potential. Therefore, the focus of the present work is to simulate the motions of ions in the vicinity of closely-spaced charged dust grains, and evaluate how the equilibrium distribution of ions is affected by varying the interparticle separation of dust grains and their orientation relative to the axial electric field. The specific influence of the dust grain orientation on the equilibrium ion distribution is isolated by simulating one, two, and three dust grains at different locations using the DRIAD molecular dynamics

simulation while keeping the background plasma conditions constant for all cases.

Relevant details about DRIAD are provided in Section 5.3.1, and a description of the simulation parameters is provided in Section 5.3.2.

5.3.1 Simulation Description

Each iteration of the DRIAD simulation modeled stationary spherical dust with radii of 4.445 μm in an argon plasma. The neutral gas pressure $P = 20.8$ Pa, electron temperature $T_e = 30,000$ K (2.59 eV), ion temperature $T_i = 369$ K (0.032 eV), electron number density $n_e = 1 \times 10^{15} \text{ m}^{-3}$, ion number density $n_i = 3 \times 10^{15} \text{ m}^{-3}$, and axial electric field $\vec{E} = -4,000 \text{ V/m } \hat{z}$ were selected to approximate the experimental conditions where self-organization of dust grains has been observed in the sheath above the electrode of a GEC rf reference cell (Hyde 2013, Kong 2011, Kong 2014). The simulation parameters yield electron and ion Debye lengths of $\lambda_{De} = 377.9 \mu\text{m}$ and $\lambda_{Di} = 24.2 \mu\text{m}$, where the Debye length is calculated using $\lambda_{Dj} = \sqrt{\epsilon_0 k_B T_j / (n_j e^2)}$ substituting $j = e$ for electrons or $j = i$ for ions, with the physical constants $\epsilon_0 = 8.854 \times 10^{-12} \text{ F/m}$, $k_B = 1.3807 \times 10^{-23} \text{ J/K}$, and $e = 1.6022 \times 10^{-19} \text{ C}$. The sound speed Mach number determined from the simulation results is 0.623 with a standard deviation of 0.002, where $\text{Mach} = \bar{v}_i / c_s$ and the sound speed $c_s = \sqrt{k_B T_e / m_i}$. Each simulation covered an elapsed time of 0.2 ms, approximately 2,300 ion plasma periods (τ_{pi}), where $\tau_{pi} = 1 / \omega_{pi}$, and $\omega_{pi} = \sqrt{n_i e^2 / (\epsilon_0 m_i)}$ = $1.15 \times 10^7 \text{ Hz}$. The simulation parameters are also provided in Table 5.1 for reference.

Table 5-1 Plasma parameters used for input in the DRIAD simulation.

P [Pa]	T_g [K]	T_e [K]	T_i [K]	n_e [m ⁻³]	n_i [m ⁻³]	\vec{E} [V/m]	r_d [μm]	m_i [kg]
20.8	300	30,000	369	1×10^{15}	3×10^{15}	$-4,000 \hat{z}$	4.445	6.634×10^{-26}

In order to evaluate the electric potential in the vicinity of charged dust grains, more than 400 DRIAD simulations were performed using the same background plasma conditions with one, two and three dust grains separated by 1-16 λ_{Di} (24-379 μm) and orientated at angles relative to the axial electric field ranging from parallel (0°) to perpendicular (90°). The simulation with a single dust grain was performed with one dust grain located at the origin. Simulations with two dust grains were performed by placing the two dust grains at regular intervals along the directions perpendicular (\hat{x}) and parallel (\hat{z}) to the axial electric field, with interparticle separations ranging from 0-14 λ_{Di} in both directions. Simulations with three dust grains were performed by arranging two dust grains symmetrically about the z-axis of the simulation region and placing a third dust grain centered on the z-axis below them. The upper two dust grains were separated by 1-14 λ_{Di} along the \hat{x} -direction, and for each interparticle separation of the upper two grains, the third dust grain was positioned 0.5-14 λ_{Di} below their midpoint along the \hat{z} -direction. A representation of the various dust positions is shown in Figure 5.1 for cases with (a) two and (b) three dust grains. The interparticle separation distance, d , and angle of orientation, θ , relative to the axial electric field, \vec{E}_z , are shown for a representative case in both panels. In panel (a) the position of the upper right dust grain in each simulation is indicated by the gray filled circle, and relative positions for the lower left dust grain are indicated by the open circles (size of circles in the figure are not representative of the size

of dust grains). The positions of the upper two dust grains used in the three dust grain simulations are identified in Figure 5.1b by matching colors, while the positions for the third dust grain are indicated by the black outlined circles.

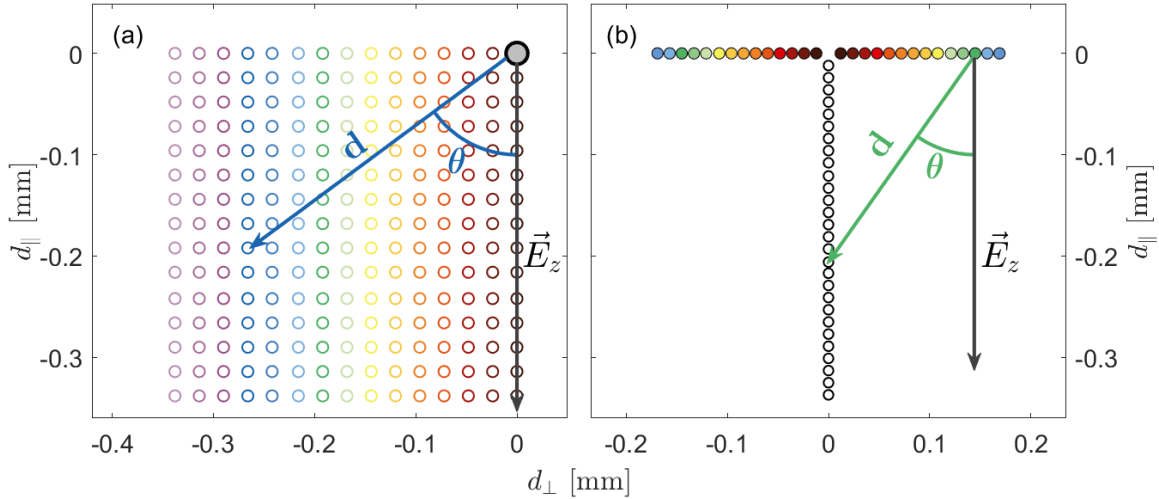


Figure 5.1 An illustration indicating the positions of stationary dust grains in the simulations with (a) two and (b) three dust grains. The separation distance, d , and angle of orientation, θ , relative to the axial electric field direction (\vec{E}_z) are indicated for a representative case in both panels. In panel (a) the relative position of the upper right dust grain in each simulation is indicated by the gray filled circle, and relative positions for the lower left dust grain are indicated by the open circles (size of circles \neq size of dust grains). Cases with three dust grains, (b), each use a pair of upper dust grains (illustrated as circles with the same color) with the third dust grain located at the position indicated by the black outlined circles. The axial electric field points from the top to bottom in both panels, indicated by the gray arrow.

Key characteristics of the ion wakes include the location of the center-of-charge in the ion wake, the amount of charge contained in the ion wake, and the point of maximum ion density within the ion wake. The DRIAD simulation provides ion density values at evenly spaced grid points along the xz -plane (the central axis of the simulation cylinder) at time intervals specified by user input. For the present simulations, the time-averaged ion density is output by DRIAD every 0.001 ms, and results for the 0.2 ms simulation are averaged and interpolated to a grid with uniform 1 μm spacing in the xz -

plane. A visual representation of the 2D grid is provided in Figure 5.2, where the contour colors represent the normalized ion density (each $0.2 n_i/n_{i0}$ division is marked by a solid contour line), the gray circles represent dust grain locations (not indicative of dust grain size), and the light gray grid lines depict the location of every 10th grid division in the x and z directions. The maximum ion density value in each wake is indicated by a green diamond, and the calculated 3D center-of-charge in each wake is represented by the white star.

The 2D ion density data is extended to 3D by first identifying the grid points within the ion wake (defined to be all grid points where the ion density is larger than the background ion density by a set threshold value of $n_i \geq 1.4 n_{i0}$, the outermost contour line in Figure 5.2). Next, the volume of an elliptical 3D ring is calculated at each grid point, (j, k) , using the radial distance of the grid point from the location of the ion density maximum in the wake, $r_{j,k}$, with the width and height of the ring equal the axial and radial grid spacing, $\Delta x = \Delta z = 1 \mu\text{m}$,

$$\frac{V_{\text{ring},j,k}}{2} = \beta \pi \Delta x \Delta z [r_{j,k} + \Delta x]. \quad (5.1)$$

The volume of the ring calculated at each grid point is divided by two (representing either the left or right half of the ring) to allow for asymmetry in the shape of the wake along the x -direction. The extent of the wake in the direction perpendicular to the xz -plane is scaled using $\beta = R_{\text{single}}/R_{\text{wake}}$ to account for the azimuthal asymmetry in the wake arising from the simulated dust grains being displaced only in the xz -plane, where R_{single} is the maximum width of the wake of a single dust grain and R_{wake} is the maximum width of the current wake. The number of ions contained in each half ring is then calculated as the volume multiplied by the density at that grid point, $N_{j,k} = n_{j,k} V_{\text{ring},j,k}/2$.

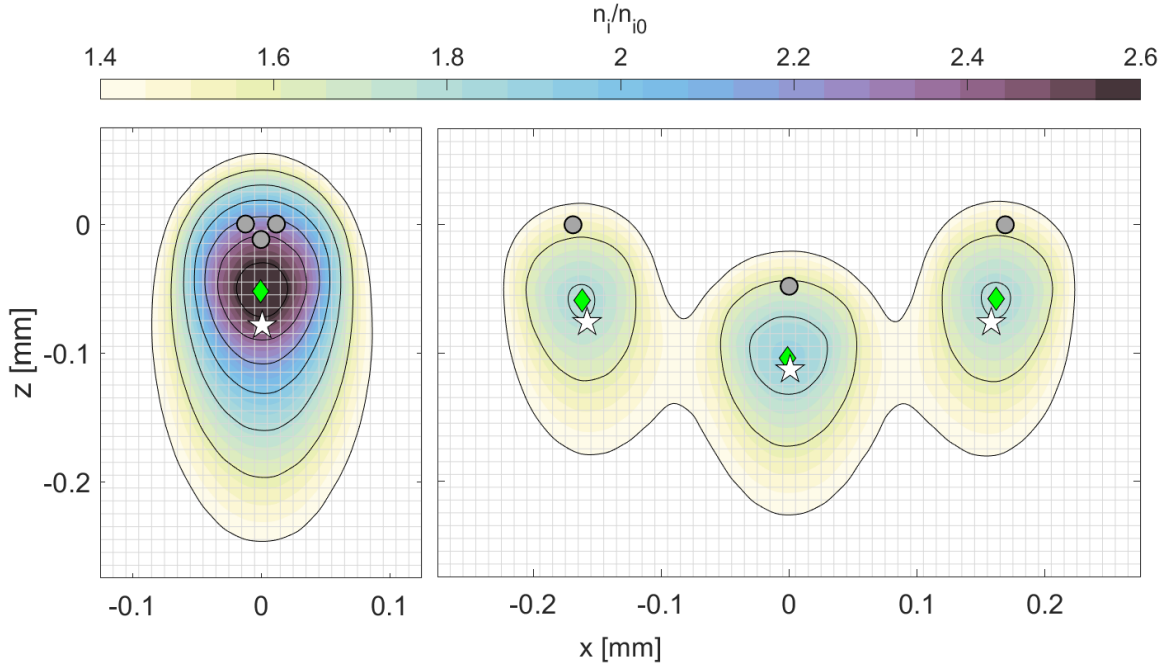


Figure 5.2 Illustration of the 2D grid spacing used to determine 3D characteristics of the ion wake for two representative cases. The contour colors represent the ion density normalized to the background ion density (n_i/n_{i0}) with $0.2 n_i/n_{i0}$ increments indicated by contour lines, the gray circles indicate the location of the dust grains (dust grain size not shown to scale), and the white stars represent the location of the center-of-charge for each wake. The green diamonds indicate the location of the peak ion density in each wake, which is used as the center of the wake for defining radii of 3D rings in the wake. The light gray grid lines represent the position of every 10th grid division (with smaller divisions omitted for visual clarity).

The location of the 3D center-of-charge in the xz -plane is found using the expressions $X = \sum_{j,k}(N_{j,k} \cdot x_{j,k}) / \sum_{j,k}(N_{j,k})$ and $Z = \sum_j(N_{j,k} \cdot z_{j,k}) / \sum_{j,k}(N_{j,k})$, where $x_{j,k}$, and $z_{j,k}$ are the radial and axial positions, respectively, at the grid location (j, k) .

The location of the center-of-charge is assumed to be in the xz -plane (at $y = 0$) since no dust grains were displaced perpendicular to the xz -plane. The position of the center-of-charge calculated in this manner is used to represent the location of the point charge ion wake for the analysis provided in Section 5.5.

5.4 Results

The DRIAD simulation output includes the time evolution of dust grain charges and local ion number density. The total electric potential can then be calculated directly as a combination of the location of dust grains and their charge, the local ion number density in the simulation region, and the ions outside the simulation region (which are assumed to be uniformly distributed). The dust grain charge and local ion number density both vary with the interparticle separation of the dust grains and their orientation relative to the axial electric field, and these results are presented in Sections 5.4.1 and 5.4.2. It will be shown that the variation of dust grain charge and ion number densities lead to interesting results for calculating the total electric potential, and these results are presented in Section 5.4.3.

5.4.1 Dust Grain Charge

The charge of a dust grain is output at 0.001 ms intervals by the DRIAD simulation, and fluctuates due to the discrete nature of ion collection by dust grains (Cui 1994, Matthews 2020). The discrete charging process results in overall variations on a scale of a few percent of the total charge, or approximately 100 elementary charges. Since the scale of charge fluctuations for a given dust grain is small compared with the variations in dust grain charge between the different simulations, the time averaged dust grain charge is used for the remainder of results presented.

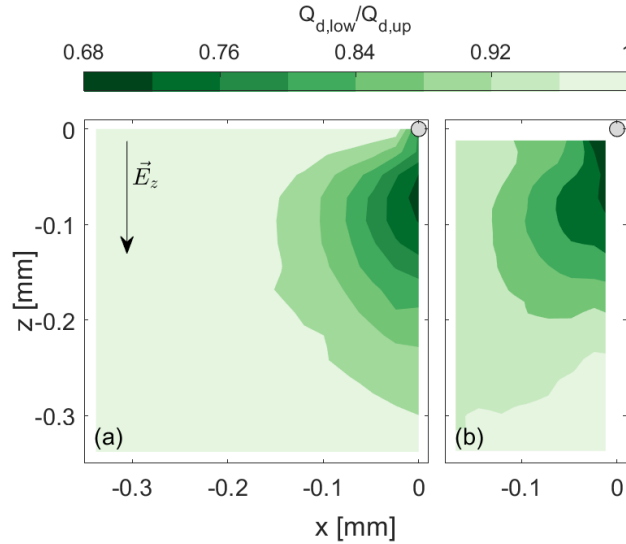


Figure 5.3 Results from two (a) and three (b) dust grain simulations illustrating lower dust grain charge as a fraction of upper right dust grain charge ($Q_{d,low}/Q_{d,up}$) at each location relative to the upper right dust grain position, with the upper dust grain position indicated by the gray circle in the top right corner of each panel (not indicative of the size of the dust grain).

The charge on the lower dust grain as a fraction of the charge on the upper (or right) dust grain ($Q_{d,low}/Q_{d,up}$) is presented in Figure 5.3a for the simulations with two dust grains and Figure 5.3b for simulations with three dust grains. The positions in the contour plot represent the locations of the lower dust grain relative to the upper (or right) dust grain (indicated by the gray circle at the origin in each panel), and the color of the contours correspond to the ratio of charges. Approximately equal upper and lower grain charges are indicated by the lightest shade of green and positions where the lower dust grain has the greatest decharging relative to the upper dust grain are shown as the darkest shade of green. The relative charge on the lower dust grain is reduced as the separation between the dust grains decreases, and their reduction in charge is greatest for lower dust grains positioned directly beneath the upper dust grain (i.e., parallel to the axial electric field direction). The lower dust grain charge in simulations of three dust grains is found

to approach that of the upper right dust grain charge at smaller parallel interparticle separations than in the two dust grain simulations, seen as the lightest green patch near the x axis of Figure 5.3b. This effect is most significant when the two upper dust grains have interparticle separations less than about $8 \lambda_{Di}$ (0.2 mm).

5.4.2 Ion Number Density

The position in the ion wake where the ion density reaches a maximum value will be located below the dust grain if only one dust grain is present, but the location of the maximum ion density can shift in response to the number and positions of dust grains when two or more dust grains are present.

5.4.2.1 Single dust grain. The ion density results for the single dust grain simulation are shown in Figure 5.4 as a contour plot (a) and scatter plot (b) showing the location and peak value of the ion density found along rays originating from the dust grain position at ten degree increments. The largest ion density is located along the direction parallel to the axial electric field, $-\hat{z}$ (0° , as indicated by the black arrow in (a)), with distance and the peak ion density value decreasing as the angle increases until 90° . For angles greater than 90° , the maximum ion density value is at the dust grain surface, seen in Figure 5.4b as the data points that are positioned along the x -axis of the plot.

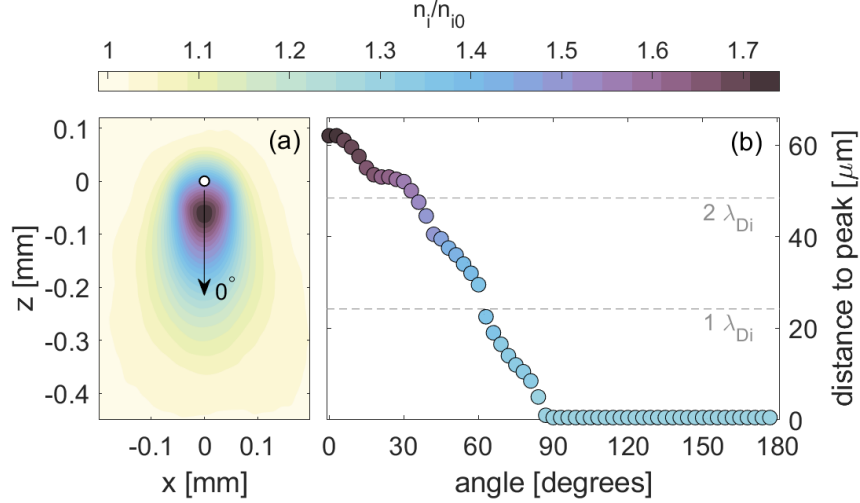


Figure 5.4 Results from the simulation of a single dust grain showing (a) the ion density as a contour plot with the location of the dust grain marked by a white circle outlined in black (not indicative of the size of the dust grain), and (b) the distance to the maximum ion density location along each angle at three degree increments, with the shade of the marker corresponding to the same color scale used in (a) and indicating the magnitude of the ion density normalized to the background ion density value ($n_{i0} = 3 \times 10^{15} \text{ m}^{-3}$). Horizontal light gray lines in (b) indicate the distances from the dust grain in increments of ion Debye lengths (λ_{Di}).

5.4.2.2 *Two dust grains.* Results for the normalized ion density in the two dust grain simulations are shown in Figure 5.5 for representative cases with interparticle separations of 2, 4, 6, 8, 10, 12, and 14 λ_{Di} (columns, left to right) and dust oriented at 90° , 60° , 30° , and 0° relative to the axial electric field (rows, top to bottom). The dust grain locations are indicated by the black outlined white circles, but are not intended to show the size of the dust grains. The dashed black line in each panel of Figure 5.5 indicates the threshold ion density value used to define the ion wake ($n_i/n_{i0} = 1.4$). Simulations of two dust grains revealed three types of wake formations: (i) each dust grain forms a separate ion wake, (ii) one merged ion wake forms for both dust grains, but each dust grain is associated with a separate ion density peak, and (iii) one merged wake forms for both dust grains with only one peak in the ion density. The type of wake that

forms is plotted in Figure 5.6a as a function of the interparticle separation distance (d) in ion Debye lengths and the angle of orientation (θ) relative to the axial electric field direction.

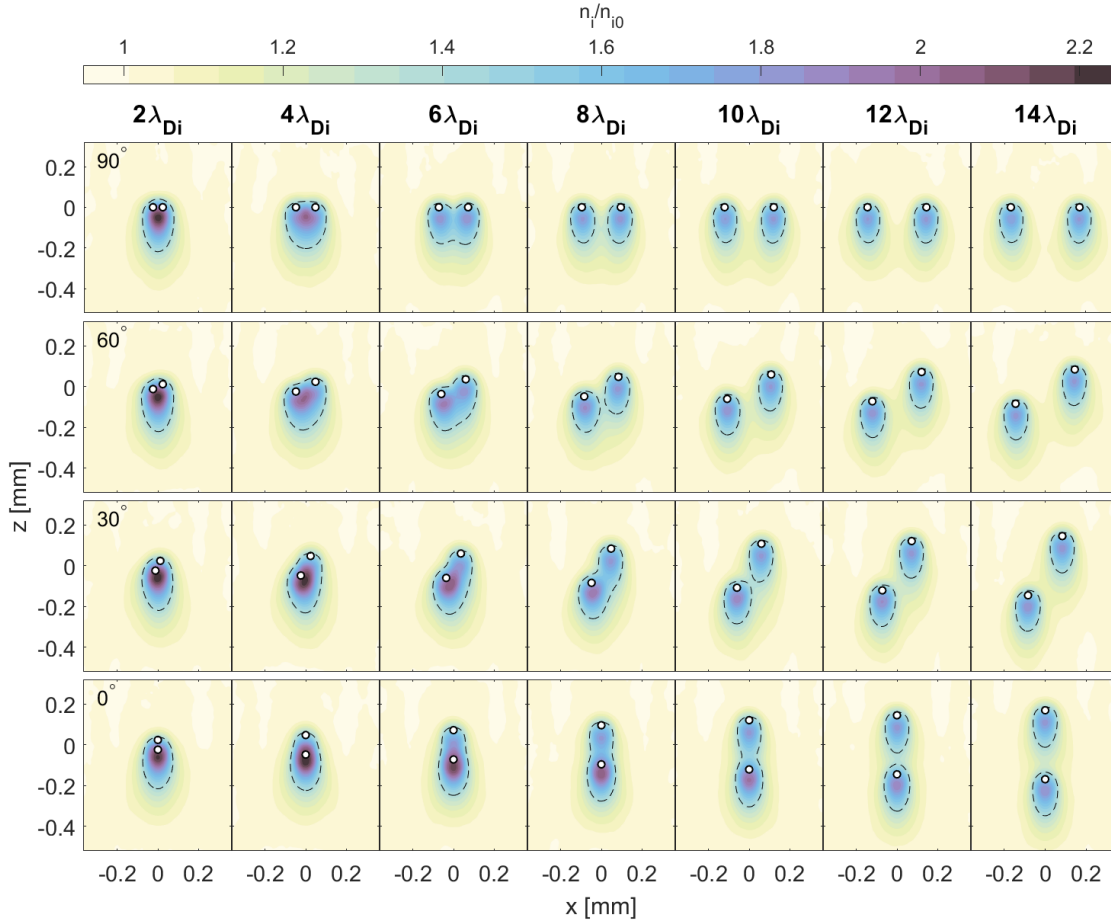


Figure 5.5 Contour plots of normalized ion density for representative cases from the two dust grain simulations. Dust grains separated by 2, 4, 6, 8, 10, 12, and 14 λ_{Di} are shown in the columns from left to right (indicated by the column headings), and dust grains oriented at 90° , 60° , 30° , and 0° relative to the axial electric field are shown in the rows from top to bottom (indicated by the inset text in the leftmost panel of each row). The dust grain locations are indicated by the black outlined white circles (not representative of the size of the dust grains). The ion density values indicated by the colorbars are normalized to the background ion density value, $n_{i0} = 3.0 \times 10^{15} \text{ m}^{-3}$, and the dashed black line in each plot corresponds to $n_i = 1.4 n_{i0}$.

The ion wakes in the two dust grain simulations are qualitatively similar to the single dust grain simulation when the dust grains are positioned near the maximum interparticle separation distance ($14 \lambda_{Di}$ in the parallel or perpendicular directions). However, as the separation between dust grains decreases, the angle of offset between the dust grains becomes significant. This trend can be seen in Figure 5.6(b-j). For a given interparticle separation, the peak ion density and total charge in the lower left ion wake tends to increase as the angle of offset between the dust grains decreases, with the largest variation with the offset angle seen for interparticle separations near 0.1 mm ($\sim 4 \lambda_{Di}$). This result correlates with the ion density contours in the second column of Figure 5.5, where the largest ion density value is seen in the bottom panel, corresponding to the offset angle of 0° (parallel to the axial electric field). In cases where only one ion wake forms for both dust grains, the peak ion density, distance to the center-of-charge in the wake, and total charge in the wake tend to a constant value as the interparticle separation decreases.

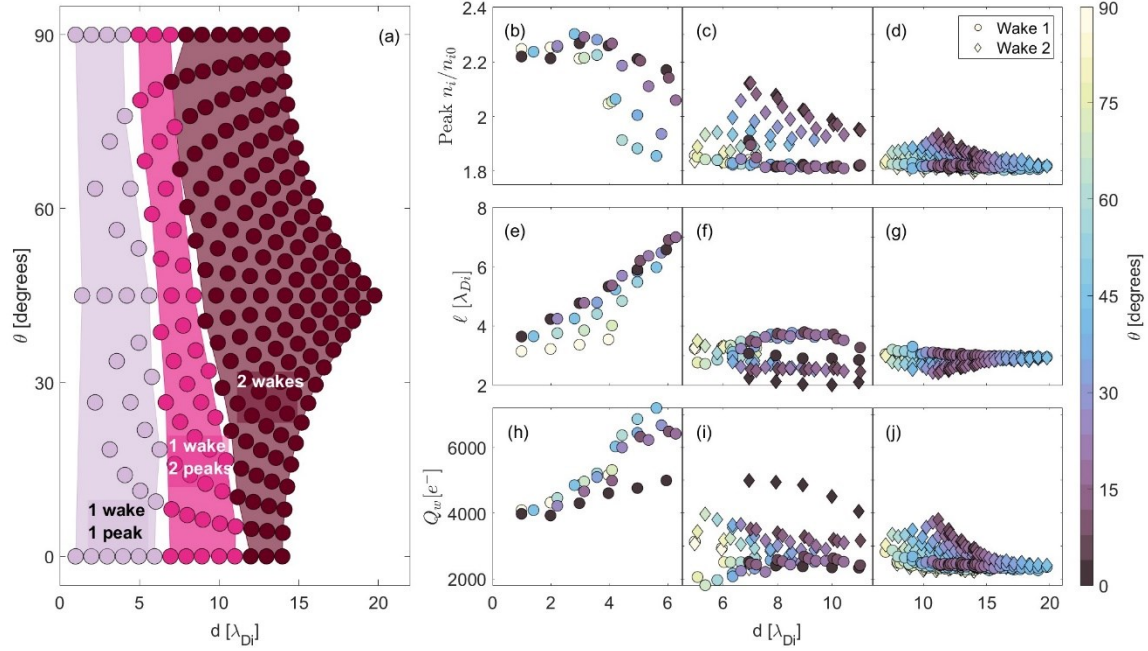


Figure 5.6 Ion wake characteristics from two dust grain simulations showing (a) the number of ion wakes as a function of interparticle separation (d) and angle of orientation (θ) relative to the axial electric field, (b-d) peak ion density value in the wake, (e-g) the distance to the center-of-charge in the ion wake, and (h-j) the charge in the ion wake. Panels (b), (e), and (h) correspond to cases where a single merged ion wake with one peak forms for both dust grains, panels (c), (f), and (i) correspond to cases where a single ion wake with two peaks forms, and panels (d), (g), and (j) correspond to cases when two separate ion wakes formed. The shade of the markers in (b-j) represent the angle of orientation relative to the axial electric field, with 0° as the darkest shade and 90° as the lightest shade. Diamond shaped markers represent the wake for the lower left dust grain, and circle markers represent the wake for the upper right dust grain (or the merged wake when only one peak is present).

The distance to the center-of-charge in the ion wake is largest for dust grains aligned parallel to the axial electric field when only one peak is present, and under these conditions the center of charge shifts below the lower dust grain. The largest peak ion density value is seen in cases with a single merged ion wake with only one density peak, and for a given interparticle separation the value of the peak varies with orientation angle by up to $0.35 n_i/n_{i0}$ at interparticle separations between $5 - 7 \lambda_{Di}$. The largest wake charge is found in cases oriented at less than 30° with respect to the axial electric field

with interparticle separation near $6 \lambda_{Di}$, and corresponds to cases that form one merged ion wake with a single ion density peak. In cases where two separate ion wakes form, the peak ion density, distance to the center-of-charge in the wakes, and amount of charge contained in the wakes tends toward the same value as the interparticle separation distance is increased, and the ion wakes resemble those formed by single, isolated dust grains. It is important to note that although panels (d), (g), and (j) of Figure 5.6 represent cases where separate wakes formed for both dust grains, there is still variation in the amount of charge ($1400 e^-$), distance to the center-of-charge ($0.7 \lambda_{Di}$), and peak ion density ($0.12 n_i/n_{i0}$) found in the wakes of the upper and lower dust grains, and the variation is most significant for cases oriented at angles less than 30° from the axial electric field direction.

5.4.2.3 Three dust grains. Contour plots depicting the ion density from representative simulations with three dust grains are provided in Figure 5.7. Cases with the upper two dust grains separated by 2, 4, 6, 8, 10, 12, and $14 \lambda_{Di}$ are shown in the columns from left to right (indicated by the column headings), and lower dust grains oriented at 65° , 45° , and 30° relative to the axial electric field are shown in the rows from top to bottom (as indicated by the inset text in the leftmost panel of each row). The dashed black line in each panel represents the threshold ion density value used to define the extent of the ion wakes ($n_i/n_{i0} = 1.4$). When the upper two dust grains are positioned less than $8 \lambda_{Di}$ apart in the direction perpendicular to the axial electric field, a single merged ion wake forms with only one peak value, which is positioned at or below the lower dust grain. Increasing the interparticle separation of the upper two dust grains leads to the formation of a large, merged wake with multiple peak values, and the largest

separation yields three separate wakes as seen in the three lower right panels of Figure 5.7. The type of wake that forms is plotted in Figure 5.8a as a function of the interparticle separation distance (d) in ion Debye lengths and the angle of orientation (θ) relative to the axial electric field direction.

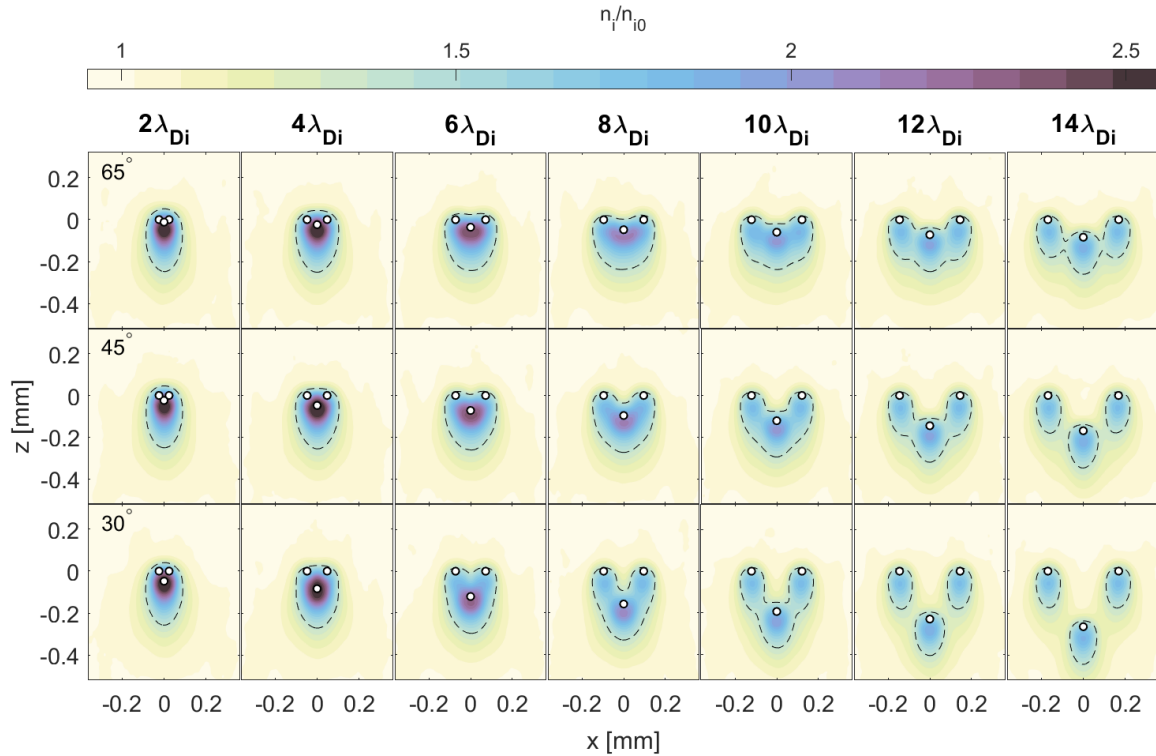


Figure 5.7 Contour plots of normalized ion density for representative cases from the three dust grain simulations. Cases with the upper two dust grains separated by 2, 4, 6, 8, 10, 12, and 14 λ_{Di} are shown in the columns from left to right (indicated by the column headings), and lower dust grains oriented at 65° , 45° , and 30° relative to the axial electric field are shown in the rows from top to bottom (indicated by the inset text in the leftmost panel of each row). The ion density values indicated by the colorbars are normalized to the background ion density value, $n_{i0} = 3.0 \times 10^{15} \text{ m}^{-3}$, and the dashed black line in each plot corresponds to $n_i = 1.4 n_{i0}$.

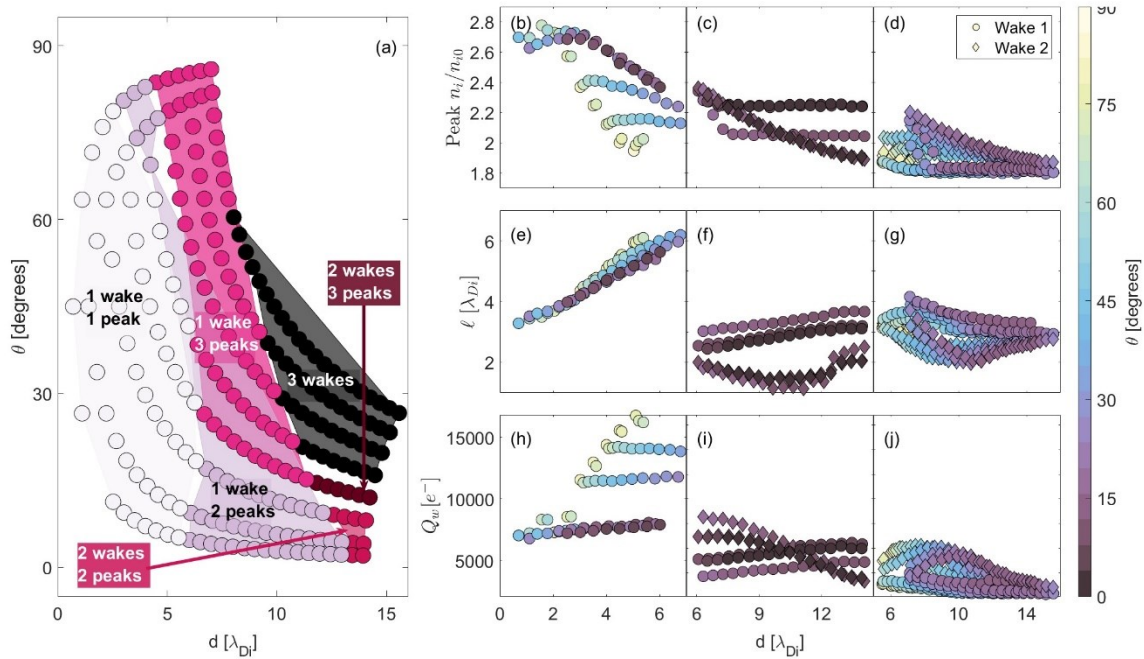


Figure 5.8 Ion wake characteristics from simulations of three dust grains showing (a) the number of ion wakes as a function of interparticle separation (d) and angle of orientation (θ) relative to the axial electric field, (b-d) peak ion density value in the wake, (e-g) the distance to the center-of-charge in the ion wake, and (h-j) the charge in the ion wake. Panels (b), (c), and (h) correspond to cases where a single merged ion wake with one peak forms for all three dust grains, panels (c), (f), and (i) correspond to cases where a merged ion wake with two peaks forms, and panels (d), (g), and (j) correspond to cases when three separate ion wakes formed. The shade of the markers in (b-j) represent the angle of orientation relative to the axial electric field, with 0° as the darkest shade and 90° as the lightest shade. Diamond shaped markers represent the wake for the lower dust grain, and circle markers represent the wake for the upper right dust grain (or the upper merged wake when fewer than three peaks are present).

The maximum ion density versus the interparticle separation between the upper right dust grain and lower dust grain for each of the simulations with three dust grains is shown in Figure 5.8 for (b) cases with a single merged ion wake with one peak, (c) cases with a merged ion wake and two peaks, and (d) cases with three ion density peaks. Circle markers indicate the peak for the upper right dust grain, and diamond markers indicate the peak for the lower dust grain. The color of each marker indicates the angle between the upper right and lower dust grains, with $\theta = 0^\circ$ (90°) indicating dust grains aligned

parallel (perpendicular) to the axial electric field. The distance to the center-of-charge in the ion wake is shown in Figure 5.8e-g, and the total charge in the ion wake is shown in Figure 5.8h-j for the same wake formations as described in (b-d).

Notably, the amount of charge contained in the ion wake associated with the lower dust grain is found to be smaller than the upper wake when two peaks are present and the separation between upper right and lower dust grains is between $10 - 14 \lambda_{Di}$. The total charge in the ion wake is largest when a merged ion wake with only one peak forms for dust grains oriented at greater than 75° to the axial electric field direction and interparticle separations of $4 - 6 \lambda_{Di}$ between the upper right and lower dust grains. The distance from the center-of-charge in an ion wake to the dust grains is largest in the case of a merged ion wake with a single ion density peak, where the center-of-charge is found below the lower dust grain. The peak ion density value in the wake shows the largest variation for a given interparticle separation in the cases with a merged ion wake and single ion density peak, where the peak ion density value varies by up to $0.6 n_i/n_{i0}$ when the upper right and lower dust grain are separated by $5 \lambda_{Di}$. The ion wakes tend to converge to a single value as the interparticle separation increases when three peaks form in the ion wake. However, as was noted with the simulations of two dust grains, a significant variation in peak ion density, distance to center-of-charge, and total charge in the wake between the upper and lower dust grains persists for interparticle separations as large as $12 \lambda_{Di}$ (most notably for grains aligned parallel to the axial electric field), suggesting that it is unreasonable to treat these as isolated dust grains.

5.4.3 Electric Potential

The total electric potential surrounding the charged dust grains in DRIAD simulations is calculated as a combination of the electric potential due to the ions outside the simulation region (which are assumed to be uniformly distributed and with a density equal to the background ion density value in the simulation, $n_{i0} = 3.0 \times 10^{15} \text{m}^{-3}$), ϕ_i^{out} , ions inside the simulation (based on the local ion number density, ϕ_i^{in} , and the charged dust grain, ϕ_d).

The electric potential components along with the total electric potential ($\phi_{\text{total}} = \phi_d + \phi_i$, where $\phi_i = \phi_i^{\text{in}} + \phi_i^{\text{out}}$) are shown in Figure 5.9 for the simulation with a single dust grain. Panel (a) of Figure 5.9 shows the Coulomb potential of a single, isolated charged dust grain, with $Q_d = 8140 e^-$, panel (b) shows the electron shielded potential from ions inside and outside the simulation region, and panel (c) shows the total electric potential, which is a summation of panels (a) and (b). The increased ion density in the ion wake below the dust grain (visible in Figure 5.4(a)) leads to a region of positive potential, while the negatively charged dust grain creates a large negative potential well.

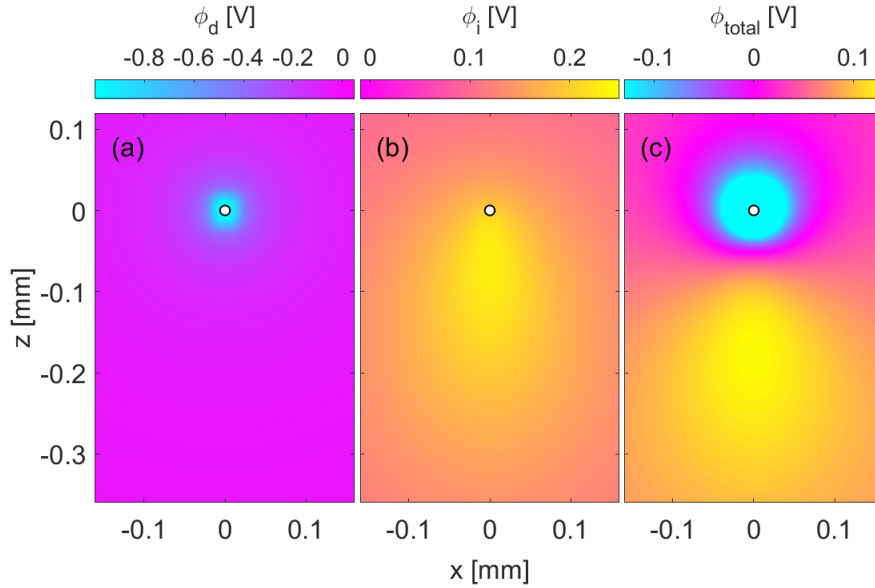


Figure 5.9 Results from a single dust grain simulation showing (a) the Coulomb potential of the charged dust grain, ϕ_d , (b) the electron shielded potential of ions inside and outside the simulation region, ϕ_i , and (c) the total electric potential, ϕ_{total} . The location of the dust grain is marked by the white circle outlined in black (not representative of the actual dust grain size), and the potential is indicated by the contour colors from blue (negative) to yellow (positive).

The total electric potential measured along rays extending from the location of the dust grain at angles from 0° (parallel to the axial electric field) to 180° (anti-parallel to the axial electric field) is depicted in Figure 5.10. The positions of the rays are indicated as lines on the contour plot in panel (a) of Figure 5.10, with the lightest green line representing the parallel direction (0°) and lightest pink line representing the antiparallel direction (180°). Panels (b) and (c) in Figure 5.10 plot the total electric potential measured along the indicated rays, with line colors matching the lines from panel (a). The positive potential region associated with the ion wake positioned 0.08-0.525 mm downstream from the dust grain is clearly visible in the lighter green lines in Figure 5.10b, while the upstream direction shows a shallow negative potential region associated

with a slight ion depletion at radial distances larger than 0.5 mm upstream from the dust grain.

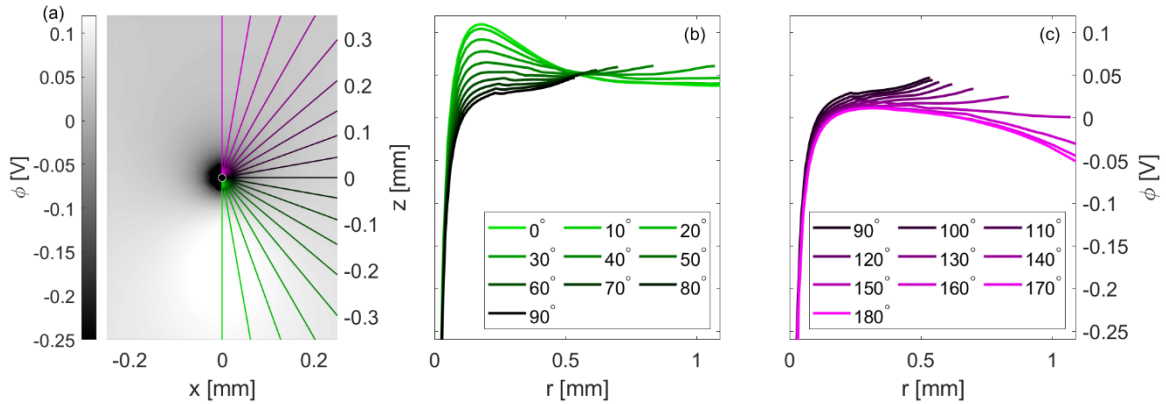


Figure 5.10 Simulation results for the total electric potential surrounding a single dust grain (a) as a contour plot with lines indicating the location of the angles shown in the line plots (b) downstream and (c) upstream from the dust grain location. The shade of the lines in (a)-(c) indicates the angle with respect to the axial electric field direction, with shades growing darker approaching the perpendicular, 90° , and growing lighter green (pink) toward the parallel, 0° (anti-parallel, 180°) direction.

Results for the total electric potential from the simulations with two dust grains are provided in Figure 5.11 for the same representative cases used in Figure 5.5. The accumulation of ions downstream from the dust grains results in a positive potential region, similar to the effect noted in Figure 5.9d for the single dust grain. When one dust grain is positioned downstream from the other, the negative potential region associated with the downstream grain attenuates the positive potential from the upstream grain, resulting in reduced positive potential peak and enhanced negative potential well for the upper grain (most clearly visible in the bottom two rows of Figure 5.11).

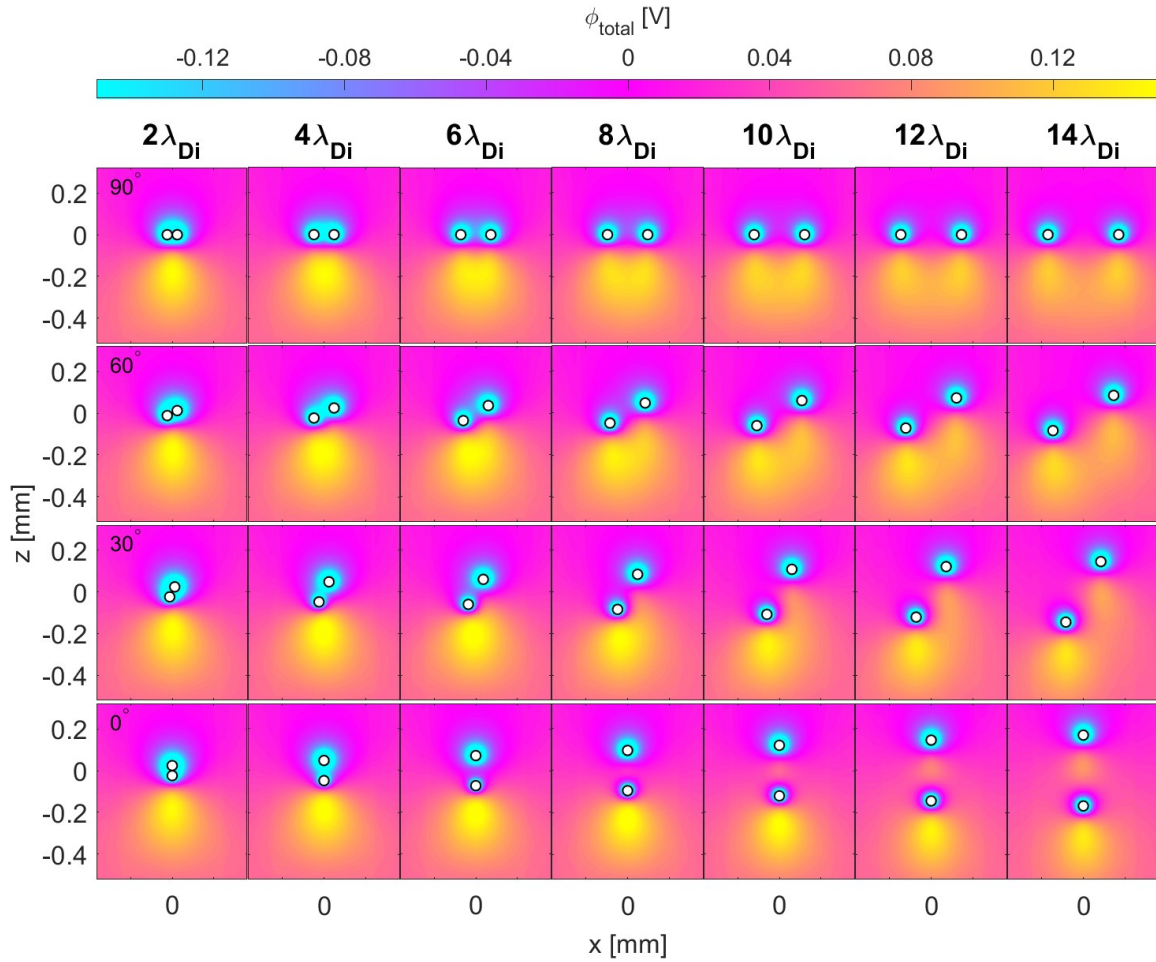


Figure 5.11 Results for the total electric potential from two dust grain simulations showing the same representative cases as in Figure 5.5. Dust grains separated by 2, 4, 6, 8, 10, 12, and 14 λ_{Di} are shown in the columns from left to right (as indicated by the column headings), and dust grains oriented at 90° , 60° , 30° , and 0° relative to the axial electric field are shown in the rows from top to bottom (indicated by the inset text in the leftmost panel of each row). Dust grain locations are marked with white circles outlined in black (not representative of the size of dust grains), and the total electric potential is indicated by the contour colors ranging from blue (negative) to yellow (positive).

The electric potential for three dust grain simulations (the same representative cases from Figure 5.7) are shown in Figure 5.12, where the dust grain locations are indicated by white circles outlined in black and the total electric potential is shown by the contour colors with blue representing a negative potential and yellow representing a positive potential. The results for the total electric potential obtained from simulations

with three dust grains show that the accumulation of positively charged ions downstream from the dust grains leads to a positive potential region, as found for both the single dust grain and two dust grain simulations, with the largest positive potential values found nearest to the lower dust grain.

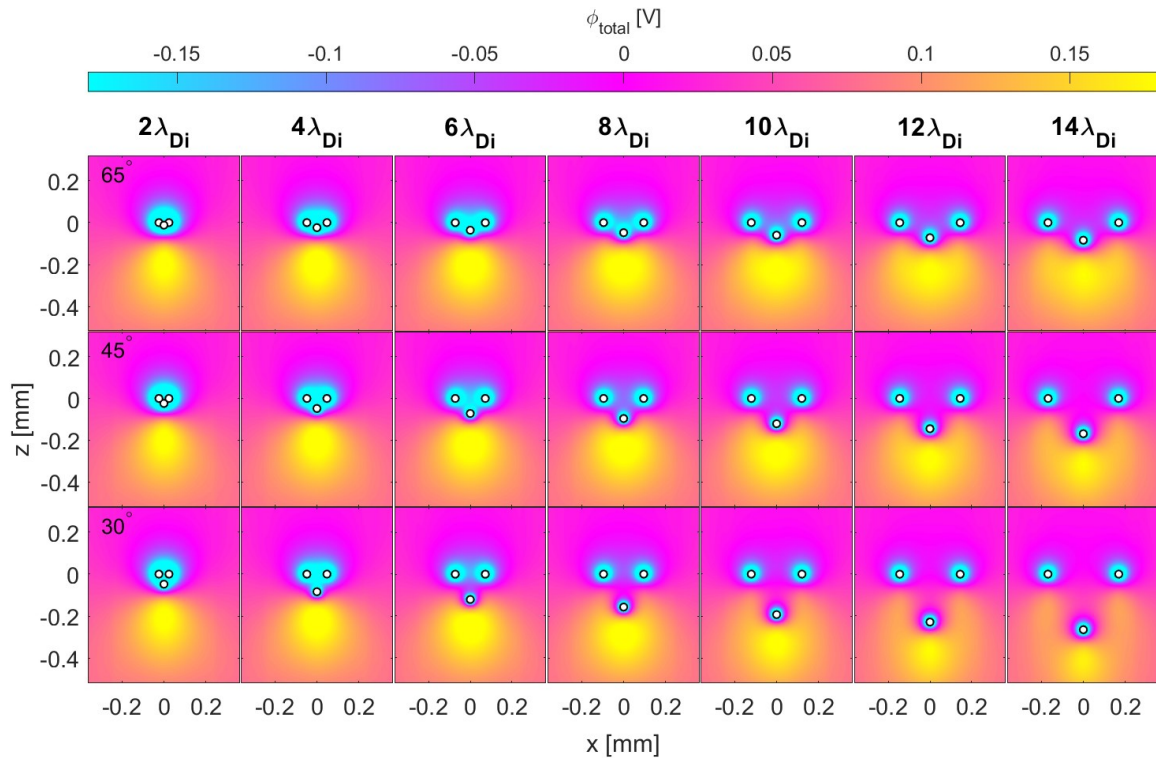


Figure 5.12 Results for the total electric potential from three dust grain simulations showing the same representative cases as in Figure 5.7. Cases with the upper two dust grains separated by 2, 4, 6, 8, 10, 12, and 14 λ_{Di} are shown in the columns from left to right (as indicated by the column headings), with the lower dust grains oriented at 65° , 45° , and 30° relative to the axial electric field shown in the rows from top to bottom (indicated by the inset text in the leftmost panel of each row). Dust grain locations are marked with white circles outlined in black (not representative of the size of dust grains), and the total electric potential is indicated by the contour colors ranging from blue (negative) to yellow (positive).

5.5 Discussion

The electric potential surrounding charged dust grains in a complex plasma is typically expressed as a shielded Coulomb (or Yukawa) potential, $\phi(r) = (Q_d/r) \exp[-r/\lambda_D]$, or as an expansion based upon the velocity distribution or collisionality of the ions, as in (Kompaneets 2007b). However, both forms of the electric potential have limited validity and should be applied with caution. The Debye potential is known to break down very near the dust grain surface where the electron and ion distributions are unable to be calculated using a linear approximation (Lampe 2000), even in the case of a stationary plasma, and the expansion based on velocity distribution and ion collisionality is valid only for distances $r \gg \lambda_D$ (Kompaneets 2007b).

5.5.1 Model for Electric Potential

The precise electric potential obtained from simulations of one, two, and three dust grains provides an opportunity to quantify the ion wake contributions to their total electric potential. The Coulomb potential of a single, negatively charged dust grain is negative at all points and tends to zero as the distance from the dust grain tends to infinity (as shown in Figure 5.9a). Even if the Debye potential is used with a shielding length that varies as a function of the direction relative to the axial electric field, the positive potential region due to the ion wake is not represented. The positive region downstream from the dust grain may be recovered by adding a constant value to the potential at all points, but this solution provides a potential that no longer tends to zero as r tends to infinity. A comparison between the total electric potential results obtained from DRIAD for two dust grains with the Coulomb potential and Yukawa potential are shown in Figure 5.13. Even when the potentials are shifted by adding or subtracting a constant value, the

large positive potential region downstream from the dust grains visible in the DRIAD simulation results is not captured by either the Coulomb or Yukawa form of the potential.

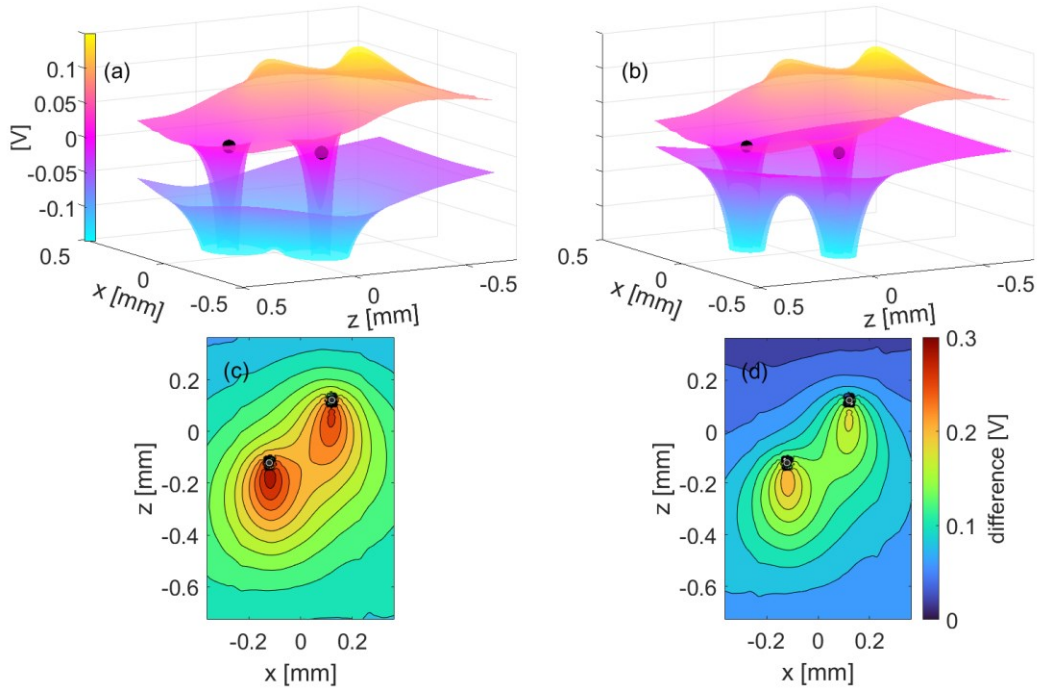


Figure 5.13 Comparison between the total electric potential obtained from DRIAD simulation results (upper surfaces) with the (a) Coulomb potential and (b) Yukawa potential (lower surfaces). The colors of the surfaces correspond to the potential (measured in Volts), and the black circles indicate the location of the dust grains (dust grain size not to scale). The difference between the simulation results and the Coulomb potential is shown in (c) and the difference between simulation results and the Yukawa potential is shown in (d), where the color of the contours corresponds to the difference between the upper and lower surfaces in panels (a) and (b).

In order to capture the electric potential features arising from the ion wake, the form of the electric potential must include a term which causes the potential to be positive at the location of the ion wake. A modification to the Yukawa potential can be made which treats the ion wake as an additional shielded point charge, and allows the shielding lengths to vary based on the angle with respect to the axial electric field:

$$f(r, \theta) = \sum_{i=1}^{N_d} \left\{ \begin{aligned} & \frac{kQ_{d,i}}{\sqrt{(\vec{r} - \vec{r}_{d,i})^2}} \exp \left[\kappa_{d,i}(\theta) \cdot \sqrt{(\vec{r} - \vec{r}_{d,i})^2} \right] \\ & + \frac{kQ_{w,i}}{\sqrt{(\vec{r} - \vec{r}_{w,i})^2}} \exp \left[\kappa_{w,i}(\theta) \cdot \sqrt{(\vec{r} - \vec{r}_{d,i})^2} \right] \end{aligned} \right\} + c. \quad (5.2)$$

The first term in the sum of Equation 5.2 is the shielded potential from the i^{th} dust grain with charge $Q_{d,i}$ located at $\vec{r}_{d,i}$ with shielding length $1/\kappa_{di}$, and the second term is the shielded potential from the ion wake associated with the i^{th} dust grain located at $\vec{r}_{w,i}$ with charge $Q_{w,i}$ and shielding length $1/\kappa_{wi}$. By including the term corresponding to the positive ion wake, the modified Yukawa expression generates a potential which is positive at the ion wake location and negative near the dust grains. Thus, the potential in Equation 5.2 is able to qualitatively reproduce the simulation results, as shown in panel (a) of Figure 5.14, with the difference between the simulation results and Equation 5.2 shown in the contour plot of Figure 5.14c. At distances beyond $1 \lambda_{Di}$ upstream and $5 \lambda_{Di}$ downstream from the dust grain, the potential described by Equation 5.2 varies from the simulation results by less than 0.05 V. However, just as with the original Yukawa potential, the modified form of the Yukawa potential in Equation 5.2 is seen to be invalid near the location of the negative dust grains due to the $1/r$ dependence, and further breaks down near the location of the positive point charge representing the ion wake (visible as the white open areas in Figure 5.14c). This means that while this modification is able to account for the changing shielding length which results from the flowing ions, it fails to describe the potential at the lengths relevant for the interaction of multiple dust grains.

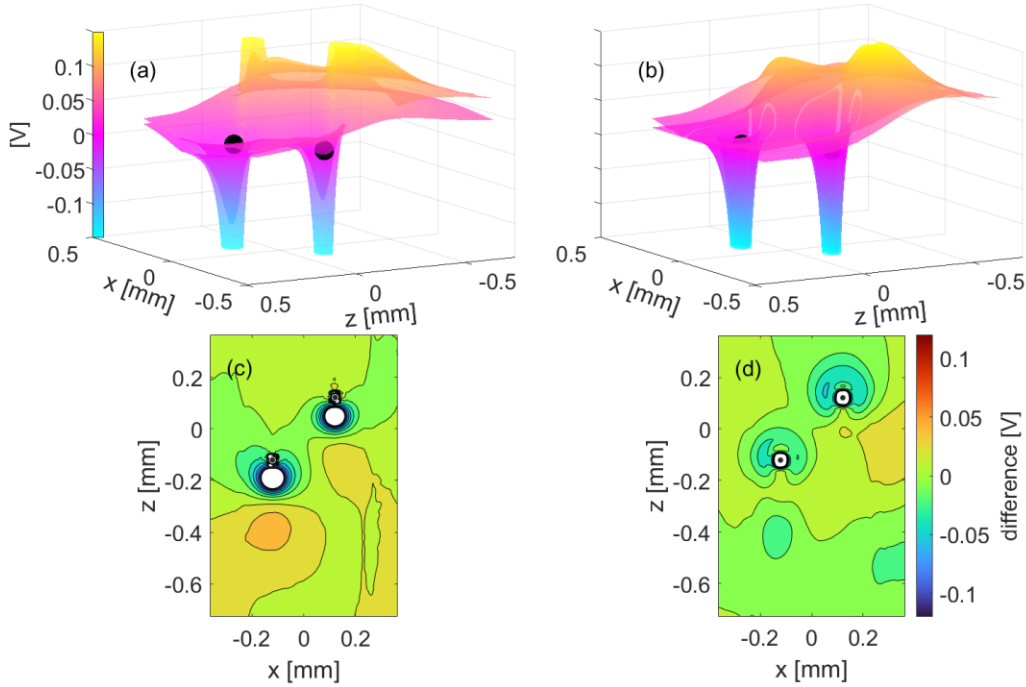


Figure 5.14 Comparison between the total electric potential in two dust grain DRIAD simulation (a) with the potential determined by Equation 5.2 and (b) with the potential determined by Equation 5.3, using the dust grain charge and ion wake charge determined from DRIAD simulation results. The colors of the surfaces correspond to the electric potential (measured in Volts), and the black circles indicate the location of the dust grains (dust grain size not to scale). The difference between the simulation results and the potential determined by Equation 5.2 is shown in (c), and the difference between the simulation results and the potential determined by Equation 5.3 is shown in (d), where the contour colors represent the difference between the upper and lower surfaces in panels (a) and (b).

A model for the electric potential which includes the influence from negatively charged dust grains and the positively charged ion wakes but which does not become invalid near the location of the charges can be found by using Gaussian functions to represent the charged dust grains and positive ion wakes, as shown in Equation 3. With this expression, the potential is no longer subject to a dependence on $1/r$, and the depth (peak) in the potential at the dust grain surface (point charge wake) is set by the coefficient $kQ_{d,i}$ ($kQ_{w,i}$).

$$\phi(x, z) = \sum_{i=1}^{N_d} \left\{ \begin{array}{l} kQ_{d,i} \exp \left[\begin{array}{l} -a_{d,i}(x - x_{d,i})^2 - 2b_{d,i}(x - x_{d,i})(z - z_{d,i}) \\ -c_{d,i}(z - z_{d,i})^2 \end{array} \right] \\ + kQ_{w,i} \exp \left[\begin{array}{l} -a_{w,i}(x - x_{w,i})^2 - 2b_{w,i}(x - x_{w,i})(z - z_{w,i}) \\ -c_{w,i}(z - z_{w,i})^2 \end{array} \right] \end{array} \right\} \quad (5.3)$$

where k represents the Coulomb constant, $Q_{d,i}$ and $Q_{w,i}$ are the dust and ion wake charges for the i^{th} dust grain, and the constants a , b , and c are the elliptic Gaussian coefficients $a = \frac{\cos^2 \theta}{2\sigma_x^2} + \frac{\sin^2 \theta}{2\sigma_z^2}$, $b = \frac{\sin 2\theta}{4\sigma_x^2} - \frac{\sin 2\theta}{4\sigma_z^2}$, and $c = \frac{\sin^2 \theta}{2\sigma_x^2} + \frac{\cos^2 \theta}{2\sigma_z^2}$. The width of the Gaussian peak in the \hat{x} or \hat{z} directions are determined by the value of σ_x and σ_z , respectively, and the angle θ determines the orientation of the Gaussian peak with respect to the axial electric field. Using the elliptic Gaussian to represent the total electric potential achieves much closer agreement with the simulation results, as shown in Figure 5.14b and d. The form of the potential described by Equation 5.3 varies by less than 0.035 V for distances larger than $1 \lambda_{Di}$ in all directions from the dust grain surface, as well as reproducing the positive potential associated with the ion wake downstream from the dust grains. It is further seen that the elliptic Gaussian function eliminates the anomalous behavior of the Yukawa potential as $r \rightarrow r_d$, and the coefficients a , b , and c allow the potential structure in the ion wake to be fit with greater precision.

The ability of the potential form described by Equation 5.3 to reproduce the DRIAD simulation results is due in large part to the specificity in the coefficients. As a result, there are three coefficients for each of the dust grains and ion wakes which must be determined for every configuration of dust grains. To determine overall trends within the coefficients, fitting each coefficient individually quickly becomes an intractable problem. However, new developments in machine learning may provide a method for

evaluating the large requisite number of dust grain separations and orientations relative to the axial electric field direction in order to determine the coefficients for the model in Equation 5.3.

The complexities which arise from attempting to model the total electric potential dependence on dust grain locations and charges might lead one to rely on simplifications such as treating the potential from multiple dust grains as a superposition of the single dust grain potentials. However, as shown in Figure 5.15, while the total electric potential resulting from the superposition of single dust grain potentials is able to qualitatively reproduce the positive potential regions for larger dust grain separations (Figure 5.15b, d, f, h), this method fails to capture the enhanced positive potential resulting from strong ion focusing below the downstream dust grains or the extended negative potential well surrounding the upstream grain (Figure 5.15a, c, e, g). It is evident that in order to predict the precise form of electric potential surrounding any given dust grain in a collection of dust grains, information about the location and charge of dust grains both upstream and, perhaps surprisingly, downstream from that dust grain are necessary.

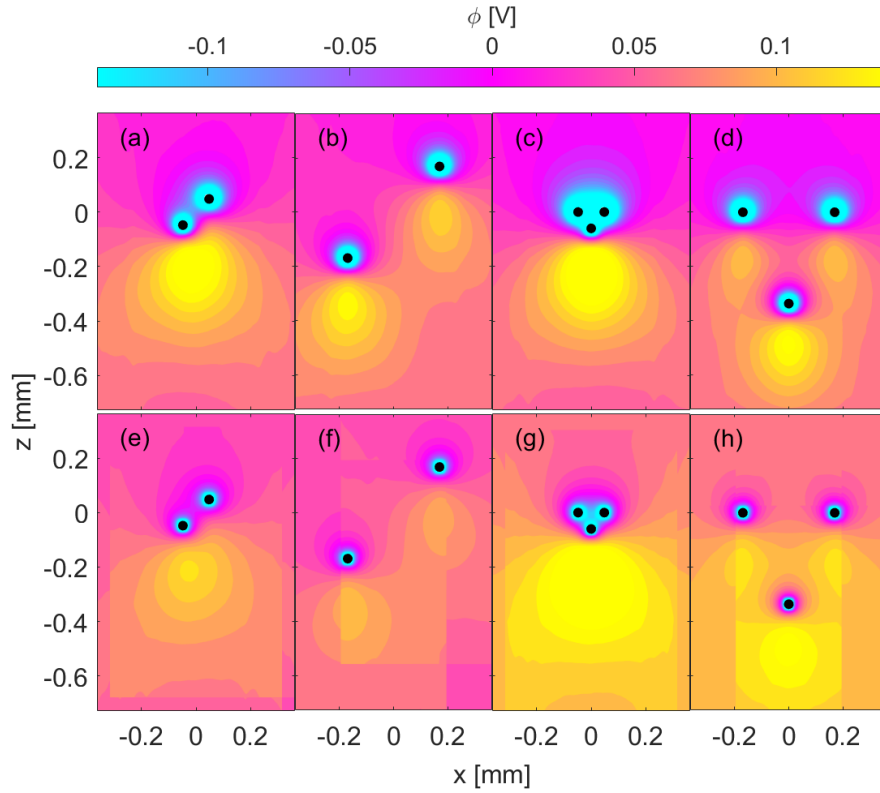


Figure 5.15 Comparison between the DRIAD simulation results for four representative cases with two and three stationary dust grains (a-d) and the total electric potential which results from a superposition of the single dust grain simulation results at each dust grain location (e-h). The dust grain locations are indicated by black circles in each plot (not representative of the actual size of dust grains), and the contour colors indicate the value of the total electric potential, ϕ , measured in Volts.

5.5.2 Minimum Energy Configuration

Dust grains in a complex plasma will self-organize into stable single chains, zigzags, and twisted helices when the configuration is one that minimizes the energy of the dust grains, ions, and confinement potential. A typical expression for the configuration energy of a collection of dust grains is

$$U = \sum_{i=1}^N \left[\frac{1}{2} m \omega^2 r_i^2 \right] + \sum_{i=1}^N \sum_{j=1}^{j<i} \left[\frac{k Q_i Q_j}{r_{ij}} \exp \left(-\frac{r_{ij}}{\lambda_D} \right) \right] \quad (5.4)$$

where m is the mass of a dust grain, ω relates to the strength of the confinement potential, r_i is the position of the i^{th} dust grain, k is the Coulomb constant ($8.99 \times 10^9 \text{ V} \cdot \text{m/C}$), Q_i and Q_j are the charges of dust grain i and j , respectively, $r_{ij} = \sqrt{\vec{r}_i - \vec{r}_j}$ is the distance between dust grains i and j , and λ_D represents the shielding length. The first term is the energy of the dust grain due to the position within the confining potential, and the second term accounts for the energy between pairs of dust grains. To include the contribution from the ion wake, one may treat the ion wake as a point charge and add another term like the second term in Equation 5.4 which describes the interaction energy between a dust grain and the ion wakes associated with the other dust grains (as in Melzer 2014, for example), resulting in the following equation

$$U = \sum_{i=1}^N \left[\frac{1}{2} m \omega^2 r_i^2 \right] + \sum_{i=1}^N \sum_{j=1}^{j<i} \left[\frac{k Q_i Q_j}{r_{ij}} \exp \left(-\frac{r_{ij}}{\lambda_D} \right) \right] + \sum_{i=1}^N \sum_{j' \neq i}^N \left[\frac{k Q_i Q_{j'}}{r_{ij'}} \exp \left(-\frac{r_{ij'}}{\lambda_D} \right) \right] \quad (5.5)$$

where the subscript j' indicates the ion wake associated with the j^{th} dust grain.

The variation of the dust grain charge, charge in the ion wake, and location of the ion wake all depend on the location of the dust grains, which makes it difficult to accurately predict the location of an additional dust grain that will produce a minimum energy configuration. This can be illustrated by comparing the results from two and three dust grain simulations. The contour plots in Figure 5.16 show the energy, U , calculated from simulations with two dust grains positioned at (a) $2 \lambda_{Di}$, (b) $4 \lambda_{Di}$, (c) $6 \lambda_{Di}$, (d) $8 \lambda_{Di}$, (e) $10 \lambda_{Di}$, (f) $12 \lambda_{Di}$, and (g) $14 \lambda_{Di}$ apart in the direction perpendicular to the

axial electric field direction. The shade of the contour indicates the energy associated with a third dust grain located at that grid point. The energy calculation is performed considering only the interaction between charged particles, using the last two terms in Equation 5.5.

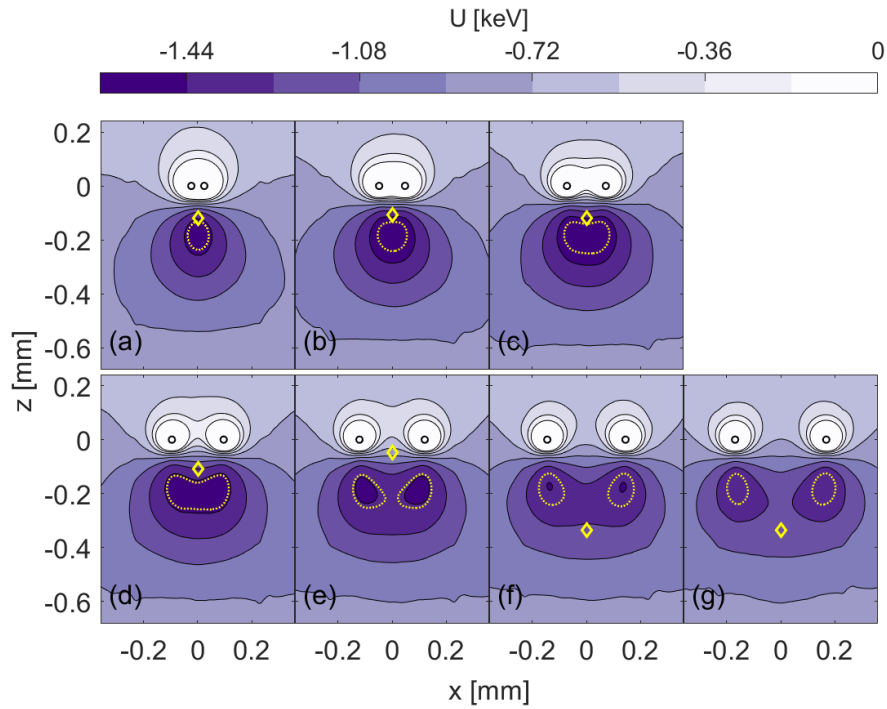


Figure 5.16 Contour plots illustrating the potential energy (U) from simulations of two dust grains positioned (a) $2 \lambda_{Di}$, (b) $4 \lambda_{Di}$, (c) $6 \lambda_{Di}$, (d) $8 \lambda_{Di}$, (e) $10 \lambda_{Di}$, (f) $12 \lambda_{Di}$, and (g) $14 \lambda_{Di}$ apart in the direction perpendicular to the axial electric field direction (dust grain locations are indicated by the open black circles). The dotted yellow contour line in each panel indicates the location where the energy is within 95% of the minimum energy. The yellow diamond in each panel represents the minimum energy location for the third dust grain determined from the results of simulations with three dust grains.

One might expect that a third dust grain positioned within the yellow dotted contour line of Figure 5.16 (indicating the region where the energy is within 5% of the minimum energy) would produce a minimum energy configuration. However, as indicated by the yellow diamonds in each panel, the location of the third dust grain where

the energy of the configuration is at a minimum is nearer to the upper two dust grains for panels (a)-(e) (corresponding to upper dust grain separations $2 - 10 \lambda_{Di}$ perpendicular to the axial electric field direction), and further from the upper two dust grains for panels (f) and (g) (corresponding to upper dust grain separations of 12 and 14 λ_{Di} perpendicular to the axial electric field direction).

It is important to note that the third dust grain was centered between the upper two dust grains in all simulations of three dust grains, while the expected location of the third dust grain would be beneath the left or right dust grain (based upon energy calculations from two dust grain simulations). Additional simulations with the third dust grain placed at the point of minimum energy determined from two dust grain simulations (shown in Figure 5.16 by the stars) were performed to verify if the offset lower dust grain would result in a lower energy configuration than the centered lower dust grain. The offset lower dust grain configurations were found to have higher configuration energies for all separation distances of upper dust grains than the simulations with centered lower dust grains, with the largest difference noted for smaller upper dust grain separations. The changes in the dust grain charges, amount of charge contained in the ion wake, and ion wake locations when the third dust grain is added are likely to be responsible for the difference between the predicted minimum energy location for the third dust grain and actual minimum energy configuration.

Contour plots of the total electric potential for simulations with the third dust grain at the minimum energy position when centered between the upper two dust grains (top row) and placed at the minimum energy location predicted from two dust grain simulations (bottom row) are provided in Figure 5.17. The total electric potential in the

bottom row shows that placing a third dust grain at the predicted minimum energy location below the upper right dust grain prevents the formation of an ion wake below the upper right dust grain and results in a highly asymmetric charge configuration. The uneven distribution of charges is a driving factor for the larger energy found in all cases where the lower dust grain is offset, suggesting that the centered lower dust grain is a lower energy configuration. This is an interesting result since it has been experimentally observed that dust grains forming a zigzag, or double chain, structure will typically have a lowest dust grain which is centered relative to the rest of the configuration, as seen in Hyde 2013, Melzer 2006, and Kamimura 2012, for example.

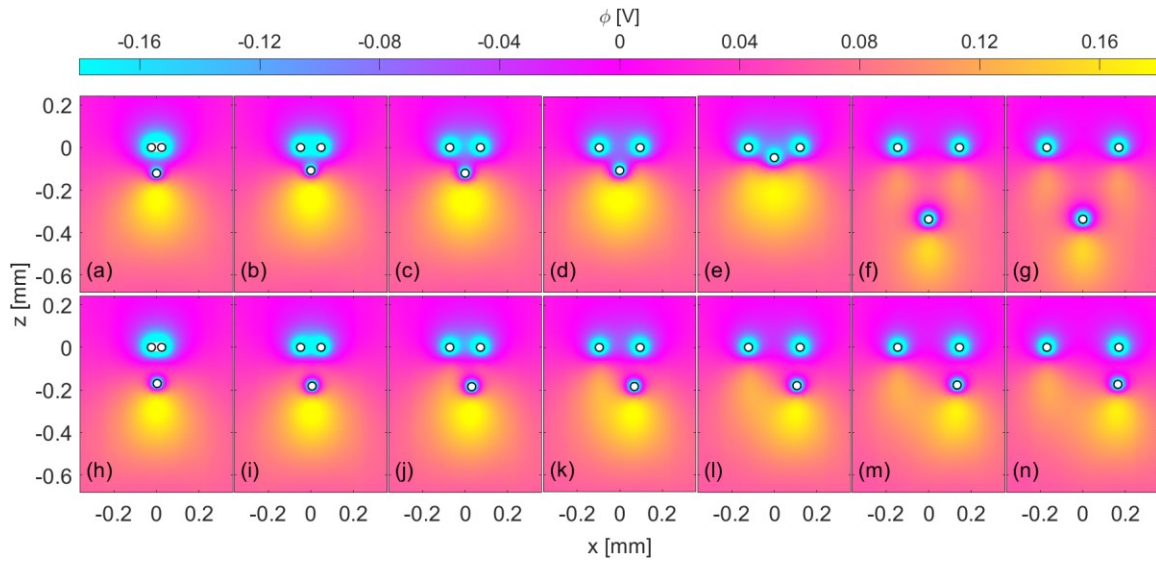


Figure 5.17 Contour plots illustrating the total electric potential for three dust grain simulations with the lower dust grain at the position with the minimum energy centered between the upper two dust grains (top row) and at the minimum energy position calculated from two dust grain simulations shown in Figure 5.16 (bottom row). The upper two dust grains are positioned at $2 \lambda_{Di}$ (a and h), $4 \lambda_{Di}$ (b and i), $6 \lambda_{Di}$ (c and j), $8 \lambda_{Di}$ (d and k), $10 \lambda_{Di}$ (e and l), $12 \lambda_{Di}$ (f and m), and $14 \lambda_{Di}$ (g and n) apart in the direction perpendicular to the axial electric field direction. Dust grain locations are indicated by the white circles, but do not represent the actual size of the dust grains.

5.6 Conclusion

The self-organization of dust grains into single chains, zigzags, and twisted helices depends upon the energy of each configuration, with stable structures forming when the structure is at a minimum energy configuration. The energy of a given dust structure is determined by Equation 5.5, and is known to depend upon the location and charge of individual dust grains, the charge contained in the ion wakes that form downstream from the dust grains, and the position of the center-of-charge in the ion wake. Results from the simulations of one, two, and three stationary dust grains were analyzed to quantify the changes to the dust grain charge, location and amount of charge in the ion wake, and total electric potential in the presence of dust grains with precise interparticle separations and orientations relative to the axial electric field direction in order to provide a foundation for accurate predictions of minimum energy configurations.

In Section 5.4.1, it was shown that a dust grain placed downstream from one or two dust grains will have up to a 30% reduction in charge compared with the upstream grain, with the largest reduction seen for grains aligned directly below the upper grains. The charge reduction for the lower dust grain in three dust grain simulations occurs over a shorter range in the direction parallel to the axial electric field, suggesting that the ion focusing effect is reduced with two upstream dust grains compared with a single upstream dust grain.

The formation of ion wakes in the two and three dust grain simulations (discussed in Section 5.4.2.2 and 5.4.2.3) was found to have a strong dependence on the orientation of dust grains relative to the axial electric field for interparticle separations less than 4 mm ($16 \lambda_{Di}$), while the ion wakes that formed at larger interparticle separations tended to

share characteristics with the single dust grain results. The ion wakes for two and three dust grains merged into one larger wake as interparticle separation is reduced, with the location of the center-of-charge in the ion wake shifting to be closer to (or below) the lower dust grain.

The total electric potential in the case of a single dust grain has a positive potential region downstream from the dust grain that corresponds to the increased positive ion concentration in the ion wake, while the dust grain creates a large negative potential well due to the negative dust grain charge. When a second or third dust grain is introduced, the changes to the ion wake and dust grain charge lead to changes in the total electric potential which are challenging to predict. The typical analytic potential models are unable to reproduce the positive potential region that arises from the ion wake, and break down in the region very near the dust grains. A model which uses Gaussian functions to describe the potential of the negatively charged dust grains and positively charged ion wakes (treated as a point charge) is proposed as a possible solution for describing the electric potential near the dust grains. Due to the large numbers of coefficients needed for the potential model using Gaussian functions, an approach utilizing machine learning is expected to be useful for further developing this model into a useful tool for predicting the minimum energy configurations based upon given plasma conditions, and will be the focus of future investigation.

CHAPTER SIX

Conclusion and Outlook

The results of molecular dynamics simulations performed using DRIAD to model ion and dust motion and dust grain charging have been presented. The characteristics of ion wakes forming in the presence of highly charged micrometer sized dust grains have been examined with simulations of dust grains positioned at various fixed interparticle separations and orientations relative to the ion flow direction. The stability of dust chains formed under various conditions within fast-moving ionization waves in the PK-4 experiment has been characterized and compared with results if plasma parameters are considered to be a simple time-average of fundamental quantities (such as ion and electron temperature, ion and electron density, and axial electric field strength). A summary of these results are presented below.

6.1 Dust Chain Stability in the Presence of Ionization Waves

6.1.1 Results

Fast-moving ionization waves present in a PIC-MCC simulation of conditions within the PK-4 showed variations in electron and ion temperatures, plasma density, and axial electric field strength which were shown to deviate by as much as ten times from the time-averaged value. The ion flow speed, which is driven by the axial electric field, is a critical factor in the formation of ion wakes and thus the degree of stability in the tens of particles long dust chains which have been experimentally observed in the PK-4. Dust

chains which formed under conditions simulating the peak electric field and ion flow speed were found to exhibit the most order, and developed ion wakes which spanned almost the full interparticle separation distance. Dust grains exposed to conditions with the weakest electric field and lowest ion flow speed had the smallest equilibrium interparticle separation in the resulting dust chain, irregular positioning of dust grains perpendicular to the ion flow direction, and formed nearly spherical, separated ion wakes. The dust chain that formed in plasma with the lowest plasma density and median electric field strength was highly ordered, but the ion wakes were more diffuse and had smaller maxima than was seen in the case with the highest electric field strength.

The time-averaged plasma conditions were unable to reproduce the experimental dust chain characteristics, and formed a disordered chain with isolated spherical ion wakes. It is therefore concluded that the variations present in the different phases of the ionization waves have a significant impact on the formation of stable dust chains, and the time-averaged values are inadequate to capture these effects. Further, it is noted that the formation of ion wakes that are elongated along the ion flow direction are correlated with higher order in the dust chains.

6.1.2 Future Work for Dust Chain Formation in Ionization Waves

Although the conditions at three distinct points within ionization waves were simulated as separate cases in this work, the ionization waves in the PK-4 experiment are moving rapidly with respect to the relatively stationary dust grains. As a result, the dust grains will be exposed to varying plasma conditions that may affect the equilibrium charge, interparticle separation, and structural order.

A simple capacitor model for dust grain charging in varying plasma conditions was presented in Section 4.4.2, where it was shown that the dust grain charges and discharges following the temporal variation of ionization wave conditions. A logical next step to fully characterize the impact of ionization waves on the stability of dust chains would therefore be to model the dust chain formation in the presence of varying plasma conditions. This is being addressed by incorporating a subroutine within DRIAD which recalculates the plasma quantities outlined in Section 3.3 based on variations to the axial electric field, electron and ion temperatures, and plasma density.

6.2 Dependence of Ion Wake Characteristics on Dust Grain Orientation

6.2.1 Results

The deflection of ions near highly charged dust grains leads to the accumulation of excess ion density in a region downstream from the dust grain. The location of the ion wake, and the amount of charge contained in the ion wake will determine the nature of non-reciprocal interactions between dust grains in a flowing plasma that lead to self-organization of dust into dust chains, zigzags, helices, and other interesting configurations. The interparticle separation distance at which the ion wakes of two dust grains begin to overlap is strongly dependent on the angle of orientation relative to the ion flow direction. For dust grains oriented parallel to the ion flow, the ion wakes begin to overlap at distances less than $12 \lambda_{Di}$, while dust grains positioned more than $8 \lambda_{Di}$ apart may form separate ion wakes if the angle of orientation is greater than 70° (close to perpendicular to the ion flow direction). The amount of charge in the wake is largest for dust grains oriented at 45° to the ion flow direction when the two wakes overlap, but

separate wakes result in the largest wake charge when they are oriented parallel to the ion flow direction. In the cases where a third dust grain was placed below two perpendicularly oriented dust grains, the largest wake charge was found when all three wakes have merged and all dust grains are positioned nearly perpendicular to the ion flow direction. For all interparticle separations with three dust grains, the largest peak ion density values were seen when the upper two dust grains were positioned closely together, regardless of the parallel separation to the third dust grain.

Analysis of the minimum energy of two and three dust grain configurations showed that positioning the third dust grain centered between the upper two dust grains resulted in a lower energy configuration than if the third dust grain was positioned at the expected minimum energy position determined from two dust grain simulations. Experiments with dust in zigzag or helical configurations corroborate this finding, with many of the structures having a centered dust grain at the top or bottom of the configuration.

6.2.1 Future Work

The present study of ion wake formation was performed with stationary dust grains, and fixed plasma conditions. To expand this work, the ion wake characteristics in the presence of multiple moving dust grains is being explored. The changing plasma parameters which are being used to investigate the time-varying conditions in ionization waves can be used to allow dust to form first in one stable configuration, after which point a transition to another stable configuration may be triggered. It is unclear at the present time whether the ion wake characteristics would depend only on the position and relative orientation of dust grains as they move from one configuration to another, or

whether there is a ‘memory’ aspect to the ion wake that is dependent upon the initial configuration of the dust structure.

BIBLIOGRAPHY

- Allen, J. E., Boyd, R. L., Reynolds, P., 1956. The collection of positive ions by a probe immersed in a plasma. *Proceedings of the Physical Society - Section B* 70, 297-304.
- Allen, J. E., 1992. Probe theory – the orbital motion approach. *Physica Scripta* 45, 497-503.
- Allen, J. E., de Angelis, U., 2000. *Journal of Plasma Physics* 63(4), 299-309.
- Antonova, T., Khrapak, S. A., Pustyl'nik, M. Y., Rubin-Zuzic, M., Thomas, H. M., Lipaev, A. M., Usachev, A. D., Molotkov, V. I., Thoma, M. H., 2019. Particle charge in PK-4 DC discharge from ground-based and microgravity experiments. *Physics of Plasmas* 26, 113703.
- Arp, O., Block, D., Klindworth, M., Piel, A., 2005. Confinement of Coulomb balls. *Physics of Plasmas* 12(12), 122102.
- Arp, O., Goree, J., Piel, A., 2012. Particle chains in a dilute dusty plasma with subsonic ion flow. *Physical Review E* 85, 046409.
- Banka, R., Vermillion, K., Matthews, L., Hyde, T., Couedel, L., 2022. Evolution of Ion Wake Characteristics with Experimental Conditions. (under review for publication in *Plasma Physics and Controlled Fusion*)
- Bellan, P. M., 2008. *Fundamentals of Plasma Physics*. Cambridge University Press.
- Block, D., Miloch, W. J., 2015. Charging of multiple grains in subsonic and supersonic plasma flows. *Plasma Physics and Controlled Fusion* 57(1), 014019.
- Bohm, D., Burhop, E. H. S., Massey, H. S. W., 1949. *The characteristics of electrical discharges in magnetic fields*. McGraw-Hill.
- Carbone, E., Graef, W., Hagelaar, G., Boer, D., Hopkins, M. M., Stephens, J. C., Yee, B. T., Pancheshnyi, S., van Dijk, J., Pitchford, L., 2021. Data needs for modeling low-temperature non-equilibrium plasmas: The LXCat project, history, perspectives, and a tutorial. *Atoms* 9(1), 16.
- Castrejon, A., Lyra, W., Richert, A. J., Kuchner, M., 2019. Disentangling planets from photoelectric instability in gas-rich optically thin dusty disks. *The Astrophysical Journal* 887, 16.

- Chaudhuri, M., Ivlev, A. V., Khrapak, S. A., Thomas, H. M., Morfill, G. E., 2010. Complex plasma – the plasma state of soft matter. *Soft Matter* 7(4), 1287-1298.
- Chen, F. F., 2018. *Introduction to Plasma Physics and Controlled Fusion*. Springer.
- Chu, J. H., Lin, I., 1994. Direct observation of Coulomb crystals and liquids in strongly coupled rf dusty plasmas. *Physical Review Letters* 72(25), 4009-4012.
- Couëdel, L., Zhdanov, S. K., Ivlev, A. V., Nosenko, V., Thomas, H. M., Morfill, G. E., 2011. Wave mode coupling due to plasma wakes in two-dimensional plasma crystals: In-depth view. *Physics of Plasmas* 18(8), 083707.
- Cui, C., Goree, J., 1994. Fluctuations of the Charge on a Dust Grain in a Plasma. *IEEE Transactions on Plasma Science* 22(2), 151-158.
- Dietz, C., Kretschmer, M., Steinmuller, B., Thoma, M. H., 2017. Recent microgravity experiments with complex direct current plasmas. *Contributions to Plasma Physics* 58, 21-29.
- Dietz, C., Budak, J., Kamprich, T., Kretschmer, M., Thoma, M. H., 2021. Phase transition in electrorheological plasmas. *Contributions to Plasma Physics*, e202100079.
- Donko, Z., 2011. Particle simulation methods. *Plasma Sources Science and Technology* 20, 024001.
- Donko, Z., Derzsi, A., Vass, M., Horvath, B., Wiczek, S., Hartmann, B., Hartmann, P., 2021. eduPIC: an introductory particle based code for radio-frequency plasma simulation. *Plasma Sources Science and Technology* 30, 095017.
- Dubinskii, A. Yu., Reznichenko, Yu. S., Popel, S. I., 2019. Formation and Evolution of Dusty Plasma Structures in the Ionospheres of the Earth and Mars. *Plasma Physics Reports* 45(10), 928-935.
- Dukes, C. A., Baragiola, R. A., 2013. Secondary electron emission from lunar soil: yields, energy distributions, and charging effects. *Planetary and Space Science* 89, 36-41.
- Farouki, R. T., Hamaguchi, S., 1992. Phase transitions of dense systems of charged “dust” grains in plasmas. *Applied Physics Letters* 61, 2973.
- Fortov, V. E., Nefedov, A. P., Torchinsky, V. M., Molotkov, V. I., Petrov, O. F., Samarian, A. A., Lipaev, A. M., Khrapak, A. G., 1997. Crystalline structures of strongly coupled dusty plasmas in dc glow discharge strata. *Physics Letters A* 229, 317-322.

- Fortov, V., Morfill, G., Petrov, O., Thoma, M., Usachev, A., Hoefner, H., Zobnin, A., Kretschmer, M., Ratynskaia, S., Fink, M., Tarantik, K., Gerasimov, Y., Esenkov, V., 2005a. The project 'Plasmakristall-4' (PK-4) – a new stage in investigations of dusty plasmas under microgravity conditions: first results and future plans. *Plasma Physics and Controlled Fusion* 47, B537-B549.
- Fortov, V., Ivlev, A., Khrapak, S., Khrapak, A., Morfill, G., 2005b. Complex (dusty) plasmas: Current status, open issues, perspectives. *Physics Reports* 421, 1-103.
- Goree, J., 1994. Charging of particles in a plasma. *Plasma Sources Science and Technology* 3, 400-406.
- Gurnett, D. A., Bhattacharjee, A., 2005. *Introduction to Plasma Physics with Space and Laboratory Applications*. Cambridge University Press.
- Hartmann, P., Douglass, A., Reyes, J. C., Matthews, L. S., Hyde, T. W., 2010. Crystallization dynamics of a single layer complex plasma. *Physical Review Letters* 105, 115004.
- Hartmann, P., Rosenberg, M., Juhasz, Z., Matthews, L. S., Sanford, D. L., Vermillion, K., Carmona-Reyes, J., Hyde, T. W., 2020. Ionization waves in the PK-4 direct current neon discharge. *Plasma Sources Science and Technology* 29, 115014.
- Hollenstein, C., Dorier, J. L., Dutta, J., Sansonnens, L., Howling, A. A., 1994. Diagnostics of particle genesis and growth in rf silane plasmas by ion mass spectrometry and light scattering. *Plasma Sources Science and Technology* 3, 278-285.
- Hutchinson, I. H., 2012. Intergrain forces in low-Mach-number plasma wakes. *Physical Review E* 85, 066409.
- Hyde, T. W., Kong, J., Matthews, L. S., 2013. Helical structures in vertically aligned dust particle chains in a complex plasma. *Physical Review E* 87(5), 053106.
- Ikezi, H., Coulomb solid of small particles in plasmas. *Physics of Fluids* 29(6), 1764.
- Ikkurthi, V. R., Matyash, K., Melzer, A., Schneider, R., 2008. Computation of dust charge and potential on a static spherical dust grain immersed in rf discharges. *Physics of Plasmas* 15(12), 123704.
- Ikkurthi, V. R., Matyash, K., Melzer, A., Schneider, R., 2010. Computation of charge and ion drag force on multiple static spherical dust grains immersed in rf discharges. *Physics of Plasmas* 17(10), 103712.

- Ishihara, O., Vladimirov, S. V., 1996. Wake potential of a dust grain in a plasma with ion flow. *Physics of Plasmas* 4(1), 69-74.
- Ivlev, A. V., Morfill, G. E., 2000. Anisotropic dust lattice modes. *Physical Review E* 63(1), 016409.
- Ivlev, A. V., Morfill, G. E., Thomas, H. M., Rath, C., Joyce, G., Huber, P., Kompaneets, R., Fortov, V. E., Lipaev, A. M., Molotkov, V. I., Reiter, T., Turin, M., Vinogradov, P., 2008. First observation of electrorheological plasmas. *Physical Review Letters* 100, 095003.
- Ivlev, A. V., Brandt, P. C., Morfill, G. E., Rath, C., Thomas, H. M., Joyce, G., Fortov, V. E., Lipaev, A. M., Molotkov, V. I., Petrov, O. F., 2010. Electrorheological Complex Plasmas. *IEEE Transactions on Plasma Science* 38(4), 733-740.
- Ivlev, A. V., Thoma, M. H., Rath, C., Joyce, G., Morfill, G. E., 2011. Complex plasmas in external fields: The role of non-Hamiltonian interactions. *Physical Review Letters* 106, 155001.
- Ivlev, A. V., Bartnick, J., Heinen, M., Du, C. -R., Nosenko, V., Lowen, H., 2015. Statistical mechanics where Newton's Third Law is broken. *Physical Review X* 5(1), 011035.
- Kamimura, T., Ishihara, O., 2012. Coulomb double helical structure. *Physical Review E* 85(1), 016406.
- Kersten, H., Deutsch, H., Stoffels, E., Stoffels, W. W., Kroesen, G. M. W., 2003. Plasma-powder interaction: trends in applications and diagnostics. *International Journal of Mass Spectrometry* 223, 313-325.
- Khrapak, A. G., Molotkov, V. I., Lipaev, A. M., Zhukhovitskii, D. I., Naumkin, V. N., Fortov, V. E., Petrov, O. F., Thomas, H. M., Khrapak, S. A., Huber, P., Ivlev, A., Morfill, G., 2016. Complex plasma research under microgravity conditions: PK-3 Plus laboratory on the International Space Station. *Contributions to Plasma Physics* 56(3), 253-262.
- Klahr, H., Brandner, W., Jakosky, B., 2006. Planet formation: Theory, observation, and experiments. Cambridge University Press.
- Kliushnychenko, O. V., Lukyanets, S. P., 2017. Effects of gas interparticle interaction on dissipative wake-mediated forces. *Physical Review E* 95, 012150.
- Klumov, B. A., Popel, S. I., Bingham, R., 2000. Dust particle charging and formation of dust structures in the upper atmosphere. *Journal of Experimental and Theoretical Physics Letters* 72(7) 364-368.

- Kompaneets, R., Konpka, U., Ivlev, A. V., Tsyтович, V., Morfill, G., 2007a. Potential around a charged dust particle in a collisional sheath. *Physics of Plasmas* 14, 052108.
- Kompaneets, R. 2007b. PhD Thesis, Complex plasmas: Interaction potentials and non-Hamiltonian dynamics.
- Kong, J., Hyde, T. W., Matthews, L., Qiao, K., Zhang, Z., Douglass, A., 2011. One-dimensional vertical dust strings in a glass box. *Physical Review E* 84, 016411.
- Kong, J., Qiao, K., Matthews, L. S., Hyde, T. W., 2014. Interaction force in a vertical dust chain inside a glass box. *Physical Review E* 90(1), 013107.
- Kureshi, R., Tripathi, K. R., Mishra, S. K., 2020. Electrostatic charging of the sunlit hemisphere of the Moon under different plasma conditions. *Astrophysics and Space Science* 365(2), 23.
- Laframboise, J. G., 1966. Theory of spherical and cylindrical Langmuir probes in a collisionless, Maxwellian plasma at rest. UTIAS Report No. 100.
- Lampe, M., Joyce, G., Ganguli, G., 2000. Interactions between dust grains in a dusty plasma. *Physics of Plasmas* 7(10), 3851-3861.
- Lampe, M., Gavrishchaka, V., Ganguli, G., Joyce, G., 2001. Effect of trapped ions on shielding of a charged spherical object in a plasma. *Physical Review Letters* 86(23), 5278-5281.
- Lipaev, A. M., Molotkov, V. I., Nefedov, A. P., Petrov, O. F., Torchinskii, V. M., Fortov, V. E., Khrapak, A. G., Khrapak, S. A., 1997. Ordered structures in a nonideal dusty glow-discharge plasma. *Journal of Experimental and Theoretical Physics* 85 (6), 1110-1118.
- Lisin, E. A., Petrov, O. F., Sametov, E. A., Vaulina, O. S., Statsenko, K. B., Vasiliev, M. M., Carmona-Reyes, J., Hyde, T. W., 2020. Experimental study of the nonreciprocal effective interactions between microparticles in an anisotropic plasma. *Scientific Reports* 10(1), 13653.
- Ludwig, P., Miloch, W. J., Kahlert, H., Bonitz, M., 2012. On the wake structure in streaming complex plasmas. *New Journal of Physics* 14, 053016.
- Matthews, L. S., Land, V., Hyde, T. W., 2012. Charging and coagulation of dust in protoplanetary plasma environments. *The Astrophysical Journal* 744, 8.
- Matthews, L. S., Shotorband, B., Hyde, T. W., 2013. Cosmic dust aggregation with stochastic charging. *The Astrophysical Journal* 776, 103.

- Matthews, L. S., Shotorban, B., Hyde, T. W., 2018. Discrete stochastic charging of aggregate grains. *Physical Review E* 97, 053207.
- Matthews, L. S., Sanford, D. L., Kostadinova, E. G., Ashrafi, K. S., Guay, E., Hyde, T. W., 2020. Dust charging in dynamic ion wakes. *Physics of Plasmas* 27, 023703.
- Matthews, L. S., Vermillion, K., Hartmann, P., Rosenberg, M., Rostami, S., Kostadinova, E. G., Hyde, T. W., Pustynnik, M. Y., Lipaev, A. M., Usachev, A. D., Zobnin, A. V., Thoma, M. H., Petrov, O. F., Thomas, H. M., Novitskiy, O. V., 2021. Effect of ionization waves on dust chain formation on DC discharge. *Journal of Plasma Physics* 87, 905870618.
- Melandsø, F., Goree, J., 1996. Particle simulation of two dimensional dust crystal formation in a mesothermal plasma flow. *Journal of Vacuum Science and Technology A* 14(2), 511-518.
- Melzer, A., Schweigert, V. A., Schweigert, I. V., Peters, S., Piel, A., 1996. Structure and stability of the plasma crystal. *Physical Review E* 54(1), 846-849.
- Melzer, A., Schweigert, V. A., Piel, A., 1999. Transition from attractive to repulsive forces between dust molecules in a plasma sheath. *Physical Review Letters* 83(16), 3194-3197.
- Melzer, A., 2006. Zigzag transition of the finite dust clusters. *Physical Review E* 73(5), 056404.
- Melzer, A., Schella, A., Mulsow, M., 2014. Nonequilibrium finite dust clusters: Connecting normal modes and wakefields. *Physical Review E* 89(1), 013109.
- Miloch, W. J., Kroll, M., Block, D., 2010. Charging and dynamics of a dust grain in the wake of another grain in flowing plasmas. *Physics of Plasmas* 17(10), 103703.
- Miloch, W. J., Block, D., 2012. Dust grain charging in a wake of other grains. *Physics of Plasmas* 19(12), 12703.
- Morfill, G. E., Ivlev, A. V., Thomas, H. M., 2012. Complex (dusty) plasmas – kinetic studies of strong coupling phenomena. *Physics of Plasmas* 19(5), 055402.
- Mott-Smith, H. M., Langmuir, I., 1926. The theory of collectors in gaseous discharges. *Physical Review* 28, 727-763.
- Piel, A., 2017. Molecular dynamics simulation of ion flows around microparticles. *Physics of Plasmas* 24, 033712.
- Pustynnik, M. Y., Fink, M. A., Nosenko, V., Antonova, T., Hagl, T., Thomas, H. M., Zobnin, A. V., Lipaev, A. M., Usachev, A. D., Molotkov, V. I., Petrov, O. F.,

- Fortov, V. E., Rau, C., Deysenroth, C., Albrecht, S., Kretchmer, M., Thoma, M. H., Morfill, G. E., Seurig, R., Stettner, A., Alyamovskaya, V. A., Orr, A., Kufner, E., Lavrenko, E. G., Padalka, G. I., Serova, E. O., Samokutyayev, A. M., Christoforetti, S., 2016. Plasmakristall-4: New complex (dusty) plasma laboratory on board the International Space Station. *Review of Scientific Instruments* 87, 093505.
- Pustyl'nik, M. Y., Klumov, B., Rubin-Zuzic, M., Lipaev, A. M., Nosenko, V., Erdle, D., Usachev, A. D., Zobnin, A. V., Molotkov, V. I., Joyce, G., Thomas, H. M., Thoma, M. H., Petrov, O. F., Fortov, V. E., Kononenko, O., 2020. Three-dimensional structure of a string-fluid complex plasma. *Physical Review Research* 2(3), 033314.
- Qiao, K., Kong, J., Van Oeveren, E., Matthews, L. S., Hyde, T. W., 2013. Mode couplings and resonance instabilities in dust clusters. *Physical Review E* 88(4), 043103.
- Raizer, Y. P., 1997. *Gas Discharge Physics*. Springer.
- Rohlena, K., Ruzicka, T., Pekarek, L., 1972. A theory of the low current ionization waves (striations) in inert gases. *Czechoslovak Journal of Physics B* 22, 920-937.
- Schmidt, J., Hyde, T. W., 2020. Discharge parameters of Plasmakristall-4BU: A modifiable dusty plasma experiment. *Review of Scientific Instruments* 91, 083506.
- Schroeder, D. V., 2000. *Thermal Physics*. Addison Wesley Longman.
- Schweigert, V. A., Schweigert, I. V., Melzer, A., Homann, A., Piel, A., 1996. Alignment and instability of dust crystals in plasmas. *Physical Review E* 54(4), 4155-4166.
- Selwyn, G. S., Singh, J., Bennett, R. S., 1989. In situ laser diagnostic studies of plasma-generated particulate contamination. *Journal of Vacuum Science & Technology A: Vacuum, Surfaces, and Films* 7(4), 2758-2765.
- Sheridan, T. E., 2012. Discontinuous structure transition in a Debye cluster. *Physics of Plasmas* 19(5), 057302.
- Shukla, P. K., 2000. A survey of dusty plasma physics. *Physics of Plasmas* 8(5), 1791-1803.
- Skullerud, H. R., 1968. The stochastic computer simulation of ion motion in a gas subjected to a constant electric field. *Journal of Physics D: Applied Physics* 1(11), 1567-1568.

- Sukhinin, G. I., Fedoseev, A. V., Antipov, S. N., Petrov, O. F., Fortov, V. E., 2013. Dust particle radial confinement in a dc glow discharge. *Physical Review E* 87, 013101.
- Takahashi, K., Oishi, T., Shimomai, K., Hayashi, Y., Nishino, S., 1998. Analyses of attractive forces between particles in Coulomb crystal of dusty plasma by optical manipulations. *Physical Review E* 58(6), 7805-7811.
- Takahashi, K., Totsuji, H., 2019. Structure of Coulomb crystals in cylindrical discharge plasmas under gravity and microgravity. *IEEE Transactions on Plasma Science* 47(8), 4213-4218.
- Thoma, M. H., Hofner, H., Kretschmer, M., Ratynskaia, S., Morfill, G. E., Usachev, A., Zobnin, A., Petrov, O., Fortov, V., 2006. Parabolic Flight Experiments with PK-4. *Microgravity Science and Technology* 18, 47-50.
- Thoma, M. H., Mitic, S., Uschev, A., Annartone, B. M., Fink, M. A., Fortov, V. E., Hofner, H., Ivlev, A. V., Klumov, B. A., Konopka, U., Kretschmer, M., Morfill, G. E., Petrov, O. F., Sutterlin, R., Zhdanov, S., Zobnin, A. V., 2010. Recent complex plasma experiments in a DC discharge. *IEEE Transactions on Plasma Science* 38(4), 857-860.
- Thomas, H., Morfill, G. E., Demmel, V., 1994. Plasma crystal: Coulomb crystallization in a dusty plasma. *Physical Review Letters* 73(5), 652-655.
- Thomas, H. M., Schwabe, M., Pustyl'nik, M. Y., Knappek, C. A., Molotkov, V. I., Lipaev, A. M., Petrov, O. F., Fortov, V. E., Khrapak, S. A., 2019. Complex Plasma Research on the International Space Station. *Plasma Physics and Controlled Fusion* 61, 014004.
- Trottenberg, T., Melzer, A., Piel, A., 1995. Measurement of the electric charge on particulates forming Coulomb crystals in the sheath of a radiofrequency plasma. *Plasma Sources Science and Technology* 4, 450-458.
- Usachev, A., Zobnin, A., Petrov, O., Fortov, V., 2004. The project "Plasmakristall-4 (PK-4) – A dusty plasma experiment in a combined DC/rf discharge plasma under microgravity conditions. *Czechoslovak Journal of Physics* 54, C639-C647.
- Vermillion, K., Sanford, D., Matthews, L., Hartmann, P., Rosenberg, M., Kostadinova, E., Carmona-Reyes, J., Hyde, T., Lipaev, A. M., Usachev, A. D., Zobnin, A. V., Petrov, O. F., Thoma, M. H., Pustyl'nik, M. Y., Thomas, H. M., Ovchinin, A., 2022. Influence of temporal variations in plasma conditions on the electric potential near self-organized dust chains. *Physics of Plasmas* 29, 023701.

- Vermillion, K., Banka, R., Mendoza, A., Wyatt, B., Matthews, L., Hyde, T., 2022. "Interacting dust grains in complex plasmas: ion wake formation and electric potential." arXiv.
- Vladimirov, S. V., Nambu, M., 1995. Attraction of charged particulates in plasmas with finite flows. *Physical Review E* 52(3), R2172-R2174.
- Vladimirov, S. V., Maiorov, S. A., Ishihara, O., 2003. Molecular dynamics simulation of plasma flow around two stationary dust grains. *Physics of Plasmas* 10(10), 3867-3873.
- Wang, Z., Tian, D. Ma, Z. Zhao, C., Liu, Y., Liu, Y., 2020. An electrostatic lofting model based on adhesion separation characteristics for lunar dust. *Planetary and Space Science* 184, 104883.
- Weidenschilling, S. J., 2000. Formation of planetesimals and accretion of the terrestrial planets. *Space Science Reviews* 92(1), 295-310.
- Whipple, E. C., 1981. Potentials of surfaces in space. *Reports on Progress in Physics* 44(11), 1197-1250.
- Xiang, C., Carballido, A., Matthews, L. S., Hyde, T. W., 2021. The initial structure of chondrule rims II: Charged grains. *Icarus* 354, 114053.
- Yaroshenko, V., Pustyl'nik, M., 2021. Possible mechanisms of string formation in complex plasmas at elevated pressures. *Molecules* 26, 308.
- Yukawa, H., 1934. On the Interaction of Elementary Particles I. *Proceedings of the Physico-Mathematical Society of Japan* 17, 48-57.
- Zhdanov, S. K., Ivlev, A. V., Morfill, G. E., 2009. Mode-coupling instability of two-dimensional plasma crystals. *Physics of Plasmas* 16(8), 083706.
- Zobnin, A. V., Usachev, A. D., Petrov, O. F., Fortov, V. E., 2008. Ion current on a small spherical attractive probe in a weakly ionized plasma with ion-neutral collisions (kinetic approach). *Physics of Plasmas* 15(4), 043705.
- Zobnin, A. V., Usachev, A. D., Petrov, O. F., Fortov, V. E., Thoma, M. H., Fink, M. A., 2018. Two-dimensional positive column structure with dust cloud: Experiment and nonlocal kinetic simulation. *Physics of Plasmas* 25, 033702.